Universidad
Carlos III de Madrid
www.uc3m.es

Bachelor Thesis

Tissue-on-a-Chip Design for Skin Modeling

Author

Carlos Matellán Martín

Directors

José Luis Jorcano Noval & Miguel Holgado Bolaños

October 2015

Abstract

Overcoming the challenges that the pharmaceutical industry currently faces requires the development of more sophisticated models of the human body. Tissue- and organ-on-a-chip technologies have arisen as a new enabling platform for organ modeling and drug screening based on bioinspired microfluidic systems. These devices have the potential to replicate the complex tissue architectures and organ-level interactions that dominate the systemic response to a drug.

The present work describes the design, modeling, fabrication and testing of a skin-biomimetic microfluidic device that can recapitulate skin physiology and architecture. The skin-on-a-chip developed herein is capable of accommodating a bioengineered skin equivalent continuously perfused through a microvascular channel, thus providing a solid proof of concept of the feasibility of a skin-modeling device for drug screening.

Acknowledgments

I would like to acknowledge my director, José Luis Jorcano, and the biomedical engineering department for their assistance. Special thanks to Diego Velasco for his support with microfluidics, Javier Rodriguez for his insightful comments and encouragement, and Nieves Cubo and Leticia Valencia for their help in the laboratory. I would also like to thank the technical staff of the department, especially Angelica Corral for her patience.

I would like to express my appreciation for my co-director, Miguel Holgado, and for the Optics, Photonics and Biophotonics group at the Center for Biomedical Technology. I am particularly grateful for the assistance given by Francisco Javier Sanza, who taught me everything I know about the art of microfabrication.

I would like to show my gratitude to Miguel Angel Martínez and Mariola Pantoja from the material science and engineering department for their guidance in some aspects of this project and for granting me access to their laboratories.

Finally, I wish to thank my friends and family for their patience, support and understanding. Special thanks to my mother for her unconditional love; to Denise Bosman, for believing I was capable even when I didn't; to Jose Manuel Rey, Elena Galbally and Daniel Martínez, for their friendship through the years; and to everyone that has helped me review the document.

"We are a way for the cosmos to know itself"
-Carl Sagan-

Table of Contents

List of Figures

List of Tables

1 Introduction

Efficient drug development requires new bioinspired models that can replicate the response of human organs or tissues to a drug. During the past 60 years, advancements in various scientific fields such as molecular pathology, combinatorial chemistry, omic technologies and bioinformatics have improved the capacity to identify new drug targets and to develop chemical libraries of candidate drug compounds. Other enabling technologies like High-throughput screening (HTS) allow rapid testing of these libraries against target proteins to identify those candidates with potential therapeutic effect. And yet, the number of new drugs approved per billion dollar spent in their development continues to decrease every year.

The decline in R&D productivity has been a cause of concern for the pharmaceutical industry since the 1950s. The new technologies that emerged during the past decades have caused a major improvement in the early stages of drug development, increasing the volume of compounds to be tested. However, the corresponding improvement in the R&D outcome that was expected as a result has not been observed yet. Despite having a hundred times more potential compounds and more efficient screening and testing tools, the number of new drugs approved is at its bottom while pharmaceutical companies continue increasing their investment in R&D without any tangible result.

Conventional drug screening systems include cell cultures and animal models. The former study the response of human cells to certain drugs, but they cannot replicate the systemic response because they are limited to a single cell type; while the latter offer a systemic response, but the results are often not comparable to those in humans. As a result, most unsuccessful drugs fail during clinical trials because current models fail to predict the systemic response of the human body to a drug.

Tissue-on-a-chip or organ-on-a-chip technologies consist in microfluidic cell culture systems designed to replicate the complex tissue and organ architecture and physiology as well as tissue- and organ-level interactions with the aim of simulating the dynamic and heterogeneous microenvironment of the human body. Although these technologies are still in their infancy, the use of microfluidics and microfabrication

techniques allows for a precise control of cell patterning, tissue-tissue interfaces and physicochemical gradients under physiological fluid flow conditions.

However, the real potential of tissue-on-a-chip technologies lies in the possibility of connecting multiple devices, each of them representing a different organ, to create human-on-a-chip or body-on-a-chip systems. These systems would be able to recapitulate the systemic response while maintaining the precision, control and automation of microfluidic devices. Whether fully integrated on a single chip or modular systems, human-on-a-chip technologies promise to offer revolutionary models of human biology with lower expenses and high control and automation capabilities.

The present work deals with the design, development, modeling, fabrication and testing of a tissue-on-a-chip device to model the skin. The design of this Skin-on-a-chip (SoaC) is inspired by some basic aspects of the architecture and physiology of the skin to accommodate a continuously perfused, mechanically stimulated organotypic skin culture.

2 Background, motivation and goals

Why do we need new model?

The low efficiency of drug development and discovery methods is one of the largest challenges that pharmaceutical industry currently faces. Developing a drug is both an expensive and time consuming process with a probability of success (POS) as low as 10.4% from phase I [1]. The estimated average cost for the development of a new molecular entity (NME) was in the order of US$ 802 million in the early 2000s [2] with estimates ranging from $500 million to over $2,000 millions [3]. These costs have shown an increasing trend in the last decade, with more recent estimates of $1,778 million (capitalized cost) in 2010 [4]. The estimated average time to develop a drug from its discovery to marketing approval spans from 12 to 15 years [5] [6], of which an average of 1.2 years correspond to the FDA review and approval phase [7] (data from 1992 to 2002); although this time has decreased for compounds with priority therapeutic significance since the passage of the PDUFA[1] [8].

Arguably, one of the main problems of the pharmaceutical industry is the decline in R&D productivity in the last 60 years (Fig. 2.1). Since 1950, the number of NME approved per billion dollars spent in development has halved every 9-10 years, a tendency that has been termed *Eroom's Law*[2] by some authors [9]. The plummeting of the productivity in the pharmaceutical industry is accompanied by a substantial increase in the attrition rates – the percentage of projects entering a given clinical phase that fail to complete it – as well an increase in development times and R&D expenditures [10]. Every year, pharmaceutical companies are spending more capital in developing drugs that fail at the late stages of the process, specially during Phase II and Phase III –the most expensive phases of the clinical trials [1].

[1] The prescription Drug User Fee Act to collect fees from companies that produce certain human drug and biological products. http://www.fda.gov/ForIndustry/UserFees/PrescriptionDrugUserFee/

[2] Eroom's law refers to Moore's law spelled backwards. Moore's Law states that the number of transistors in an integrated circuit roughly doubles every two years and R&D productivity in the pharma industry seems to follow the opposite tendency.

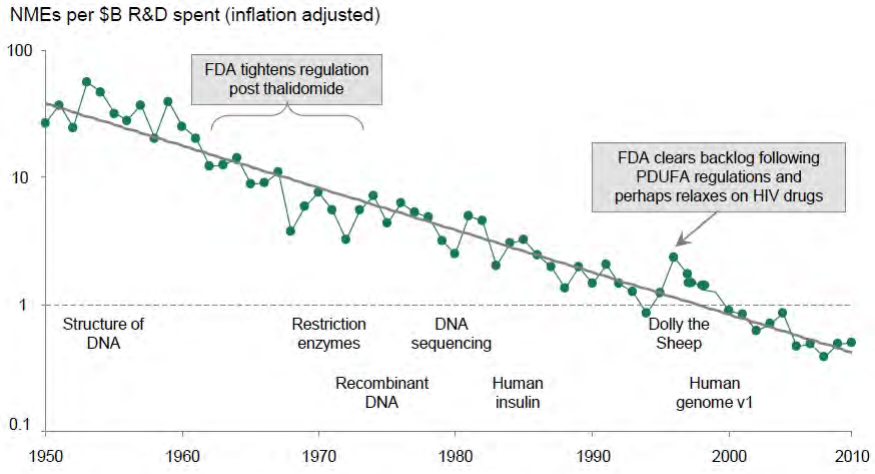

Figure 2.1: R&D productivity in the last 60 years. Notwithstanding a few exceptions, the graph shows a clear decline in productivity over the years. *Source: Bernstein Research, The Long View: Pharma R&D productivity – When the cures fail it makes sense to check the diagnosis, September 30, 2010*

In parallel with this decline, the development of new technologies has fueled the early stages of drug discovery, even allowing scientist to design drugs for specific targets on demand. Combinatorial chemistry allows to synthesize thousands of structurally related compounds, we know more than ever about molecular mechanisms of diseases and we can use bioinformatic tools to predict the behavior of these compounds *in silico* before they are even synthesized.

All these technologies have a profound impact at the beginning of the drug development value chain –the set of successive activities that the pharmaceutical industry performs to bring a newly discovered drug candidate to marketing approval– but this initially large volume of potential drugs is bottlenecked along the different stages of the development pipeline (Fig. 2.2). It has been estimated that for every 5,000-10,000 compounds that enter the pipeline, only 1 is approved for clinical use.

This lack of correlation between the input and the output of the pharmaceutical industry reveals a flaw in the testing methods, particularly those used in the middle stages of drug development. The main obstruction seems to take place between preclinical development and the beginning of clinical trials; in fact, only 11% of the drugs that showed promising results in animals are successful in clinical trials [11].

Even though there has been many efforts to improve the methods to predict the potential of a drug in its early stages of development, these data indicate that conventional models still fail to identify the appropriate candidates.

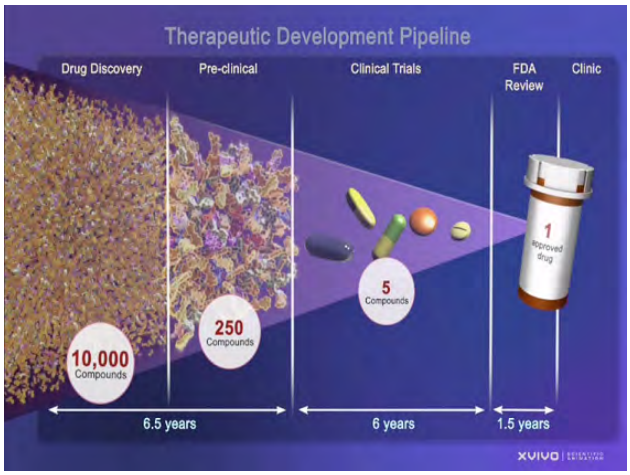

Figure 2.2: The drug discovery and development pipeline. *Source: http://www.ncats.nih.gov/research/reengineering/process.html*

From an ethical perspective, the replacement of animals models satisfies a growing societal concern regarding animal experimentation. In 2009, the European Commission approved a regulation on cosmetics which established a testing and marketing[3] ban: a prohibition to test finished cosmetic product or ingredients on animals and to commercialize any cosmetic product or ingredient that has been tested on animals within the EU [12]. At the same time, The European Centre for the Validation of Alternative Methods (ECVAM) was established in 2010 as a reference laboratory (EURL-ECVAM) for the research and validation of alternative methods to reduce, refine and replace animal testing [13].

Furthermore, the number of companies joining the Leaping Bunny Program, granted by the Cruelty Free International organization to firms that avoid animal testing, has increased over the years; and users are also demanding more cruelty-free cosmetics, household and beauty care products.

All these reasons reveal an impending need for alternative drug screening platforms that can replace

[3] The regulation from 2009 included some exceptions that were removed in the directive of 11 July 2013

conventional and inefficient animal models. By reducing the expenses and development times, pharmaceutical companies will be able to bring new drugs into the market at a lower cost and a faster pace, making them more widely available and for a larger number of diseases.

Why microfluidic Organs on Chips?

The pharmaceutical industry requires new screening systems which should be to able select, with high sensitivity and specificity, those compounds that present high efficacy and no toxicity in humans. Current platforms to test drug efficacy and toxicity consist of *in vitro* cell cultures and animal models. Recent advances in cell culture, such as 3D cultures and bioprinted tissues, offer better results than traditional 2D cultures, particularly for cancer and stem cell research [14, 15], but are still limited to a particular cell line, tissue or organ, and thus unable to reproduce the systemic response of the body. On the other hand, animals models can replicate organ-organ interactions and provide a systemic response that is essential to study the pharmcokinetics and phamacodynamics of the drug, but the results obtained in animals often cannot be extrapolated to humans. New models have to be capable of recapitulating human tissue and organ physiology and interactions to replicate the systemic response of the human body.

For many years, scientists have tried to replicate the complex *in vivo*-like conditions in cell cultures. Traditional 2D cell cultures consist of cells randomly seeded on a homogeneous culture plate and bathed by an homogeneous culture medium. Cells in 2D cultures interact with the solid substrate only on one of their sides and tend to acquire an abnormal morphology and polarization. Moreover, nutrients, oxygen and molecules added to the medium are readily available to all the cells. These conditions widely differ from the complex and dynamic environment of tissues and organs. 3D cultures based on hydrogel scaffolds, developed in the 1950s [16], can assemble into more complex structures to simulate more physiological-like conditions and cell-ECM interactions [17] (Fig. 2.3). However, these models still cannot reproduce the hierarchical organization of tissues and organs, the spatio-temporal microscale gradients and the physical stimulation –mechanical or electrical– that drives mechanotransduction [18].

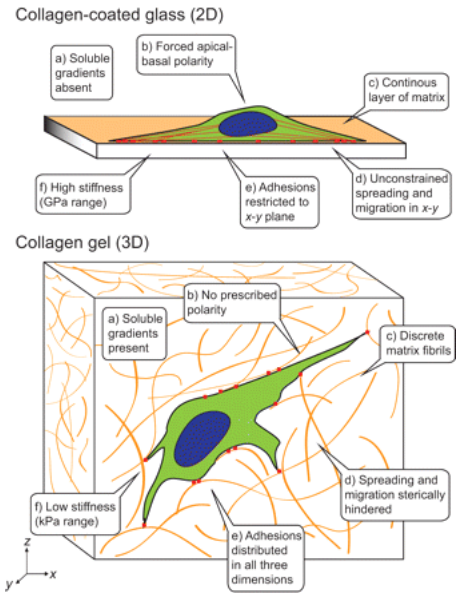

Figure 2.3: Main differences between 2D and 3D culture systems. *Source: Baker et al. Deconstructing the third dimension–how 3D culture microenvironments alter cellular cues. Journal of cell science, 2012.*

Bioengineered skin equivalents are well developed and widely used in clinical and preclinical applications [19]. These skin grafts can be used to generate skin-humanized mice models for drug discovery, disease modeling and basic skin research. A variety of humanized-mouse disease models have already been developed including genodermatoses, cancer prone diseases and wound healing abnormalities [20] as well skin inflammatory diseases [21]. Transgenic mice are also used as animal models [22]. These models, however, are complex and costly to establish, expensive to maintain and their utility is limited to skin modeling, since they cannot be extended to other tissues or connected to other organ models.

Microfluidic technologies offer many advantages over conventional cell culture platforms. Devices can be designed with biologically relevant dimensions to assay single cells or to reproduce realistic tissue size ratios. The small dimensions of the channels and the use of minute fluid volumes lead to a reduction in reagent consumption and waste production as well as reaction times due to higher effective concentrations [23]. Microfabrication techniques allow for the production of batches at a low cost that can be operated and visualized simultaneously [24]. The laminar flow within the microchannels allows to predict the performance of the device with mathematical models of fluid flow and transport

phenomena [25] and to generate specific and stable gradients of multiple molecules such as those that dominate cellular microenvironments [26–28]. Moreover, micropatterning techniques can be used to precisely determine cell location and density, allowing heterogeneous distribution of cells within the devices [29, 30]. The small size of the devices, their simplicity of operation and the small reagent use allow for low cost, high-throughput, portable systems [24].

Microfluidic devices have a wide range of applications within the biomedical field, such as research in stem cell biology [31, 32], oncology [33] and other cellular mechanisms including migration, cell-cell interactions and angiogenesis [34], as well as drug discovery [35, 36]. The possibilities for applications are endless, and limited only by the capacity to microfabricate the design into a real device.

Within this context, tissue-on-a-chip or organ-on-a-chip technologies arose as more sophisticated versions of microfluidic cell cultures. Several definitions of these technologies have been given, and it has become a hot topic in the last years [18, 37, 38]. Despite the differences, all authors coincide in the use of microfluidic and microfabrication technologies to develop complex models of tissue and organ physiology with *in vivo*-like conditions that simulate a minimal functional unit of those organs (Fig. 2.4). Some models have already been developed for a variety of organs such as liver [39–42], kidney [43], gastrointestinal (GI) tract [44–46], bone [47], blood vessels [48], lungs [49], muscle [50], heart [51] or bone marrow [52].

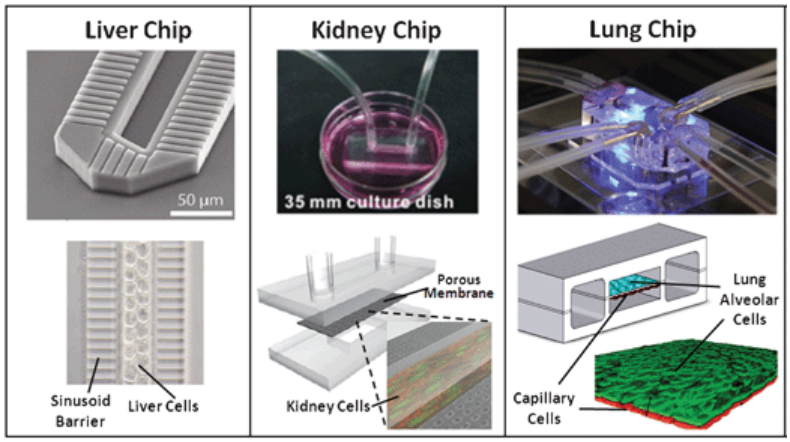

Figure 2.4: Examples of the design of Organ-on-a-chip devices for liver, kidney and lung. *Source: Huh, D et al. Microengineered physiological biomimicry: organs-on-chips. Lab on a chip. 2012*

The biomimetic approach

Early attempts to design organ-on-a-chip devices aimed at miniaturizing conventional cell culture techniques. Most of these devices were based on culture chambers supplied by microfludic channels where individual cell lines were seeded [53]. Later versions embedded cells in hydrogels to develop 3D cultures [54] or contained chambers to perfuse small tissue samples obtained from a biopsy [55, 56]. Some systems even incorporated several of these miniaturized cell cultures connected by microchannels, effectively creating the first body-on-a-chip models [57].

These systems exhibited several advantages over macro-scale cell cultures such as high multiplexing capacity, continuous media perfusion and connectivity. Some of them could even maintain temperature to sustain the culture outside of an incubator [58]. However, they presented the same limitations of conventional cultures: the response of a single cell line cannot replicate the complexity of an organ. *In vivo*, organs are not formed by single layers of one cell type completely submerged in a fluid and connected by channels; instead, they preset highly complex and hierarchical architectures that are critical to their functions and they are supplied by an intricate network of blood vessels.

In the last years, the field has experienced a paradigm shift towards bioinspired design. Modern organ-on-a-chip devices are more sophisticated systems with several cell types arranged to simulate tissue-tissue interfaces with biologically relevant dimensions and near-physiological conditions; some of which can even recapitulate pathological conditions [49, 59]. Recent designs incorporate actuators to subject the culture to physical forces [59–61] to recapitulate mechanotransduction mechanisms that have been shown to be key in the regulation of cell behavior [62, 63].

This biomimetic approach is essential towards the development of integrated body-on-a-chip systems. For instance, developing biomimetic models of the GI tract lining and capillary walls is fundamental to recapitulate the absorption and distribution of oral drugs [64, 65]. Likewise, a model of skin is required to study topical delivery and a model of blood-brain-barrier is basic to study drug delivery to the brain. Functional models of liver lobules and kidney nephrons are key to understand the metabolism, toxicity and elimination [66–68] of the drug from the system. All these complex processes – known as the

ADMET (absorption, distribution, metabolism, excretion and toxicity) – describe the phamacokinetics of the drug and thus the systemic response of the body.

Why Skin-on-a-chip?

Within the context of body-on-a-chip systems, the skin constitutes an essential organ for drug screening. Not only is the skin the largest organ of the human body and its primary barrier against pathogens, but also it is directly in contact with cosmetics, topically delivered drugs and other chemicals.

Percutaneous absorption is a key route of drug administration. The permeability of the epidermis to the drug and the diffusion through the dermis and the endothelium determine the concentration of the drug that reaches the bloodstream and therefore, the drug bioavailability. The skin-on-a-chip is key to study the ADMET of topical formulations and to understand new methods of delivery and new formulations such as nanoparticles [69].

The epidermis, especially the stratum corneum, constitutes a barrier that severely limits percutaneous absorption of drugs. As a result, the therapeutic success of topically delivered drugs is often determined by its capacity to penetrate the epidermis. For this reason, in order to develop a drug screening platform that reproduces percutaneous drug absorption, it is fundamental to model the skin in 3D with all its layers –including the stratum corneum. This problem is specific to the skin and makes it a particularly challenging organ to model.

Goals of the project

This work aims at developing a biomimetic skin-on-a-chip device for drug screening. The first objective is to design a bioinspired microfluidic system based on skin biology. The main aspects of this design include a culture chamber to host a 3D skin culture, a porous membrane that serves as interface with a microvascular channel and two lateral pneumatic channels to subject the culture to cycles of strain that simulate the tension on the skin in order to examine the effect of mechanotransduction on the response to drugs. The concepts of skin physiology and architecture relevant to its design are described in Section 3.

Secondly, a mathematical model ought to be developed to provide a foundation for the quantitative analysis of the operation of the device and the absorption of tested drugs. The mathematical model presented 5 combines principles of transport phenomena and physiology.

Once this groundwork is developed, the next objective is to fabricate the device in accordance with the design using common microfabrication techniques or developing new methods when required. The complete fabrication protocol is established in Section 6. Finally, the device will be tested to ensure that it is capable of hosting and perfusing a bioengineered skin equivalent. This proof of concept of the device is presented in Section 7. The scope of this project, therefore, includes the design, model, fabrication and testing a skin-on-a-chip device.

The long term end goal is to develop a cost effective skin biomimetic microdevice that can be established as drug testing platform. This system must be compliant with the existing regulation for alternative methods to animal testing established by the EURL-ECVAM. Moreover, the device should be easy to integrate into multi-organ systems to constitute body-on-a-chip networks for systemic studies of pharmacokinetics and pharmacodynamics.

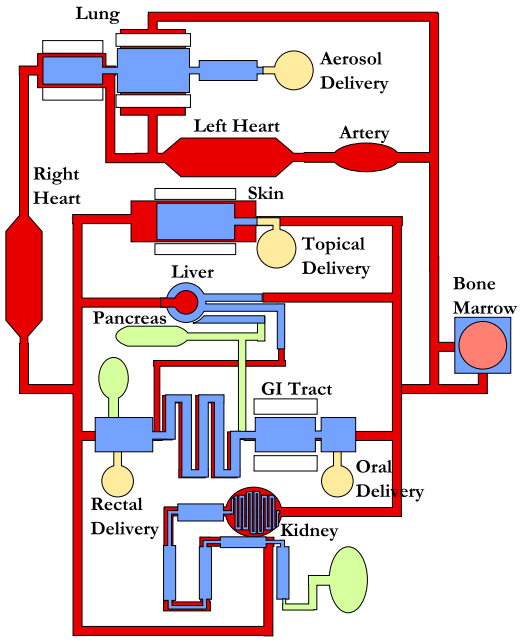

Figure 2.5: Design of a body-on-a-chip network

3 Skin bioinspiration

This chapter explores the architecture, functions and physiology of the skin. Special attention is payed to the vascularization of the skin as an essential concept to model dermal absorption as well as to the responses of the skin to physical forces via mechanotrasduction as a key element to direct cell behavior. These elements are the basis of the design presented in Section 4

3.1 Histology and physiology of the skin

The skin is the largest organ of the body, covering an area of up to $2m^2$ in an average adult. It carries out a number of functions that are essential to maintain homeostasis: it participates in thermoregulation by adjusting blood flow to the surface and by liberating sweat, it excretes various substances in sweat and absorbs lipid soluble substances like vitamins A, D, E and K, it synthesizes vitamin D thanks to its exposure to UV light, it provides thermal, tactile and pain sensations and behaves as a primary barrier for protection against pathogens, abrasion, dehydration and sunlight. [70]

From the point of view of the architecture, the skin is a relatively simple organ composed mainly by two layers: the dermis and the epidermis.

The dermis is a layer of connective tissue of variable thickness (up to 4 mm depending on the region of the body) rich in collagen and elastic fibers embedded in a ground substance composed of glycosaminoglycans and proteoglycans and rich in dermatan sulfate [71]. The dermis, in turn, is divided in two layers: the inner reticular layer and the outer papillary layer. The reticular layer is formed by irregular dense connective tissue composed of densely packed fibers, particularly bundles of collagen type I, and few cells. The papillary layer is composed of loose connective tissue and contains a higher density of cells (Fig. 3.1). The surface of the papillary dermis presents dermal papillae that project into the dermis, interlocking with epidermal ridges (Rete Ridges).

Fibroblasts constitute the main cell type that resides in the dermis. They are in charge of producing, secreting and remodeling the extracellular matrix (ECM) that forms most of this connective tissue.

Thus, fibroblasts have a role in tissue homeostasis and wound healing that makes them an essential element of the dermis.

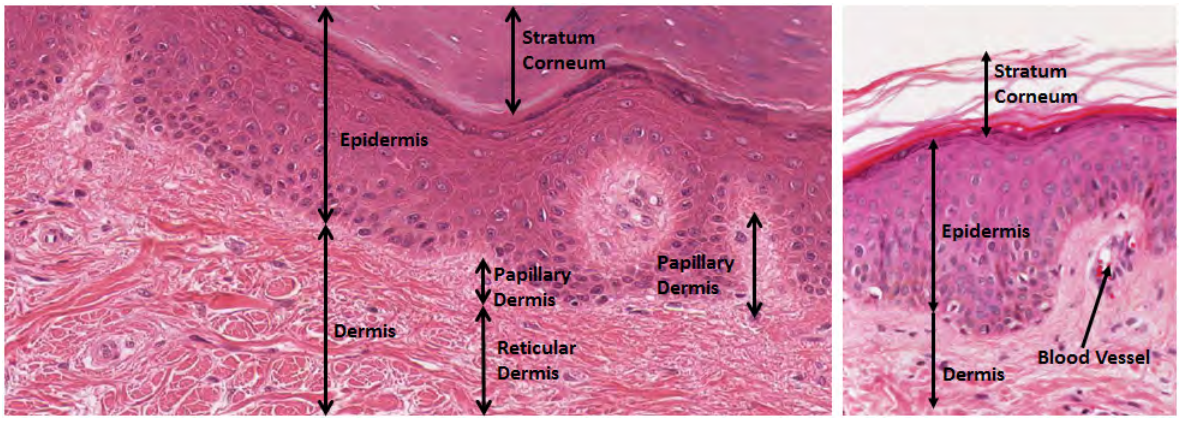

Figure 3.1: Histological slide of the skin depicting the layers that constitute its architecture. *Source: Images modified from histological slides. Michigan's collection of virtual microscope slides & slides for Junqueira's basic histology. Indiana University*

The function of the dermis is to support the epidermis i.e. it constitutes the stroma of the skin. It provides mechanical and structural support to the epidermis, anchoring it to the subcutaneous tissues; and supplies nutrition, oxygenation and innervation from its capillaries, lymphatic vessels and nerve endings. It also contains several types of sensory receptors, including mechanoreceptors for crude and discriminative touch, thermoreceptors and nocioceptors; glands like sebaceous and sweat glands; and hair root plexuses.

The epidermis is a cornified stratified squamous epithelium that forms the parenchyma of the skin. The keratinocytes that form the epidermis are organized in multiple layers or strata: stratum basale, stratum spinosum, stratum granulosum[4] and stratum corneum (Fig. 3.2). The morphology of the cuboidal cells in the basal layer changes progressively towards squamous in suprabasal layers.

The basal layer[5] is the only proliferative layer of the skin; it contains interfollicular epidermal stem cells

[4] Thick skin, such as that on the palms and soles contains a fifth layer after the stratum granulosum known as stratum lucidum

[5] And sometimes the lower section of the spinous layer, collectively known as the stratum germinativum

and mitotically active transit-amplifying cells that are in charge of the tissue renewal. The progeny of these cells migrates to upper layers and undergoes a differentiation process. Cells in the stratum spinosum contain a high number of keratin filaments arranged in tonofibrils and connected to those of adjacent cells via desmosomes to generate a network of keratin fibers capable of withstanding high tension. The stratum granulosum contains cells that produce lamellar granules; secreting their lipid-rich content in the interstititum between cells to create an impermeable layer that serves as protection against water lost and foreign substances. Cells in this stratum degenerate and undergo apoptosis as they migrate to upper layers, finally forming the stratum corneum. The stratum corneum is the outer layer of the skin, formed by 10-30 layers of flattened non-nucleated cells devoid of organelles, filled with keratin and surrounded by lips; forming a thick, impermeable and strong barrier.

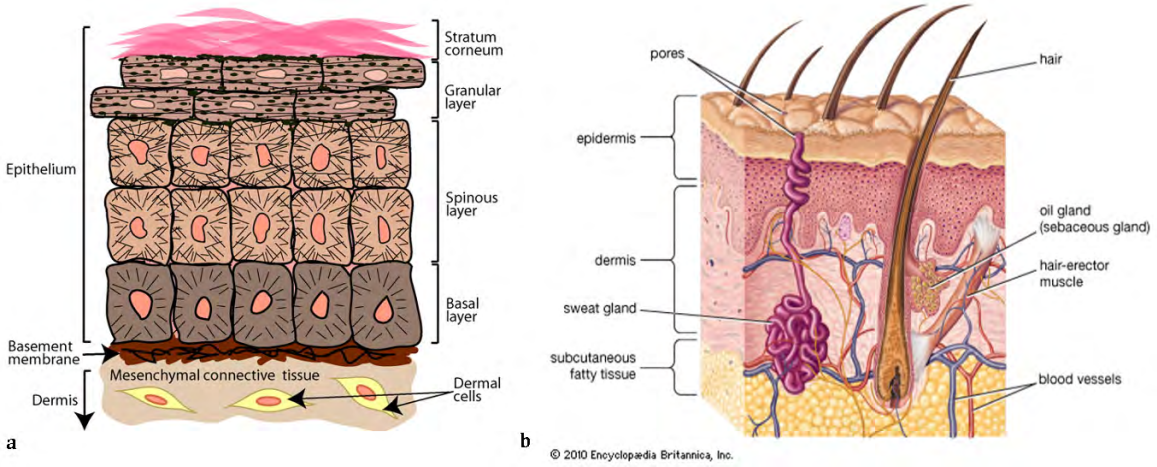

Figure 3.2: Structure of the skin. **(a)** Schematic representation of the epidermal strata **(b)** Depiction of the skin layers, blood supply and appendages. . *Sources: (a) Alonso, L et al. Stem cells of the skin epithelium. Proceedings of the National Academy of Sciences. 2003. (b) Encyclopedia Britannica.*

The dead non-nucleated cells that form the stratum corneum are continuously shed and replaced by cells that differentiate from lower strata. The epidermal stem cells in the stratum basale have self renewal capacities and they give rise to a progeny of cells[6] that undergoes suprabasal migration and

[6] Stem cells divide only rarely to produce transit-amplifying cells, which in turn divide quickly to produce a high number of keratinocytes

differentiation. In this process, cells in each strata are "pushed up" to upper layers as the lower strata are occupied by newly formed cells. Throughout the process, cells degenerate and increase their keratin content as they migrate to upper layers, losing their nuclei when they become part of the stratum corneum and are eventually shed. This mechanism allows the skin to continually renew itself thanks to the capacity of stem cells to divide at the same rate as the cornified layer is shed while remaining themselves undifferentiated. The time it takes for a cell to complete this process, from its division to shedding, is known as the epidermal turnover rate, and its spans 4-6 weeks.

The point of contact between the dermis and the epidermis is known as the dermoepidermal junction. The basal layer of the epidermis rests on an specialized ECM known as the basement membrane that provides attachment and filtering functions and affects polarization and differentiation. The basement membrane (basal lamina) is composed of a clear layer formed by laminin, known as the lamina lucida; and a an electron-dense layer formed by collagen type IV. Entacting and perlecan bind these two layers together, while anchoring fibrils of collagen type VII attach the basement membrane to the underlying dermis and hemidesmosomes formed by integrins attach the cytoskeleton of keratinocytes to the upper side of the basement membrane.

3.2 Vascularization of the skin

As an epithelial tissue, the epidermis of the skin lacks blood vessels, lymphatic vessels and nerves. Only the stroma of the skin (dermis) is vascularized, i.e. the blood vessels that supply the skin are found in the dermal layer (Fig. 3.2). Oxygen and nutrients diffuse out of these capillaries and are transported across the papillary dermis to nurture cells in the avascular epidermis (Fig. 3.3). This method of oxygen and nutrient delivery and waste product removal is common to other tissues such as cartilage (nurtured by the perichondrium) or the GI tract mucosas (nurtured by the submucosal layer), hence the importance of modeling and understanding the process.

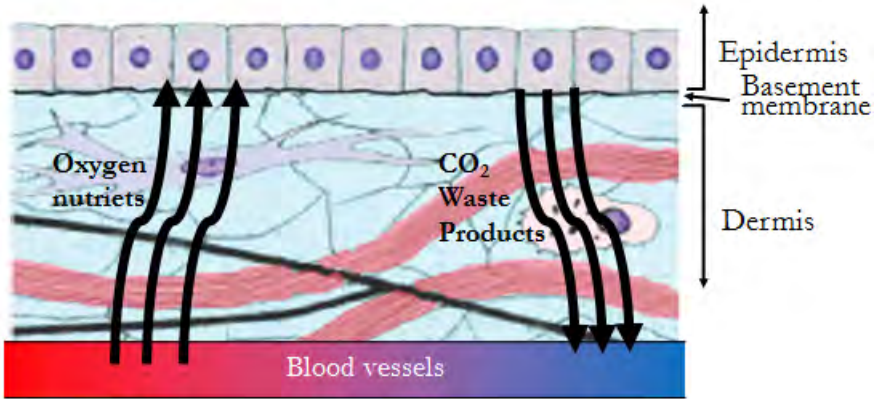

Figure 3.3: Vascularization of the skin. The Epidermis (avascular) is nurtured by the blood vessels in the dermis

The exchange of fluid and dissolved molecules between the capillaries and the surrounding interstitium is governed by a balance of forces known as the net filtration pressure (NFP). There are four main components that constitute the NFP: the hydrostatic pressure in the capillaries P_c and the interstitial fluidP_i; the oncotic or blood colloid osmotic pressure –the osmotic pressure developed by plasma proteins, specially the large ones like albumin, that cannot easily cross the capillary wall– BCOP or Π_c; and the osmotic pressure of the interstitial fluid Π_i. Hydrostatic pressure in the capillaries promote the leakage of plasma out of the capillaries while blood oncotic pressure tends to pull fluid into the capillaries (Fig. 3.4). On the other hand, the interstitial hydrostatic and osmotic pressures act in the reverse orientation and are small[7] compared to the other contributions, thus they can be neglected in approximations. Based on this balance of opposing forces, the NFP can be computed as:

$$NFP = (P_c - P_i) - (\Pi_c - \Pi_i) \tag{1}$$

Whereas the blood oncotic pressure remains nearly constant (∼26 mmHg) for the entire length of the capillaries due to the low permeability of the capillary wall to large proteins, the hydrostatic pressure decreases progressively away from the heart, dropping from 35 mmHg at the arterial end to 16 mmHg at

[7] The interstitial hydrostatic pressure is small due to the lymphatic drainage, while interstitial osmotic pressure is nearly zero due to the lack of proteins in the interstitial fluid

the venous end of the capillary. As a result, there is a shift in the sign of the NFP along the capillaries and the filtrate fluid is driven through the capillary walls in opposite orientations at either end. At the arterial end of the capillary, the hydrostatic pressure exceeds the oncotic pressure leading to a net filtration i.e. leakage of fluid out of the capillary. On the other hand, as the hydrostatic pressure drops, it is overcome by the pull from the oncotic pressure, leading net reabsorption (negative NFP) at the venous end of the capillary (Fig. 3.4).

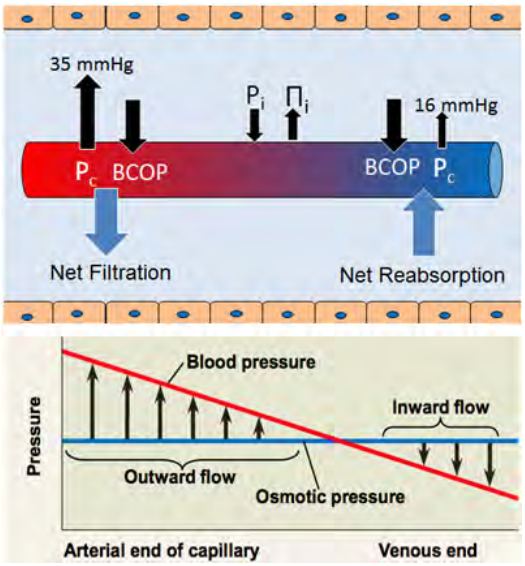

Figure 3.4: Dynamics of capillary fluid exchange with the interstitial fluid.
Source: Image modified from StudyBlue. Biological Sciences Bsc, 2011

While this mechanism allows most of the leaked fluid to be reabsorbed back into the blood stream, it is not perfectly balance and the volume of filtration is 15-20% higher than the reabsorption volume. This excess of fluid is drained by the lymphatic system, used to sample body fluids for antigens by the lymph nodes and then returned to the circulation at the subclavian vein. The drainage by the lymphatic capillaries prevents accumulation of interstitial fluid, and imbalances in this system lead to peripheral edema.

The network of capillary loops that supply the epidermis branches off from the subpapillary plexus, located between the reticular and the papillary dermis. This vascular plexus is connected to a second one that is located between the dermis and the underlying subcutaneous tissue (reticular plexus).

The hypodermis or subcutaneous tissue is composed of highly vascularized adipose tissue that allows rapid uptake and distribution of drugs. For these reasons, understanding and simulating the transport through the skin into the hypodermis is key to model drug absorption.

3.3 Mechanotransduction and skin biology

Mechanotransduction can be defined as the process by which cells transform mechanical stimuli into biochemical activity. The role of physical forces on cell behavior has become a hot topic in the last decade, although they were known to have an effect certain organs, such as the organ of Corti in the ear and the skin, for a long time (for the skin since the discovery of Langer's lines in 1861 [72]).

Cells in many tissues, such as bones, muscles, skin, blood vessels or lungs, are constantly subjected to physical forces; and these forces have an effect on their physiology. The results of this mechanism are well documented in certain cases, such as the loss of bone mass and osteoporosis in astronauts subjected to weightless environments for extended periods of time [73], the adaptation of the skin to pregnancy and obesity or the effect of blood flow shear stress on endothelial cells

Most research nowadays focuses on understanding the signaling pathways that these forces elicit and how these pathways regulate gene expression and alter cell behavior [62, 63, 74]. Several models have been proposed to explain how physical forces may cause a change in biochemical activity [63, 75]. The tensegrity model, proposed by D. Ingber, postulates that the forces are transferred to the cytoskeleton and the karyoskelton to directly cause changes in gene expression [76].

It is clear that the skin is subjected to numerous forces such as tension when we grow or change weight; during wound healing; or abrasion in the palms and soles. Understanding how these forces affect the skin from the cellular scale to the tissue and organ levels is essential to both simulate the skin and bioengineer it. Current devices to study the effect of these forces are severely limited and bulky [77]. On the other hand, microfluidic devices offer the possibility of controlling the mechanical environment of cells, subjecting them to highly controlled stimuli [61]. The SoaC device developed in the present work incorporates two pneumatic channels that can be used to subject the organotypic culture to desired cycles of tension.

4 Design of the skin-on-a-chip device

The SoaC device was designed based on the concepts of skin biology described in Section 3 and taking the lung-on-a-chip [78] developed by D. Ingber et al. as a starting point. The basic architecture of the SoaC device consists of two central channels and two bilateral channels. The device is built in three layers: A lower layer containing the microvascular channel, an intermediate porous membrane and an upper layer containing the culture chamber and the lateral pneumatic channels.

The first aspect of skin biology that was considered in the design was its structure. As previously described, the skin is composed of a connective tissue layer rich in ECM and populated by fibroblasts –dermis– and a cornified stratified squamous epithelium –epidermis. A simple tissue monolayer is unable to recapitulate the complexity of this structure and therefore a more advanced tissue architecture is required.

An organotypic skin culture can be constructed with a hydrogel-based matrix with embedded fibroblasts simulating the dermis. Fibrin (fibrinogen) from human plasma can form a hydrogel upon reaction with thrombin –triggering the coagulation cascade– which fibroblasts can remodel, eventually replacing the fibrin with collagen. Moreover, keratinocytes and HaCaT cells seeded on these matrices have been shown to undergo suprabasal differentiation upon contact with an air [79], which allows for the spontaneous formation of the epidermis. A skin equivalent constructed with this methods is fully composed of human materials, allowing a closer recapitulation of human biochemistry.

A chamber that can accommodate a 3D skin culture is therefore an integral part of the design. The dimensions of the chamber (800 µm width and 500 µm height) were chosen to offer a relatively large –according to microfluidic standards– skin surface and taking into account the thickness limitations of microfabrication techniques. This chamber can host a dermis of $\sim 300\,\mu m$ thickness and a normal epidermis of $\sim 100\,\mu m$ [71] while allowing enough space for an air-liquid interface and epicutaneous drug administration.

Based on the skin vascularization principles (Section 3.2), a microvascular channel was incorporated in the design. This channel interfaces with the culture chamber through a porous membrane that

separates the upper and lower layers of the device. Moreover, the vascular side of the membrane serves as mechanical support for the formation of an endothelial monolayer. The endothelium –which forms the capillary walls *in vivo*– regulates the transport across the capillary walls and has a key role in hemostasis and inflammatory responses, thus being essential to recapitulate capillary exchange.

Finally, two pneumatic channels were designed on either side of the central culture chamber for mechanical stimulation. These channel are half the width of the chamber ($\sim 400\,\mu m$) and separated from it by a $50\,\mu m$ deformable wall. Pneumatic channels have been used since 2000 to create microvalves [80]. The pneumatic channels can be operated with a small, computer controlled vacuum pump, collapsing inwards and deforming the walls of the chamber outwards to stretch the tissue. Moreover, the position of the channels allows for maximum deformation at the midpoint of the chamber's height, corresponding approximately to the dermoepidermal junction. This mechanism can be used to study the tissue- and organ-level response of the skin to mechanical forces.

Figure 4.1 illustrates the design concept of the SoaC device, including the central chamber with the skin equivalent 3D culture, the bilateral pneumatic channels for physical stimulation, the porous membrane for interfacing, and the microvascular channel.

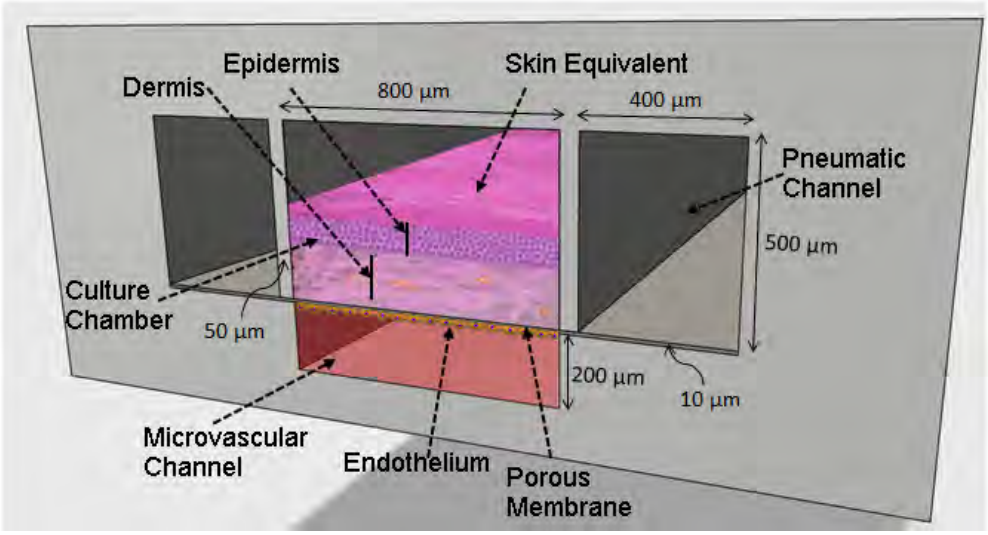

Figure 4.1: Cross-sectional view of the skin on a chip device depicting the culture chamber with a fully developed skin equivalent, the microvascular channel, the porous membrane and the pneumatic channels

Based on this concept, two microfluidic masters were designed for the upper and lower layers (Fig. 4.2). The thickness of the SU-8 master was 500 µm and 200 µm for the upper and lower layers, respectively. The position of the inlet and outlet of the microvascular channel was selected not to interfere with the rest of the device, and a double port system was designed for the central chamber whose purpose will be described in Section 7.3. An additional view of the cross-section of the device with the positions and dimensions of the ports is presented in Figure 4.3

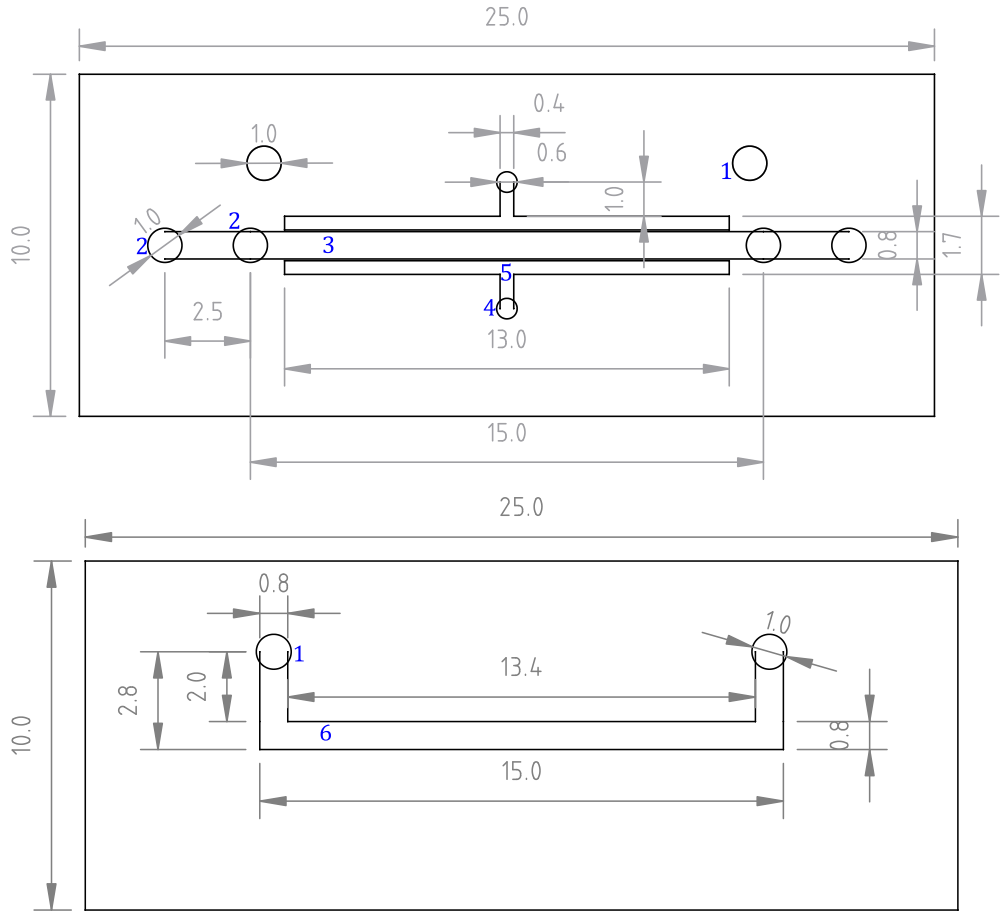

1. Access port for the microvascular channel
2. Double port system for the upper chamber
3. Cell culture microchamber
4. Access to the pneumatic channels
5. Lateral pneumatic channels
6. Microvascular channel

Figure 4.2: Design of the SU-8 master for the upper (above) and lower (below) microfluidic layers, with a thickness of 500 μm and 200 μm respectively. *Scale:* mm

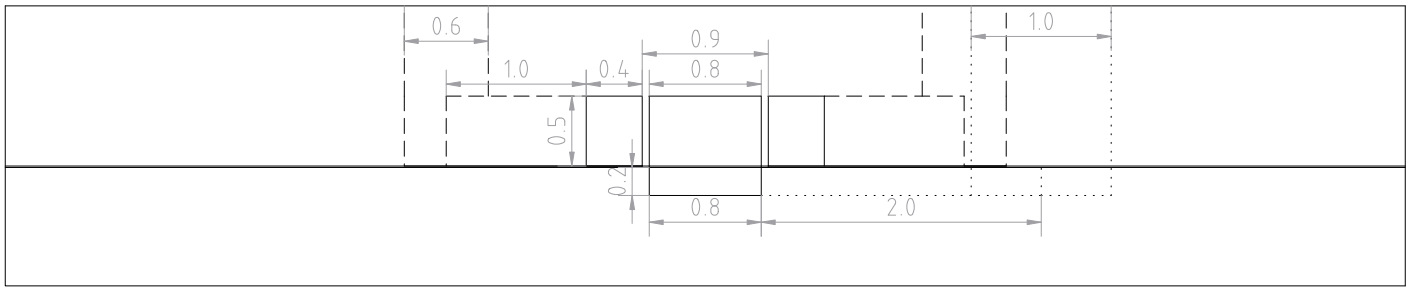

Figure 4.3: Design of the device cross-section. Dotted and dashed lines represent inlets and outlets for the microvascular and pneumatic channels respectively

A PDMS membrane with microfabricated pores was also designed as a possible candidate for the membrane that separates the upper and lower layers of the device (Fig. 4.4). This membrane contains a central porous region with an array of pores with a diameter of 10 µm and a spacing of 40 µm arranged in a square distribution.

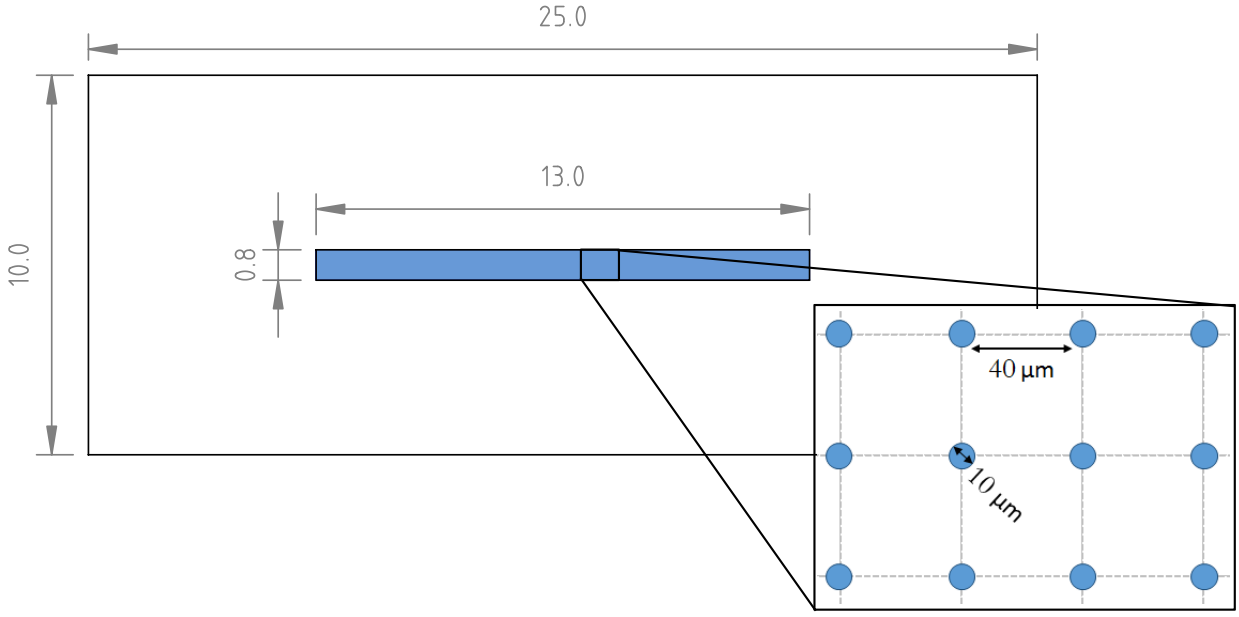

Figure 4.4: Design of the PDMS membrane with a porous region and detail of the pore size and distribution

A three-dimensional display of the device, including the three layers prior to chip assembly and the complete device, is presented in Figure 4.5. Additionally, several assembled devices can be bound to a glass slide for parallel operation (Fig. S1)

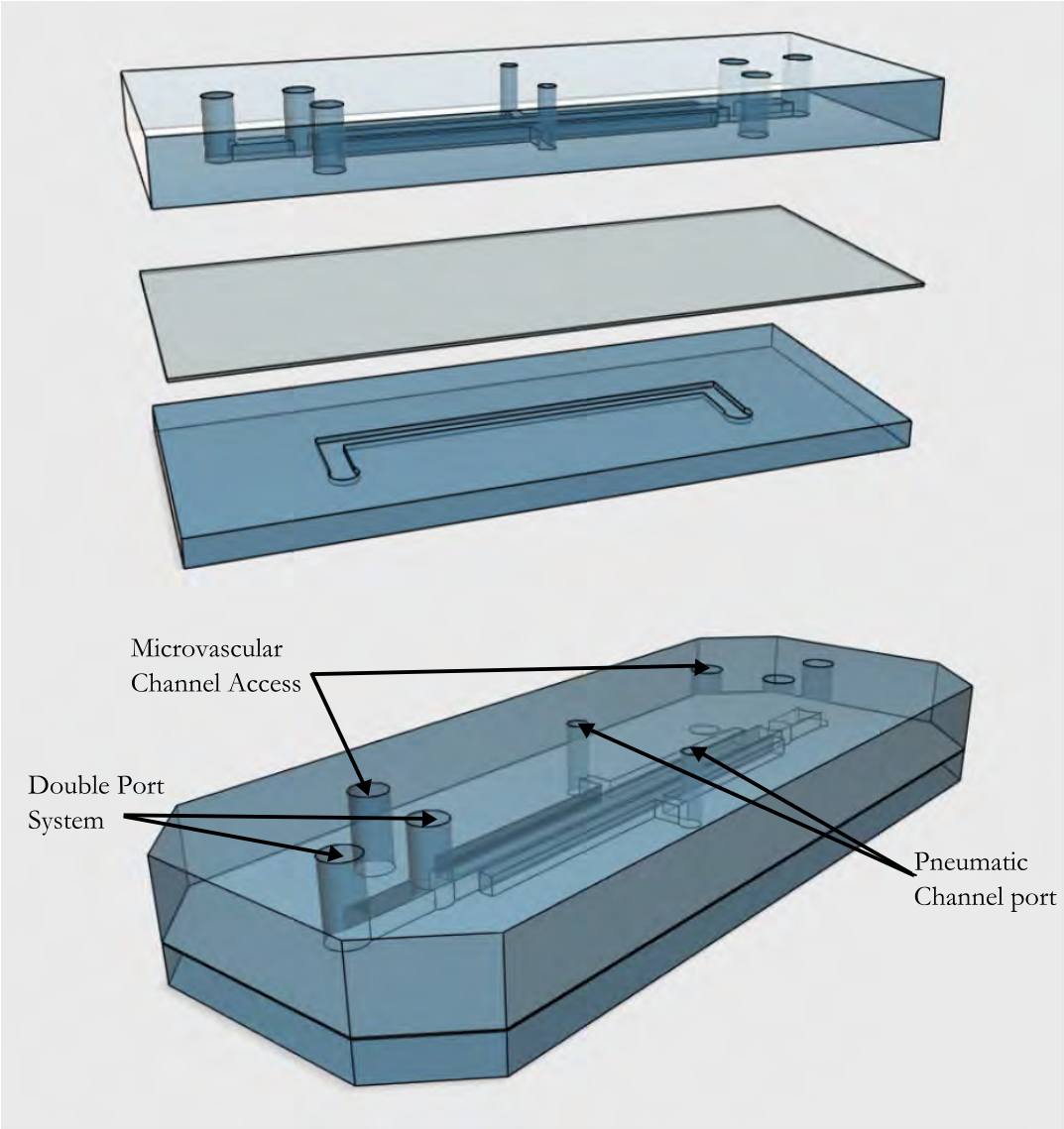

Figure 4.5: Three-dimensional view of the device. The three layers (top) are stacked to assemble the complete device (below)

5 Mathematical modeling

In this section, a mathematical model of the SoaC device is developed. First, the fluid flow through the microvascular channel and across the porous membrane is modeled by means of fluid dynamics. Then, the interstitial flow is studied for two different situations of suprabasal differentiation: early and late stages. Finally, a diffusion-convection-reaction conservation equation is derived to model the supply of O_2 and the transport of other molecules such as CO_2, lactate or drugs through the skin. While simplified, this model provides a basic understanding of the device performance.

The present work takes into consideration both physic's laws and principles of physiology to provide a more comprehensive model that can recapitulate various phenomena that are observed in the skin *in vivo,* such as the filtration-reabsorption transport through capillary walls, cutaneous oxygen uptake or the interstitial flow in the dermis. Detailed derivation of selected equations can be found in Annex II.

The primary goal of this model is to establish a groundwork for the future development of more accurate and elaborate ones. This contribution towards predicting the behavior of tissue-on-a-chip devices is fundamental to the design of body-on-a-chip systems that serve as quantitative models for drug discovery.

5.1 Blood flow model

The first step is to model the blood flow inside the microvascular channel based on fluid dynamics. Consider a channel of rectangular cross-section with height h, width w and length L (Fig. 5.1). An incompressible fluid of density ρ and viscosity μ flows along the channel, simulating the blood flow in the capillaries that supply the skin. Furthermore, the gauge pressures at the inlet and outlet of the channel are P_1 and P_2 respectively and the atmospheric pressure is P_o. Finally, the channel is bounded by a porous membrane with permeability δ.

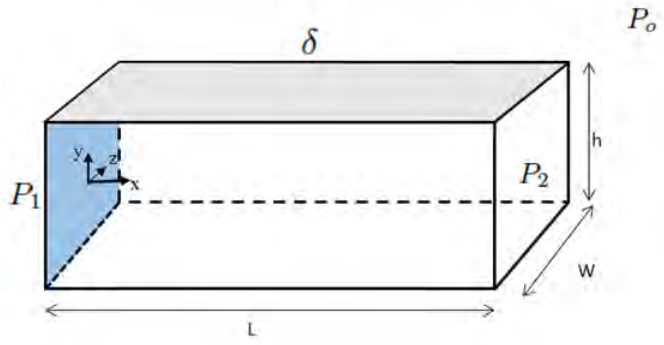

Figure 5.1: Geometry and Reference System of the microvascular channel

The permeability δ is the ratio between the filtration velocity across a membrane and the pressure difference that generates it $v = \delta \triangle P$, and thus has units of $\frac{\text{m/s}}{\text{Pa}}$. The permeability can be related to a *hydraulic conductivity* by using an analogy with electromagnetism. Consider coulomb's law for a uniform electric field: $\vec{j} = \sigma \triangle V/L$ where σ is the conductivity. The velocity, v, and the pressure difference, $\triangle P$, are analogous to the current density, $\vec{j}$, and the voltage drop, $\triangle V$ respectively. Therefore δ can be understood as a *hydraulic conductivity* –inverse to the tendency of the membrane to resist the flow– per unit thickness.

There are various parameters that affect the permeability such as mean pore size, pore distribution and density, nominal thickness of the membrane and pore constriction [81]. Additionally, if the porous membrane is lined with an endothelial monolayer, the permeability will be affected by the transport across this cellular layer.

The dynamics of viscous fluid motion can be described by the Navier-Stokes equations; a set of equations that apply the principles of mass conservation and Newton's second law derived continuum media. For

an incompressible, newtonian fluid[8], they can be reduced to:

$$\nabla \cdot \vec{v} = 0 \tag{2}$$

$$\rho \left(\frac{\partial \vec{v}}{\partial t} + \vec{v} \cdot \nabla \vec{v} \right) = -\nabla p + \mu \nabla^2 \vec{v} + \vec{f_m} \tag{3}$$

These equations can be simplified by performing dimensional analysis on equation (3). The Reynolds Number (Re) is a dimensionless number that measures –as a ratio– the relative magnitude of inertial and viscous forces:

$$\underbrace{\rho \left(\frac{\partial \vec{v}}{\partial t} + \vec{v} \cdot \nabla \vec{v} \right)}_{\sim \rho \frac{v^2}{D_H}} = -\nabla p + \underbrace{\mu \nabla^2 \vec{v}}_{\sim \mu \frac{v}{D_H^2}} + \vec{f_m} \tag{4}$$

$$Re = \frac{\text{Inertial Forces}}{\text{Viscous Forces}} = \frac{\rho v D_H}{\mu} \tag{5}$$

where D_H is the hydraulic diameter, defined as: $D_H = \frac{4A}{P}$. For this particular problem, the hydraulic diameter is computed as $D_H = \frac{2hw}{(h+w)}$; and the Reynolds Number can be calculated from equation (5) by considering $v = Q/hw$

$$Re = \frac{2\rho Q}{\mu(h+w)} \tag{6}$$

The Reynolds number can also be expressed in terms of the inlet and outlet pressures using a rough estimate of the flow rate $Q = \frac{P_1 - P_2}{L} \frac{h^2}{8\mu} \frac{2hw}{3} = \frac{(P_1 - P_2) h^3 w}{12 L \mu}$. Substituting in eq. (6) the result is:

$$Re = \frac{2\rho \left(P_1 - P_2\right) h^3 w}{12 L \mu^2 (h+w)} << 1 \tag{7}$$

Additional assumptions can be made to simplify the problem. First, the effect of gravity is negligible due to the small scale, and there are no other body forces exerted on the fluid, hence $\vec{f_m} = 0$. Second,

[8] Blood is a non-newtonian fluid with a complex rheology that depends on a variety of factors such as the hematocrit, the concentration of dissolved fibrinogen and several pathologies. More advanced constitutive models could be considered such as Bingham plastic or Casson fluid, but this would render the equation impossible to solve analytically. Moreover, most of the rheological complexity arises from the formed elements of blood, which are absent in this fluid. Hence the assumption of a newtonian behavior is justified.

there is no lateral velocity, i.e. $v_z = 0$. Moreover, considering the flow conditions presented in section (7.2), the flow develops under low Reynolds number regime (i.e. $Re << 1$), thus the inertial forces (left-hand side of the momentum equation) are negligible. With these assumptions, the Navier-Stokes equations for continuity and conservation of x-momentum are simplified to:

$$\frac{\partial v_x}{\partial x} + \frac{\partial v_y}{\partial y} = 0 \tag{8}$$

$$0 = -\frac{\partial P(x)}{\partial x} + \underbrace{\mu\left(\frac{\partial^2 v_x}{\partial z^2} + \frac{\partial^2 v_x}{\partial y^2}\right)}_{\sim\mu\frac{v_L}{D_H^2}} + \underbrace{\mu\frac{\partial^2 v_x}{\partial x^2}}_{\sim\mu\frac{v_L}{L^2}} \tag{9}$$

This kind of problem is often classified as a quasi-unidirectional flow. Consider now the fact that the length of the channel L is significantly larger than its hydraulic diameter $D_H = \frac{2hw}{(h+w)}$, that is $\frac{L}{D_H} >> 1$. A dimensional analysis of the viscous terms in eq. (9) provides an estimate of the relative order of magnitude of the transverse and longitudinal forces:

$$\frac{\mu\frac{\partial^2 v_x}{\partial x^2}}{\mu\left(\frac{\partial^2 v_x}{\partial z^2} + \frac{\partial^2 v_x}{\partial y^2}\right)} \sim \frac{\mu\frac{v_L}{L^2}}{\mu\frac{v_L}{D_H^2}} = \left(\frac{D_H}{L}\right)^2 << 1 \tag{10}$$

This means that the longitudinal component of eq. (9) is negligible with respect to the transverse components. From an intuitive standpoint, since the width and height of the channel are much smaller than its length, all magnitudes that depend on position (in this case, the velocity) change much faster in a cross-section than along the channel length. Hence, neglecting the longitudinal component of eq. (9), the momentum equation is reduced to:

$$0 = -\frac{\partial P(x)}{\partial x} + \mu\left(\frac{\partial^2 v_x}{\partial z^2} + \frac{\partial^2 v_x}{\partial y^2}\right) \tag{11}$$

At this point the problem can be solved as an unidirectional flow by decomposing the solution $\vec{v}(x, y)$ into two terms: one term depending only on y that corresponds to the solution for the unidirectional flow in a channel of infinite width, $V(y)$; and a second term that corresponds to the perturbation introduced by the finite width $\varphi(y, z)$ with $V(y) >> \varphi(y, z)$. Taking into account the non-slip and

symmetry boundary conditions presented below

$$\begin{aligned} v_x(y, z = \pm w/2) &= 0 \quad \frac{\partial v_x}{\partial y}(y = 0, z) = 0 \\ v_x(y = \pm h/2, z) &= 0 \quad \frac{\partial v_x}{\partial z}(y, z = 0) = 0 \end{aligned} \tag{12}$$

the previous eq. (11) can be split into an ODE and a PDE by neglecting the perturbation term $\varphi(y, z)$ in the ODE and applying the method of separation of variables to the PDE $\varphi(y, z) = X(x)Y(y)$

$$\begin{cases} 0 = Pl + \mu V_{yy} \\ 0 = \varphi_{yy} + \varphi_{zz} \end{cases} \tag{13}$$

with $Pl = -\frac{\partial P(x)}{\partial x}$, which can be solved analytically to yield the solution for a quasi-unidirectional flow in a channel of rectangular cross-section (Solution obtained from [82])

$$v_x(x, y, z) = \frac{Pl(x) \cdot h^2}{8\mu} \left[\left(1 - \frac{4y^2}{h^2}\right) - \sum_{n=0}^{\infty} \frac{32(-1)^n \cosh\left((2n+1)\frac{\pi z}{h}\right) \cos\left((2n+1)\frac{\pi y}{h}\right)}{(2n+1)^3 \pi^3 \cosh\left((2n+1)\frac{\pi w}{2h}\right)} \right] \tag{14}$$

Notice that, as expected from the previous decomposition, this parabolic velocity profile (Fig. 5.2) corresponds to the solution of a Poiseuille flow in a rectangular channel of infinite width plus a perturbation introduced by the finite width. The factor $\frac{Pl(x) \cdot h^2}{8\mu}$ has units of m/s and it is in fact related to the peak velocity[9]. This solution can be regarded as an instantaneous[10] or local parabolic profile with a maximum velocity that changes depending on the position along the channel (x)

[9] The actual peak velocity is: $v_{max} = \frac{Pl(x) \cdot h^2}{8\mu} \left(1 - \sum_{n=0}^{\infty} \frac{32(-1)^n}{(2n+1)^3 \pi^3 cosh\left((2n+1)\frac{\pi w}{2h}\right)}\right)$ since the perturbation term in nonzero in the center of the channel

[10] In this case instantaneous refers to an spatial coordinate, not to a time dependance

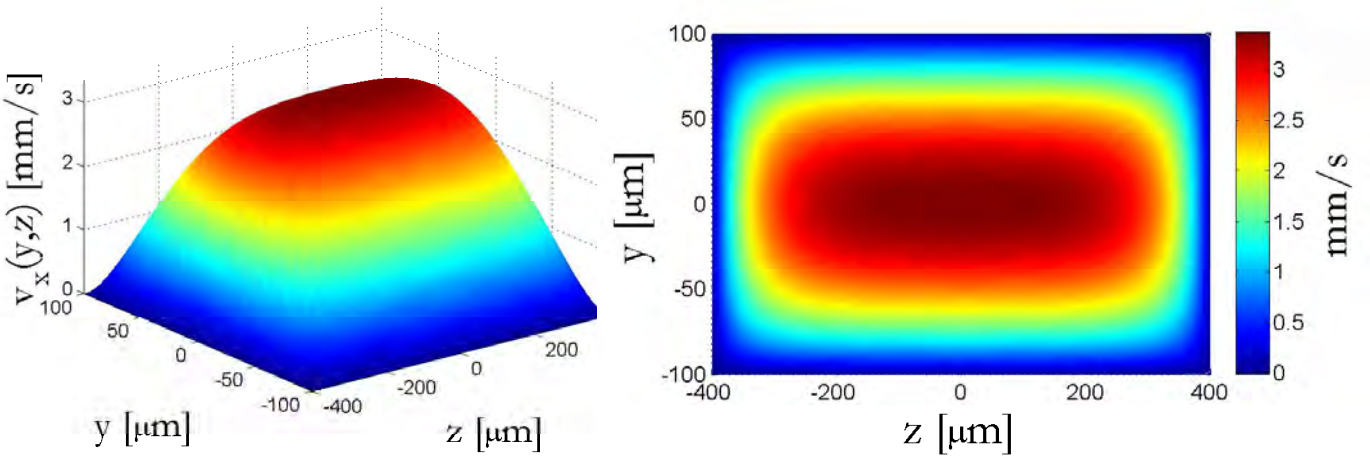

Figure 5.2: Velocity profile $v_x(y, z)$ in the microvascular channel computed for a position x close to the center of the channel (L/2). This profile can be understood as a local parabolic profile scaled by the instantaneous pressure gradient. Notice that the velocities are in the order of mm/s.

The filtration through the upper wall of the channel is precisely what determines the problem as quasi-unidirectional flow. Since there is fluid exchange with the upper dermal layer, there is a decrease in flow rate and a drop in the local pressure gradient, hence explaining the dependance on x of the velocity profile. To fully characterize the flow in the microvascular channel, the pressure field $P(x)$ has to be determined. Based on the aforementioned principle of filtration, we ought to consider the continuity equation and the definition of the flow rate through a plane that corresponds to a cross-section of the channel:

$$Q = \iint_{\Sigma} \vec{v}(x, y, z) \cdot \vec{n} d\sigma = \iint_{y,z} v_x(x, y, z) dz dy \tag{15}$$

Integrating eq. (8) with respect to x and z and applying Leibniz's integral rule

$$\frac{\partial}{\partial x} \int_{-\frac{w}{2}}^{\frac{w}{2}} \int_{-\frac{h}{2}}^{\frac{h}{2}} v_x dy dz + \int_{-\frac{w}{2}}^{\frac{w}{2}} \int_{-\frac{h}{2}}^{\frac{h}{2}} \frac{\partial v_y}{\partial y} dy dz = 0 \tag{16}$$

According to definition of flow rate –eq. (15) – and the relationship between derivatives and integrals,

the expression above can be reduced to:

$$\frac{\partial}{\partial x}Q(x) + \int_{-\frac{w}{2}}^{\frac{w}{2}} v_y(y = h/2)dz = 0 \tag{17}$$

since $v_y(-h/2) = 0$ because it corresponds to the velocity perpendicular to a non-porous wall. On the other hand $v_y(y = h/2)$ is the interfacial or filtration velocity across the porous membrane v_{int}

To understand the meaning of eq. (17), consider a control volume within the channel with a boundary Σ formed by two parallel cross-sections separated by a distance Δx and the four walls of the channel (Fig. 5.3). The integral form of the continuity equation for an incompressible fluid states $\int_\Sigma \vec{v} \cdot \vec{n} d\sigma = 0$ that is, the net sum of the flow rates coming into and out of the volume through the boundaries must be zero. In this problem, the velocity profile $v_x(y, z)$ and thus the flow rate, depend on the position x along the channel i.e. $Q = Q(x)$.

For this reason, the flow rate coming into the control volume through the first cross-sectional boundary is not the same as the flow rate going out through the second cross-section; and the difference between these two must be equal to the filtration flow rate through the upper porous wall: $Q(x + \Delta x) - Q(x) = Q_{filtration}$. When the separation between the two parallel cross-section becomes infinitesimally small ($\lim_{\Delta x \to 0}$) the previous expression turns into equation (17)

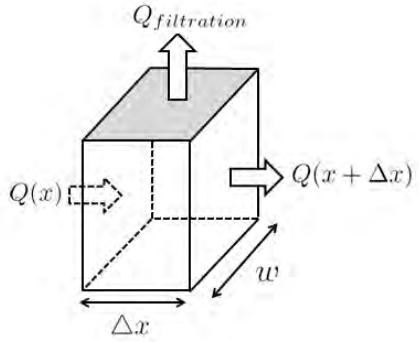

Figure 5.3: Continuity condition applied to a control volume bounded by two cross-sections

The principles of cardiovascular physiology presented in Section 3.2 can be summarized in a mathematical expression known as the Starling's Law

$$v_{int} = \delta \left(P(x) - P_i - \triangle \Pi \right) \tag{18}$$

where $P(x)$ is the local pressure in the channel side, P_i is the hydrostatic pressure of the interstitial fluid (the dermal layer) and$\triangle \Pi$ is the difference in oncotic pressure between the channel and the interstitial fluid. The permeability δ is the hydraulic conductivity per unit thickness of the membrane; and depends on the mean pore size, pore density and distribution, and other properties of the membrane such as hydrophilicity.

The flow rate can be obtained by integrating eq. (14)

$$Q(x) = \frac{Pl(x) \cdot h^2}{8\mu} \left[\frac{2}{3} hw - \sum_{n=0}^{\infty} \frac{128 \cdot \sinh\left((2n+1) \frac{\pi w}{2h} \right) \left(\frac{h}{(2n+1)\pi} \right)^2}{(2n+1)^3 \pi^3 \cosh\left((2n+1) \frac{\pi w}{2h} \right)} \right] \tag{19}$$

and to simplify the expression, we can define:

$$< A >= \left[\frac{2}{3} hw - \sum_{n=0}^{\infty} \frac{128 \cdot \sinh\left((2n+1) \frac{\pi w}{2h} \right) \left(\frac{h}{(2n+1)\pi} \right)^2}{(2n+1)^3 \pi^3 \cosh\left((2n+1) \frac{\pi w}{2h} \right)} \right] \tag{20}$$

hence, eq. (19) is reduced to:

$$Q(x) = -\frac{\partial P}{\partial x}(x) \cdot \frac{h^2}{8\mu} < A > \tag{21}$$

Using this new information in eq. (17) and taking into account that $v_y(y = h/2)$ does not depend on z so that $\int_{-\frac{w}{2}}^{\frac{w}{2}} v_y(y = h/2) dz = v_{int} \cdot w$

$$-\frac{\partial^2 P(x)}{\partial x^2} \cdot \frac{h^2}{8\mu} < A > + \delta \left(P(x) - P_i - \triangle \Pi \right) \cdot w = 0 \tag{22}$$

To make this equation more feasible of manipulations, let $k = \frac{\delta 8 \mu}{h^2 < A >} w$ and $\Pi = P_i + \triangle \Pi$. Therefore we arrive at a second order ordinary differential equation for the pressure $P(x)$

$$\frac{\partial^2 P(x)}{\partial x^2} - kP(x) = -k\Pi \tag{23}$$

which can be readily solved with P_1 and P_2 being the inlet and outlet pressures

$$\begin{aligned} P(x) &= C_1 \cdot e^{\sqrt{k}x} + C_2 \cdot e^{-\sqrt{k}x} + \Pi \\ C_1 &= \frac{(P_1 - \Pi)\, e^{-\sqrt{k}L} - (P_2 - \Pi)}{e^{-\sqrt{k}L} - e^{\sqrt{k}L}} \\ C_2 &= \frac{(P_2 - \Pi) - (P_1 - \Pi)\, e^{\sqrt{k}L}}{e^{-\sqrt{k}L} - e^{\sqrt{k}L}} \end{aligned} \tag{24}$$

Under physiological conditions, the interstitial pressure is significantly smaller than the hydrostatic pressure (from 1 to -1 mmHg versus 35-16 mmHg) and hence the term Pi in $\Pi = P_i + \triangle\Pi$ can be practically neglected. Moreover, the osmotic pressure of the interstitium is equally small and therefore Π is mainly determined by the BCOP – the osmotic pressure developed by the proteins in blood.

Once the pressure field has been found, the longitudinal velocity profile v_x can be fully determined based on equations (14) and (24). Moreover the interfacial velocity can be determined:

$$v_{int} = \delta \left(c_1 \cdot e^{\sqrt{k}x} + c_2 \cdot e^{-\sqrt{k}x} \right) \tag{25}$$

Consider now the y-momentum component of equation (3). Due to the low Re for this problem, the inertial terms can be readily neglected, thus yielding:

$$0 = \underbrace{-\frac{\partial P}{\partial y}}_{\sim \frac{\triangle_T P}{h}} + \underbrace{\mu \frac{\partial^2 v_y}{\partial y^2} + \mu \frac{\partial^2 v_y}{\partial z^2}}_{\sim \mu \frac{v_T}{D_H^2}} + \underbrace{\mu \frac{\partial^2 v_y}{\partial x^2}}_{\sim \mu \frac{v_T}{L^2}} \tag{26}$$

Following the same discussion as in equation (10), the longitudinal derivative is negligible because $\left(\frac{D_H}{L}\right)^2 << 1$. Moreover, consider that the transverse velocity is significantly smaller than the longitudinal velocity – dimensional analysis of eq. (8) shows that $v_T \sim \frac{D_H}{L} v_L << v_L$ – and therefore this model corresponds to a slender flow. In slender flows, the transverse velocity is so small that streamlines are aligned or practically parallel to each other, and therefore, the transverse pressure variations $\triangle P_T$ –that

cause transverse accelerations– are also necessarily small to maintain the alignment. In accordance with this flow slenderness, the pressure gradient term in equation (26) can be neglected to yield a simplified y-momentum equation from where the transverse velocity v_y can be obtained:

$$\frac{\partial^2 v_y}{\partial y^2} + \frac{\partial^2 v_y}{\partial z^2} = 0 \tag{27}$$

The equation can be solved by separation of variables and considering non-slip boundary conditions on the lateral and lower walls of the channel and $v_y(h/2, z) = v_{int}$

$$\begin{aligned} v_y(x,y,z) = &\quad \sum_{n=0}^{\infty} C_n \left(e^{\frac{(2n+1)\pi}{w} y} - e^{-\frac{(2n+1)\pi}{w}(y+h)} \right) \cos \frac{(2n+1)\pi}{w} z \\ C_n = &\quad \frac{4\cdot(-1)^n}{h\left(e^{\frac{(2n+1)\pi}{w}\frac{h}{2}} - e^{-\frac{(2n+1)\pi}{w}\frac{3h}{2}} \right)} \frac{w}{(2n+1)\pi} v_{int}(x) \end{aligned} \tag{28}$$

The wall shear stress along the direction of the flow can also be estimated by neglecting longitudinal derivatives as:

$$\tau_w(x,z) = -\mu \frac{\partial v_x}{\partial y} = Pl(x) \cdot h \left[\frac{1}{2} - 4 \cdot \sum_{n=0}^{\infty} \frac{\cosh\left((2n+1)\frac{\pi z}{h}\right)}{(2n+1)^2 \pi^2 \cosh\left((2n+1)\frac{\pi w}{2h}\right)} \right] \tag{29}$$

which allows to estimate the shear that an endothelium monolayer seeded on the inner side of the membrane would suffer as a result of the fluid flow.

The principal results of the model for the pressure and interfacial velocity are presented in Fig. 5.4. The pressure field and pressure gradient (Fig. 5.4a) as well as the filtration velocity (Fig. (5.4b)) are determined by the channel design, the permeability δ and the inlet and outlet pressures P_1 and P_2.

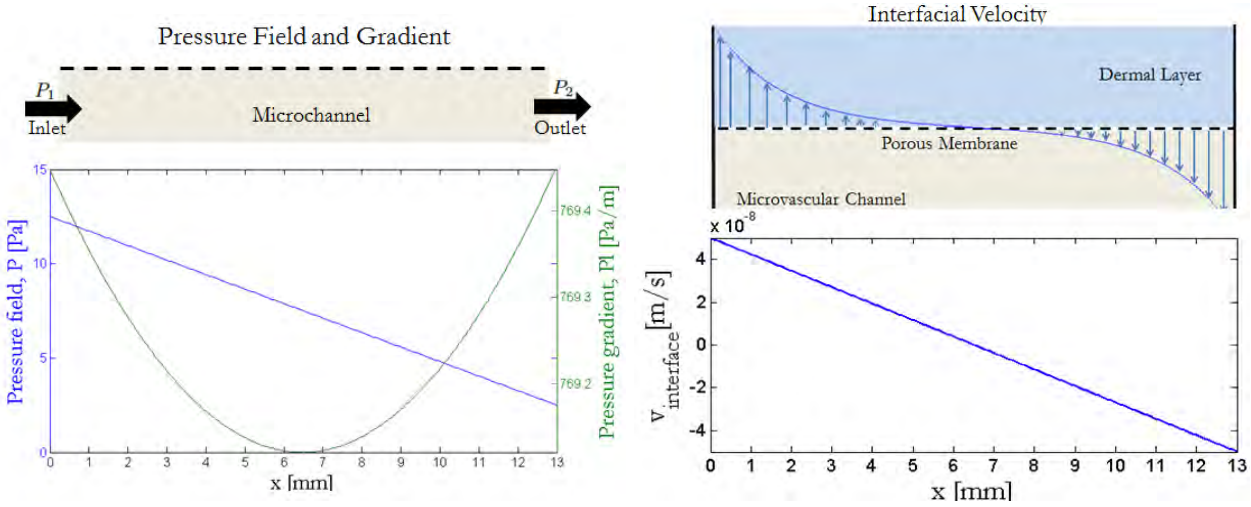

(a) Pressure field and pressure gradient in the channel

(b) Interfacial or filtration velocity ($\delta = 10^{-8} m/Pa \cdot s$)

Figure 5.4: Main results for the pressure field, pressure gradient and filtration velocity of the mathematical model developed for the microvascular channel

By controlling flow conditions of the microfluidic circuit and choosing the appropriate membrane; the velocity profile, wall shear stress and interfacial velocity can be tailored to the desired application, which could prove important for drug delivery [83, 84] and mechanotrasduction studies [85–87]. Further information regarding the choice of parameters for the model can be found in Section 7.2 and Annex II.

In particular, the permeability of the membrane δ appears to be a critical parameter in the system, specially for the shape of the interfacial velocity (Fig. 5.5). Notice that large values of δ yield a very sharp-changing profile, characterized by significant peaks of filtration and reabsorption near the inlet and outlet respectively, while the net filtration is negligible for most of the length of the channel. On the other hand, lower values of δ lead to a smoother profile that is nearly linear for permeabilities in the order of $10^{-5}\mathrm{m} \cdot \mathrm{s}^{-1} \cdot \mathrm{Pa}^{-1}$.

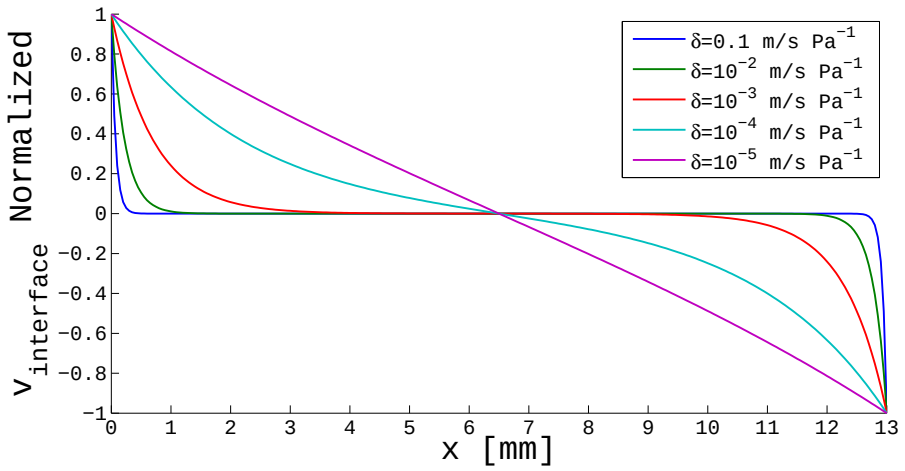

Figure 5.5: Dependency of the filtration or interfacial velocity (normalized) on the membrane permeability

5.2 Interstitial flow

The second step is to model the flow within the skin based on the previously found filtration profile. As described in section 3.2, the epidermis lacks blood vessels. Instead, it receives the oxygen and nutrients that diffuse from the capillaries present in the underlying dermis. Interstitial flow has been show to have a great impact on tissue and cell behavior, playing a role in morphogenesis, chemotaxis and angiogenesis [88] as well as tumor cell migration [89]. It has also been proposed as a core mechanism in bone mechanotransduction and osteoporosis [62]

Darcy's Law is an empirical constitutive model frequently used to describe fluid flow in porous media, including interstitial flow [90, 91]. In its differential form, it is expressed as:

$$\vec{v} = -\frac{\phi}{\mu}\nabla P \tag{30}$$

where $\vec{v}$ is the interstitial flow velocity, P is the interstitial pressure, μ is the fluid viscosity and ϕ is the *specific hydraulic conductivity.* While the *hydraulic conductivity* $\mathrm{m}^2/\mathrm{s}\cdot\mathrm{Pa}$ –that is flow rate per unit area (m/s) per unit pressure drop across unit length (Pa/m) [91]– described in the previous subsection

depends on the fluid viscosity, the specific hydraulic conductivity (units of m^2) is a property exclusively of the medium. It is also known as –and henceforth referred to as in the present work– permeability of the medium; and it is related to the characteristics of microscopic structure of the medium such as porosity (fraction of void volume) or specific surface (interface area-to-volume ratio).

In the SoaC device, the dermal layer is composed of a fibrin matrix with embedded fibroblasts and the epidermis is composed of a stratified squamous epithelium. For simplicity, the dermis is modeled as a single porous layer of length L, height H and uniform permeability ϕ. Furthermore, it is assumed that the layer is homogeneous and has isotropic properties[11] In the present work, both convective and diffusive transport are considered.

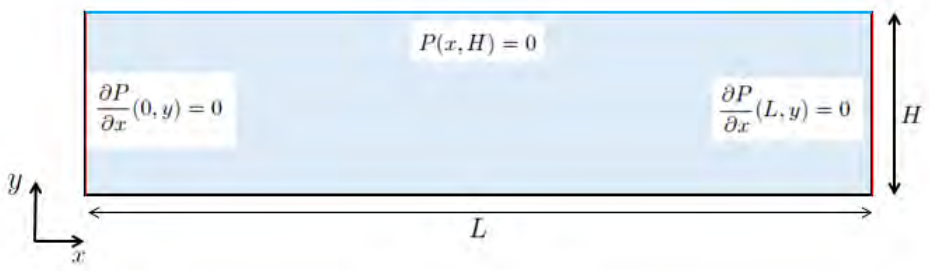

Figure 5.6: Mathematical representation of the dermal layer and boundary conditions

Taking the divergence at both sides of equation (30) and given that $\nabla \cdot \vec{v} = 0$ for an incompressible fluid, Darcy's Law can be converted into:

$$\nabla^2 P = 0 \tag{31}$$

assuming that the viscosity μ and the permeability ϕ are constant.

[11] Isotropy is particularly relevant for diffusion. Highly structured tissues tend to favor the diffusion of molecules in a particular direction (anisotropic diffusion) to acomplish a more efficient transport of said molecules. It is well documented in some cases, such as the brain and bone. However, the mathematical complexity of considering a diffusion tensor would be impractical for this model.

Equation (31) means that for the flow of an incompressible fluid within a porous media with uniform porosity, the pressure field $P(x, y)$ is a harmonic function. This equation can be supplement with the appropriate boundary conditions, presented in Fig. (5.6)

Boundary Conditions
$P(x, H) = 0$
$\frac{\partial P}{\partial x}(0, y) = 0$
$\frac{\partial P}{\partial x}(L, y) = 0$

The fourth boundary condition regards the interface of the dermis with the vascular channel. A continuity conditions applied to this interface requires:

$$\frac{\partial P}{\partial y}(x, 0) = -\frac{\mu}{\phi} v_{int} \tag{32}$$

This last expression couples the interstitial flow to the previously developed velocity profile within the channel by means of the velocity at the interface v_{int}. By using separation of variables, equation (31) can be solved for the general case:

$$P_1 = C_o(y - H) + \sum_{n=1}^{\infty} C_n \left(e^{-\frac{n\pi}{L} y} - e^{\frac{n\pi}{L}(y-2H)} \right) cos\left(\frac{n\pi x}{L} \right) \tag{33}$$

where C_o, C_n are coefficients determined by the fourth boundary condition given by eq. (32). The subscript 1 is used here to distinguish the pressure field from the one developed later on the chapter.

Taking into account the expression for the interfacial velocity previously developed (equation (25)), the particular solution for the pressure field is given by equation (33) with

$$C_o = -\frac{\mu\delta}{L\phi} \frac{1}{\sqrt{k}} \left(C_1 \left(e^{\sqrt{k}L} - 1 \right) - C_2 \left(e^{-\sqrt{k}L} - 1 \right) \right) \tag{34}$$

$$C_n = \frac{2\mu\delta}{n\pi\phi(e^{-2\frac{n\pi}{L}H} + 1)} \left(C_1 \frac{(-1)^n \sqrt{k} e^{\sqrt{k}L} - \sqrt{k}}{k + \left(\frac{n\pi}{L}\right)^2} - C_2 \frac{(-1)^n \sqrt{k} e^{-\sqrt{k}L} - \sqrt{k}}{k + \left(\frac{n\pi}{L}\right)^2} \right) \tag{35}$$

Once the pressure field is given, the velocity profile can be obtained from equation (30)

$$\vec{v}_1(x,y) = \begin{cases} v_x = \frac{\phi}{\mu} \sum_{n=1}^{\infty} C_n \left(e^{-\frac{n\pi}{L}y} - e^{\frac{n\pi}{L}(y-2H)} \right) \frac{n\pi}{L} \sin\left(\frac{n\pi x}{L}\right) \\ v_y = \frac{\phi}{\mu} \left[-C_o + \sum_{n=1}^{\infty} C_n \left(e^{-\frac{n\pi}{L}y} + e^{\frac{n\pi}{L}(y-2H)} \right) \frac{n\pi}{L} \cos\left(\frac{n\pi x}{L}\right) \right] \end{cases} \tag{36}$$

The pressure field and velocities (Fig. 5.7) present the filtration-reabsorption characteristics described in Section 3.2. The higher pressures on the left side of the dermis (corresponding to the entrance of the channel) cause the interstitial fluid to circulate towards the lower pressures on the right part of the region, where it is reabsorbed back into the channel.

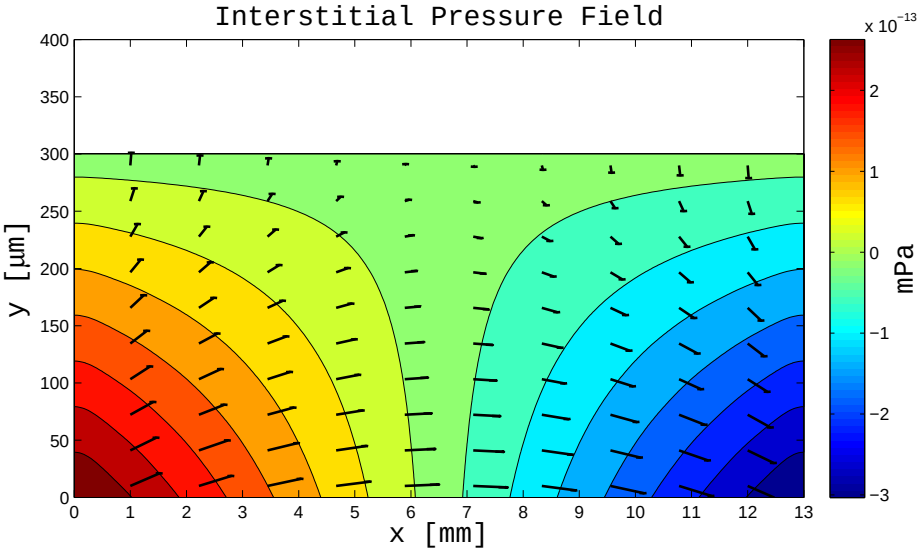

Figure 5.7: Interstitial pressure and velocity within the dermis. Velocities within the interstititum (black arrows) are in the order of 10^{-8}m/s for the vertical velocities and 10^{-9}m/s for the horizontal ones.

This model, however, considers that the epidermis has a negligible thickness and is highly permeable and therefore (fluidically) conductive, so that the upper surface of the dermal layer is exposed to an uniform atmospheric pressure. As a result, the flux through this upper surface is non-zero.

This approximation is valid for the early stages of suprabasal differentiation, when the epidermis is

still composed of an epithelial monolayer. For later stages of differentiation, once the epidermis is fully formed, the stratum corneum and the lipidic layer secreted by the stratum granulosum form a relatively impermeable barrier. Under these circumstances, the boundary condition for the outer surface can be replace by a zero-flux condition, i. e. $\frac{\partial P}{\partial y}(x, H) = 0$, while all the other conditions remain unchanged. Following the same procedure as before, equation (31) can be solved by the method of separation of variables to yield the interstitial pressure field:

$$P_2 = C_o + \sum_{n=1}^{\infty} C_n \left(e^{-\frac{n\pi}{L}y} + e^{\frac{n\pi}{L}(y-2H)} \right) cos\left(\frac{n\pi x}{L} \right) \tag{37}$$

$$C_n = \frac{2\mu\delta}{n\pi\phi(e^{-2\frac{n\pi}{L}H} - 1)} \left(C_1 \frac{(-1)^n \sqrt{k} e^{\sqrt{k}L} - \sqrt{k}}{k + \left(\frac{n\pi}{L}\right)^2} - C_2 \frac{(-1)^n \sqrt{k} e^{-\sqrt{k}L} - \sqrt{k}}{k + \left(\frac{n\pi}{L}\right)^2} \right) \tag{38}$$

where C_o is a constant that cannot be determined from this problem, since all boundary conditions refer to derivatives of P. In this regard, it makes little sense to study the pressure field, but rather the interstitial velocity field it generates (Fig. 5.8). Applying equation (30) to the pressure field above, the velocity field can be readily obtained:

$$\vec{v}_2(x, y) = \begin{cases} v_x = \frac{\phi}{\mu} \sum_{n=1}^{\infty} C_n \left(e^{-\frac{n\pi}{L}y} + e^{\frac{n\pi}{L}(y-2H)} \right) \frac{n\pi}{L} \sin\left(\frac{n\pi x}{L} \right) \\ v_y = \frac{\phi}{\mu} \sum_{n=1}^{\infty} C_n \left(e^{-\frac{n\pi}{L}y} - e^{\frac{n\pi}{L}(y-2H)} \right) \frac{n\pi}{L} \cos\left(\frac{n\pi x}{L} \right) \end{cases} \tag{39}$$

The vertical velocity field (Fig. 5.8, left) is characterized by filtration and reabsorption towards the entrance and the exit of the channel respectively in the lower regions of the dermis that diminishes towards upper regions. On the other hand, the horizontal velocity field (Fig. 5.8, right) presents low velocities at either end of the chamber and higher velocities towards the center. Notice that in this second case, the horizontal velocities are significantly larger than in the previous case (10^{-7} m/s vs 10^{-9} m/s) because the impermeability of the epidermis forces a higher circulation of fluid from the regions of filtration to those of reabsorption.

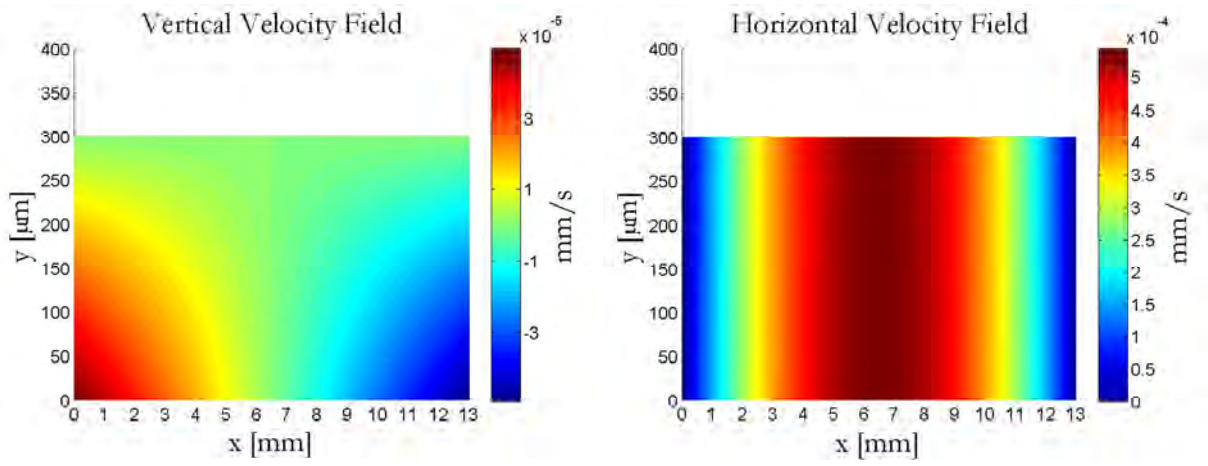

Figure 5.8: Interstitial velocity (in mm/s) for the vertical (left) and horizontal (right) directions when the epidermis is modeled as an impermeable barrier

These two versions of the model represent extreme conditions, and *in vivo* the situation is likely to be a combination of both. Moreover, there are two phenomena that are not considered in the present work. Firstly, the SoaC device does not include a lymphatic system that can drain excess interstitial fluid as described in Section 3.2. Secondly, although the epidermis is regarded as a barrier for dehydration, an average adult loses 400 ml of water per day through the skin due to evaporation. Given the low magnitude of the interstitial velocities, the effect of water evaporation through the outer surface may be non-negligible, specially for the first case.

5.3 Oxygen delivery

To develop a conservation equation for the oxygen concentration, consider a fluid volume $V_f(t)$ limited by an external boundary $\Sigma_f(t)$. According to Reynolds transport theorem, the total change with time of an intensive magnitude $\phi(\vec{x}, t)$ (in the present case $\phi(\vec{x}, t)$ is the concentration of oxygen) contained within the fluid volume is given by:

$$\frac{d}{dt}\int_{V_f} \phi dV = \frac{d}{dt}\int_{V_c} \phi dV + \int_{\Sigma_c} \phi(\vec{v} - \vec{v_c}) \cdot n d\sigma \tag{40}$$

where $V_c(t)$ and $\Sigma_c(t)$ are a control volume and its boundary that coincide with $V_f(t)$ at time t. In simple terms, the time variation of an intensive magnitude$\phi(\vec{x}, t)$ within a fluid volume is equal to the time variation of that magnitude within a control volume $V_c(t)$ and the convective flux of said magnitude across the boundary $\Sigma_c(t)$

Based on this idea, a more intuitive, albeit less formal method can be followed to develop a conservation equation (Fig. 5.9). Consider this time a volume V with a velocity $\vec{v_c}$ and bounded by a surface Σ. We wish to find an expression for the time variation of the oxygen concentration, $C(\vec{x}, t)$, within this volume. A common form of conservation laws can be expressed as:

Rate of change of a magnitude = Flux through the boundaries + Production - Consumption (41)

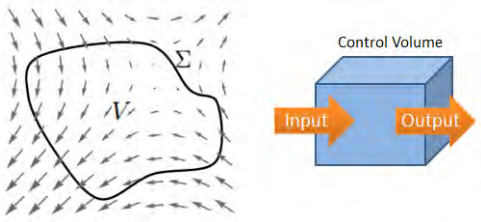

Figure 5.9: Control volume and flux through the boundaries

There are two sources of mass transport that can be taken into account when considering the flux of oxygen through the boundary, namely convection and diffusion.[12] Convective flux of oxygen corresponds to the second term on the right-hand side of equation (40) : $Q = \int_{\Sigma_c} C(\vec{v} - \vec{v_c}) \cdot n d\sigma$. On the other hand, diffusive transport can be modeled by Fick's first law $J = -D\nabla C$. The resulting conservation equation is presented below:

[12] By convention, the unit surface normal $\hat{n}$ that defines an orientable surface Σ points towards the outside of the surface. As a result, the surface integral (flux) of a vector field $F(\vec{x})$ across Σ is positive when $F(\vec{x})$ flows towards the outside and negative when it flows into the volume enclosed by Σ. Therefore, a negative sign should be include in the flux term in (41) to account for this effect, as can be observed in (42).

$$\frac{d}{dt}\int_V C dV + \int_\Sigma C(\vec{v} - \vec{v_c}) \cdot \vec{n} d\sigma = \int_\Sigma D\nabla C \cdot \vec{n} d\sigma - \int_V \psi dV \tag{42}$$

Where $\psi(x, y, z)$ is the oxygen consumption per unit volume at point (x, y, z). By applying Gauss's theorem to (42) and considering a constant diffusion coefficient D and an incompressible fluid ($\nabla \cdot \vec{v} = 0$), a conservation equation for the concentration of oxygen in differential form can be readily obtained:

$$\frac{\partial}{\partial t}C + \vec{v} \cdot \nabla C = D\nabla^2 C - \psi \tag{43}$$

Based on reaction kinetics, the oxygen consumption $\psi(x, y, z)$ can be expressed as a function of the concentration. If the oxygen consumption is considered a zeroth order reaction, then $\psi = R_{O_2}$independently of the oxygen concentration. For a first order reaction, the oxygen consumption depends linearly on the concentration, i.e. $\psi = \kappa C$ with κ a rate constant that depends on the cell type. A more elaborate model considers an enzyme-mediated mechanism of oxygen consumption based on Michaelis-Menten kinetics:

$$\psi = \frac{R_{max} C}{K_M + C} \tag{44}$$

However, the Michaelis constant (K_M) is extremely low compared to typical values of oxygen concentration [92], and therefore the Michaelis-Menten mechanism can be approximated as a zero-order reaction for concentrations that are not critically low. This simplification of (43) yields the following conservation law in differential form:

$$\frac{\partial}{\partial t}C + \vec{v} \cdot \nabla C = D\nabla^2 C - R_{O_2} \tag{45}$$

The present work considers only steady-state oxygen transport since temporal fluctuations on the level of oxygen transported through the microchannel are not taken into account. Therefore the left-hand side of equation (45) is zero. Furthermore, consider a dimensional analysis of the equation:

$$\underbrace{\vec{v} \cdot \nabla C}_{\sim v/H} = \underbrace{D\nabla^2 C}_{\sim D/H^2} - R_{O_2} \tag{46}$$

The relative magnitude of the convective and diffusive terms is given by the Péclet number $Pe = Hv/D$, where H is the thickness of the skin, v is a characteristic interstitial velocity and D is the diffusion coefficient. The diffusion coefficient for oxygen in water is in the order of 10^{-9} m^2/s, and in this model, $H \sim 10^{-4}$ m and $v \sim 10^{-8}$ m/s, and therefore $Pe << 1$ so convective terms can be neglected. The resulting simplified equation is:

$$D\nabla^2 C = R_{O_2} \tag{47}$$

Consider a modified Krogh model [93] in which the skin is formed by two adjacent layers of thickness H_1 and H_2 that represent the dermis and the epidermis respectively (Fig. 5.10). Each layer has a different but uniform diffusion coefficient D_1, D_2 and oxygen consumption rate R_1, R_2. Moreover, assume for simplicity that the concentration at the interface with the microvascular channel does not depend on the position along the channel and is given by a constant C_o. This approximation is only valid when the convective transport of oxygen along the channel is faster than its diffusive transport to the hydrogel, but is taken here to reduce the model to a 1D problem.

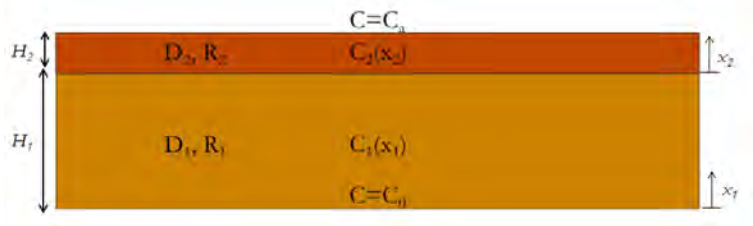

Figure 5.10: Two-layer model of the dermis and the epidermis for oxygen diffusion-consumption and boundary conditions

Finally, the concentration at the interface with the atmosphere is given by another constant C_a. This concentration can be calculated based on Henry's law $C_a = k_H P_{O_2}$ with k_H a solubility constant for oxygen in water. P_{O_2} is the partial pressure of oxygen in the gas phase, given by $P_{O_2} = \chi_{O_2}(P + P_o)$, where χ_{O_2} is the molar fraction of oxygen in the gas phase, P is the gauge pressure and P_o is the atmospheric pressure. The system of 1D diffusion-reaction equation and the boundary conditions are presented below:

$$\begin{cases} D_2 \frac{\partial^2 C_1}{\partial x_1^2} = R_1 \\ D_1 \frac{\partial^2 C_2}{\partial x_2^2} = R_2 \end{cases} \tag{48}$$

Boundary Conditions for C_1, C_2	Coupling Conditions
$C_1(x_1 = 0) = C_o$	$C_1\,(x_1 = H_1) = C_2\,(x_2 = 0)$
$C_2(x_2 = H_2) = C_a$	$D_1 C_1^{'}\,(x_1 = H_1) = D_2 C_2^{'}\,(x_2 = 0)$

Integrating each equation and considering boundary conditions, the following solution is obtained:

$$C_{_1}(x_1) = \frac{R_1}{2D_1}x_1^2 + A_1 x_1 + B_1 \tag{49}$$

$$C_{_2}(x_2) = \frac{R_2}{2D_2}x_2^2 + A_2 x_2 + B_2 \tag{50}$$

$$\begin{aligned} A_1 &= \tfrac{D_2}{D_1H_1+D_2H_2}\left[(C_a - C_o) + \tfrac{R_1H_1^2}{D_1} - \left(\tfrac{R_1}{2D_1}H_1^2 + \tfrac{R_2}{2D_2}H_2^2\right) - R_1H_1\left(\tfrac{H_2}{D_2} + \tfrac{H_1}{D_1}\right)\right] \quad B_1 = C_o \\ A_2 &= \tfrac{D_1}{D_1H_1+D_2H_2}\left[(C_a - C_o) + \tfrac{R_1H_1^2}{D_1} - \left(\tfrac{R_1}{2D_1}H_1^2 + \tfrac{R_2}{2D_2}H_2^2\right)\right] \quad B_2 = C_o + \tfrac{R_1}{2D_1}H_1^2 + A_1H_1 \end{aligned} \tag{51}$$

The oxygen concentration profile (Fig. 5.11) developed in this model follows a piece-wise ($x_1 = x$ and $x_2 = x - H_1$) parabolic shape with a minimum located between the two main sources of oxygen: the microvascular channel and the atmosphere. This atmospheric source of oxygen arises from the model when considering a non-zero concentration of oxygen at the interface between the epidermis and the atmosphere C_a. Thus, by taking into account the presence of atmospheric oxygen and its solubility, this model reproduces the oxygen uptake through the skin that has been reported before [94]. This additional supply of oxygen to the outer layers of the dermis and epidermis contributes to the overall oxygen delivery to the skin, allowing the cells to survive farther away from a capillary than usual. Notice, in fact, that the epidermis and the outer dermis are mostly supplied by this external source rather than the oxygen transported by the channel.

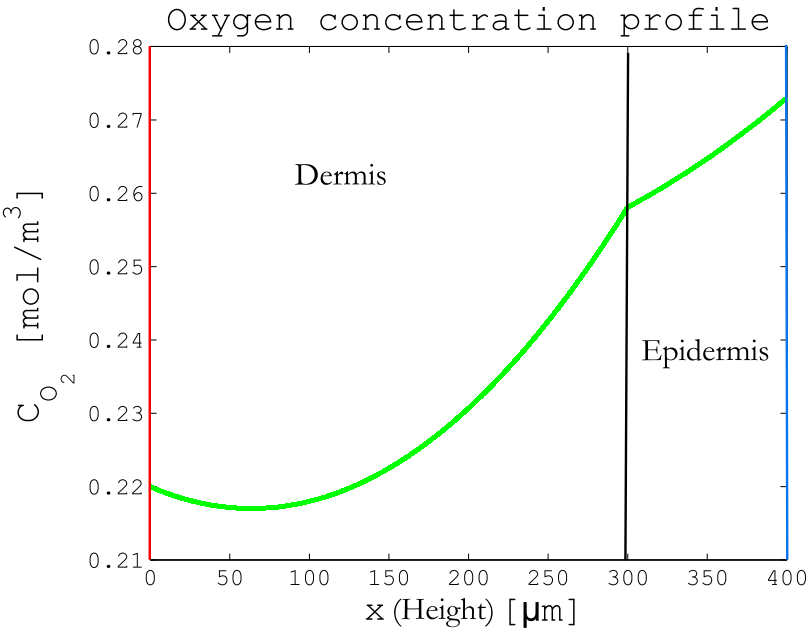

Figure 5.11: Results for the oxygen concentration profile in the dermis and epidermis

Due to the small thickness of the skin considered in this device –the thickness of the dermis, H_1, is taken to be 300 μm and that of the epidermis, H_2, around 100 μm– there is no hypoxic or anoxic region and all the cells receive a sufficient supply of oxygen.

For thicker tissue constructs, or for tissues not supplied by atmospheric oxygen, a hypoxic region can be found. The levels of oxygen in this region are so low that cells cannot properly perform aerobic respiration, and lactate and other wastes accumulate. From a mathematical standpoint, the concentration can reach negative values, which correspond to an anoxic region. Notice, however, that at low levels of oxygen the reaction follows Michaelis-Menten kinetics and thus the amount of oxygen consumed decreases.

Equation (47) can be adapted to the transport of other substances such as CO_2 or to the absorption of drugs by adjusting the reaction rates, diffusion coefficients and the levels at the interface with the microchannel and with the atmosphere. In the case of CO_2 transport, the sign of the reaction rate must be inverted to account for production rather than consumption. Notice, however, that for larger molecules such as drugs, the diffusion coefficient may be several orders of magnitude smaller and hence,

convective transport could play a role in their absorption. Moreover, it is worth to note that the barrier function of the stratum corneum severely hinders drug absorption, and therefore a specific model of drug penetration through the stratum corneum has to be developed.

For instance, consider the steady state absorption of a drug after its application as an ointment on the outer surface of the skin. The concentration of the drug in the immediate interface between the drug and the skin is taken to be C_D, while the concentration in the microvascular channel is assumed to remain zero due to the fast clearance rates from convective transport. $D_1,\ D_2$ and $R_1,\ R_2$ are the diffusion coefficients and the metabolism rate of the drug for the dermis and the epidermis respectively. A rough estimate of the absorption rate (in moles per unit area of interface for unit time) can be given by the diffusive flux of drug into the microvascular channel

$$J_D = \frac{D_1 D_2}{D_1 H_1 + D_2 H_2}\left[C_D + \frac{R_1 H_1^2}{D_1} - \left(\frac{R_1}{2D_1}H_1^2 + \frac{R_2}{2D_2}H_2^2\right) - R_1 H_1\left(\frac{H_2}{D_2} + \frac{H_1}{D_1}\right)\right]\ \frac{\text{mol}}{\text{m}^2 \cdot \text{s}} \tag{52}$$

The diffusion coefficients and reaction rates have to be determined experimentally for each drug studied, but this model serves as a foundation for more sophisticated drug absorption studies.

5.4 Limitations of the model

Modeling transport in the skin is highly a complex and many different approaches have been taken [95]. To simplify this complexity, the model in the present work is developed under several assumptions:

(1) The fluid in the channel is newtonian with constant viscosity μ and density ρ.

(2) The flow is slender and inertial forces are negligible.

(3) The membrane and endothelium are impermeable to high molecular mass proteins, which develops an oncotic pressure Π

(4) The interstitial flow within the dermis can be modeled with Darcy's Law.

(5) The permeability of the dermis ϕ is uniform and isotropic

(6) Convective transport in the interstititum is negligible.

(7) The oxygen concentration in the channel is uniform and steady, i.e. no longitudinal or temporal variations in C_o.

(8) The mass-transfer resistance through the endothelium and the membrane is negligible [82]

(9) Oxygen diffusion in the dermis and epidermis is isotropic and uniform with a constant diffusion coefficient: $D_1,\ D_2$

(10) Oxygen consumption by the dermis and epidermis is uniform and follows a zeroth order reaction regardless of oxygen concentration: $R_1,\ R_2$

The first assumption is valid under the condition that cell culture media or a similar fluid (with a high water content) is used in the device, since their behavior is mainly newtonian. However, if a more blood-like fluid is used, specially if it contains red blood cells, a more complex rheological model, such as Casson's Law should be considered. Assumptions (2) and (6) are justified given the low aspect ratio, $D_H/L << 1$, and low Reynolds and Péclet numbers, $Re,\ Pe << 1$, but may not extended to other flow conditions. Regarding assumption (4), Darcy's law neglects viscous forces within the fluid, which is only valid if ϕ is low, and hence the model does not satisfy non-slip boundary conditions at the walls. A more elaborate model could incorporate the Brinkman equation to take into account viscous terms.

Assumption (3) is key to obtain a filtration-reabsorption profile. The endothelial monolayer is impermeable to large molecules, such as proteins and plasma expanders, that can be used to establish the osmotic pressure required. On the other hand, the endothelium is mostly permeable to oxygen, which justifies assumption (8). Moreover, the conditions regarding isotropy and uniformity (assumptions (5), (9) and (10)) are justified upon homogeneous cell density and composition of the fibrin hydrogel, but may not be applicable to real skin. Finally, the use of zero-order kinetics is based on the assumption that the oxygen concentration is large compared to the Michaelis constant K_M and thus $\frac{R_{max}C}{K_M+C} \approx R_{max}$.

Given the atmospheric oxygen uptake and the relatively low rate of oxygen consumption by the skin, longitudinal variations on the oxygen concentration within the channel are considered negligible (assumption (7)). More sophisticated models can incorporate longitudinal variations due to oxygen consumed as well as oxygen-hemoglobin binding kinetics if red blood cells are included.

Overall, the model offers a simplified view on the device operation that can serve as starting point to quantitatively predict its behavior.

6 Fabrication of the skin-on-a-chip device

Microfabrication refers to a wide array of techniques used to manufacture devices with features in the micrometer scale. Although initially developed for the semiconductor industry, these methods have been adapted to a variety of other fields and applications such as sensors, microfluidics, lab-on-a-chip technologies, BioMEMS or surface patterning. In fact, the name organ-on-a-chip stems from the use of fabrication technologies historically used in the microelectronic industry to produce microchips.

Poly(dimethylsiloxane) or PDMS is a silicone elastomer that has become the material of choice for microfluidics thanks to its outstanding properties [96]. PDMS is inexpensive, soft and easy to handle. It can be thermally cured at low temperatures and is capable of replicating features down to nanometer scale, allowing low-cost, sub-micrometer, high fidelity reproduction of a mold with little equipment requirements. Furthermore, its softness allows PDMS parts to contact surfaces without damaging them and facilitates demolding. From an optical point of view, PDMS is transparent down to 280 nm (DUV) and non-fluorescent, making it an ideal candidate for optical MEMS [97, 98]. Due to its elastomeric nature, PDMS presents hyperelastic properties, allowing it to reversibly undergo significant deformations.

From a chemical point of view, PDMS is very inert due to the presence of methyl groups in the polymer backbone, non-toxic, biocompatible and highly permeable to gases. The surface of PDMS is remarkably hydrophobic, preventing cell attachment and favoring adsorption of certain species to the surface. Hydrophobic microchannels present several challenges: they are difficult to fill with fluids commonly used in microfluidics due to the contact angle and they tend to trap and nucleate bubbles, especially at sharp corners. The surface can temporarily be rendered hydrophilic by oxygen (or room air) plasma treatment, but the presence of polar silanol groups on the surface is transient and it fully recovers its hydrophobicity within 30 minutes [99], although it can be prolonged by keeping the surface in contact with water.

These properties make PDMS the ideal choice for microfluidic cell culture applications, such as the present skin-on-a-chip device. A series of microfabrication techniques collectively known as soft

lithography [100] have been developed specifically to work with PDMS (or other elastomers in general). The most common technique to produce microfluidic devices is replica molding.[13] Replica molding involves the casting of PDMS on an master mold typically made of SU-8 and manufactured with photolithography techniques.

This section explores the various microfabrication techniques used to manufacture the components of the skin-on-a-chip device, the selection of an appropriate porous membrane and the surface functionalization strategy developed to assemble the device.

6.1 Fabrication of the master molds

All microfluidic applications begin with the fabrication of a master mold –or simply master– by photolithography. Photolithography is a technique that employes light to create a pattern of a photosensitive resin on the surface of a substrate (typically Si or Glass). PDMS casted on this master replicates said features, presenting the negative pattern on its surface.

This section describes the basic microfabrication techniques used to produce photomasks and a SU-8 masters. The procedure presented here was used to fabricate a micropillar array for microimprinting of the PDMS membrane; while the microfluidic masters were acquired from microLIQUID S.L. following the specification presented in Section 4

6.1.1 Fabrication of the photomask

The first step in any photolithography process is the fabrication of a photomask or simply, mask. Photomasks are binary patterns that allow a selective exposure of the light-sensitive photoresist. Thus, a photomask must be transparent in those regions that want to be exposed and fully opaque to the given wavelength otherwise in order to properly transfer its pattern to the photoresist.

Masks can be made in a variety of scales and materials following different techniques. Typical materials include acetate, gold-palladium (AuPd) on glass or chrome. The material determines the cost, chrome

[13] Replica molding initially referred to the replication of PDMS molds in different materials

ones being the most expensive, as well as the quality. In turn, the quality and material of the photomask often limits the resolution of the photolithography step and the definition of the edges.

In the present work, an AuPd photomask was fabricated on glass for the successive photolithography steps. AuPd masks can be produced in a few hours at a relatively low cost, although they present low quality and resolution, making them ideal candidates for rapid prototyping in photolithography.

The mask was fabricated on a 20x40 mm laser-cut microscopy glass slide (Microcrown). The glass slide was thoroughly cleaned with the same wafer cleaning techniques described in Section 6.1.2 and Figure 6.3. The clean glass slide was introduced in a sputtering system (SC7620 mini sputter coater, 10 mA current) at a distance of $\sim 23\,\text{mm}$ from the AuPd target for 9 minutes, during which a thin film of metal was deposited on one of the glass surfaces. The thin film was then patterned via laser ablation with a KrF 248 nm excimer laser (ATLEX 300 I) operating at a frequency of 200 Hz and 25% attenuation with an energy of 10 mJ and 10 pulses per spot. This process yielded a glass slide with a patterned AuPd film that is opaque to the DUV light used in contact photolithography (Fig. 6.2). A summary of the steps followed to fabricate the mask is presented in Figure 6.1.

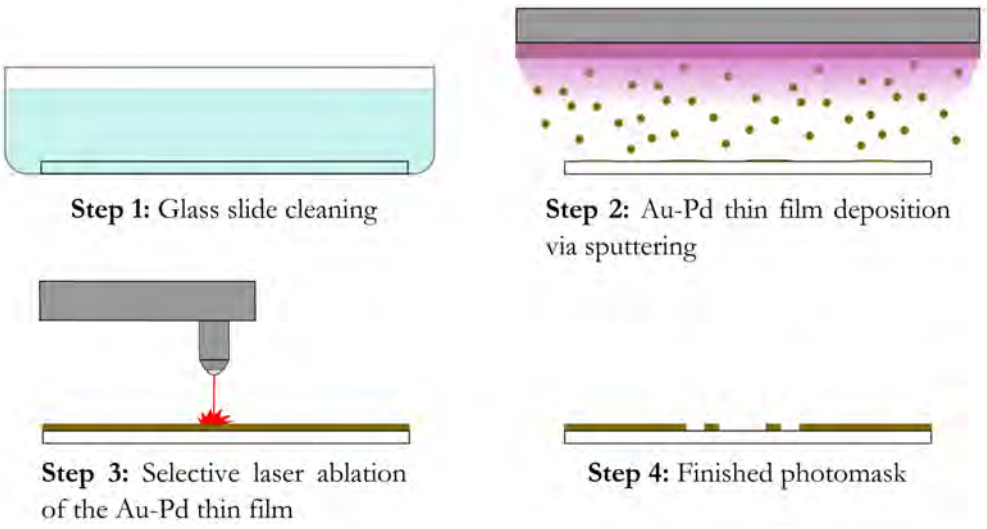

Figure 6.1: Summary of the key steps to fabricate a AuPd photomask for selective exposure during photolithograpry

Proper cleaning of the substrate is essential to ensure adhesion of the metal layer produced during the posterior deposition. In the sputtering system, a vacuum is generated within the chamber and plasma is produced to bombard the AuPd target, detaching metals atoms that deposit on the glass slide beneath. Any debris or contamination on this substrate can interfere with the deposition process, leading to poor adherence and detachment of the metal layer, causing failure of the mask.

The AuPd film deposited with this process is susceptible to laser ablation. A laser excimer produces short pulses of high energy that cause material removal by non-thermal processes (photochemical bond breaking), making the mask transparent in the specified areas. This process, however, is relatively aggressive or *explosive* and thus yields poorly defined or rough edges as seen in figure 6.2.

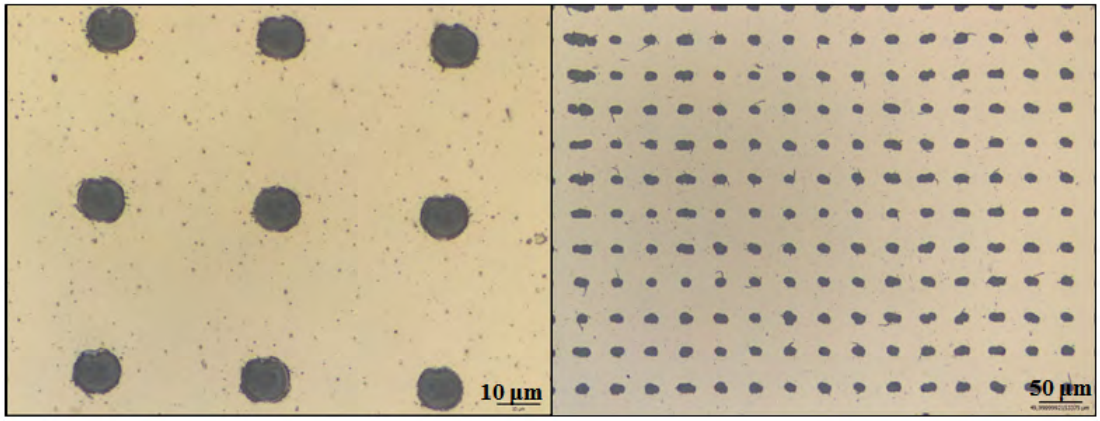

Figure 6.2: AuPd photomask for the master with micropillars at 100x (left) and 20x (right). The low definition is caused by the ablation process and mechanical errors in the laser machine

6.1.2 Photolithography

Photolithography is the most widely used microfabrication technique and the starting step in the production of microfluidic devices. It is based on the patterning of a photoresist film by selectively exposing it through a photomask. Photoresists are light-sensitive resins whose solubility properties in an specific developer change upon exposure. In this regard, resist can be positive, if the exposed regions become soluble in the developer; or negative, if the regions exposed to light become cross-linked and insoluble.

The thin film of photoresist to be patterned must be deposited on a substrate, typically Si or Glass. In traditional photolithrography processes for the microelectronic industry, the pattern of the photoresist served as mask to pattern the underlying substrate, while in the present work it is used as master mold for the microfluidic device.

SU-8 is a chemically amplified, epoxy-based negative photoresist commonly used in microfluidic masters. SU-8 allows for high aspect ratios with straight sidewalls due to its low absorption to UV light.

Prior to the photoresist deposition, the wafer has to be thoroughly cleaned to eliminate any contamination that may interfere with the photolithography process. Metallic and organic residues on the wafer form an inhomogeneous surface, and remaining dust particles or bubbles in the photoresist are forced outwards during spin coating, forming tail-like traces known as comets. Moreover, after activation, a native silicon oxide layer begins growing on the surface of the silicon wafer upon contact with the atmosphere.

Different methods can be used to eliminate different kinds of residues, which makes wafer cleaning a complex process that must be determined empirically for the desired application [101]. The present work describes a protocol for Si and Glass wafer cleaning that is effective for the fabrication of SU-8 masters with resolutions down to 10 µm.

The Si wafer was cleaved with a sharp metal tip to the desired dimensions (20x40 mm). The resulting chips were submerged in acetone and subjected to an ultrasound bath for 2 minutes, after which the process was repeated in DI water for another 2 minutes to detach and eliminate the fine particulate that remained adhered to the surface. The chips were dried with filtered compressed air and introduced in a piranha solution containing a 2:1 mixture of sulfuric acid and hydrogen peroxide (2:1 H_2SO_4: H_2O_2). The piranha solution was allowed to react with the chips for 30 minutes, producing a highly exothermic and oxidizing reaction to remove any organic contamination and to increase the hydrophilicity of the surface.

After the piranha treatment, the chips were carefully extracted from the solution with acid-resistant tweezers and rinsed with DI water injected with a filtered syringe. The chips were then dried with

filtered compressed air to prevent water evaporation, which could leave evaporation stains on the surface. Finally, the chips were placed on a hot plate at 120°C for 30 minutes to achieve thermal desorption, preventing the formation of the native oxide layer. After the cleaning process, the chips were stored in a laminar flow hood until further use. A summary of the cleaning protocol is presented in Figure 6.3.

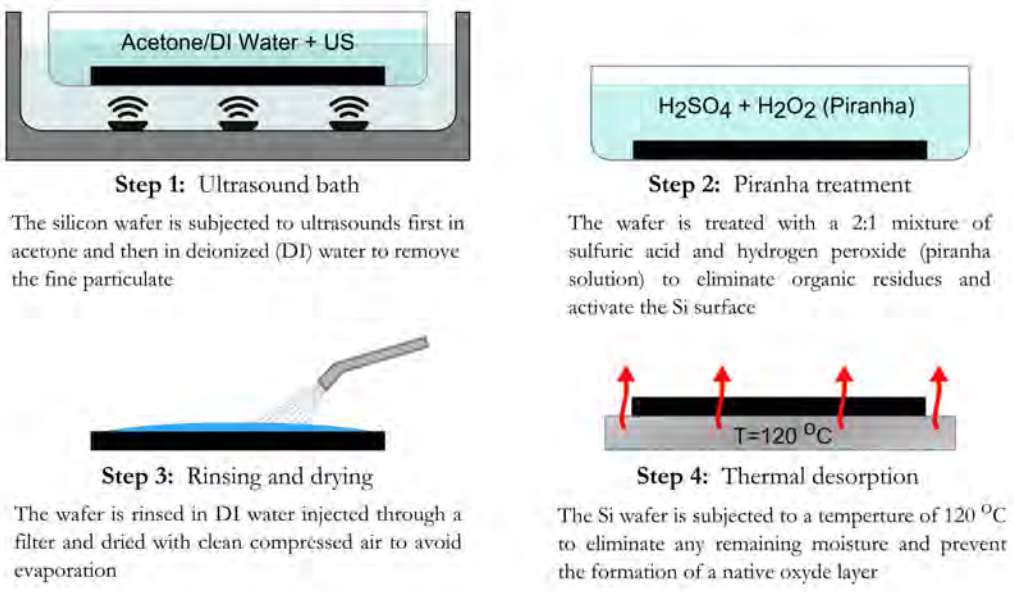

Figure 6.3: Summary of the wafer cleaning steps

One of the most common techniques for photoresist deposition is spin coating. In this process, a drop of the material to deposit is poured on the substrate (Fig. 6.4, left), which is secured on the spinner stand by a vacuum system. The system then accelerates to speeds of thousands of rpm, using the centripetal force to spread the photoresist over the surface, forming a thin film with even thickness (Fig. 6.4, right). The thickness of films produced by spin coating is determined by the spinning speed, the viscosity of the material and the adhesion with the substrate. Excess material tends to accumulate on the edges of the substrate, increasing the thickness on the rim by several folds. This phenomenon is known as edge effect.

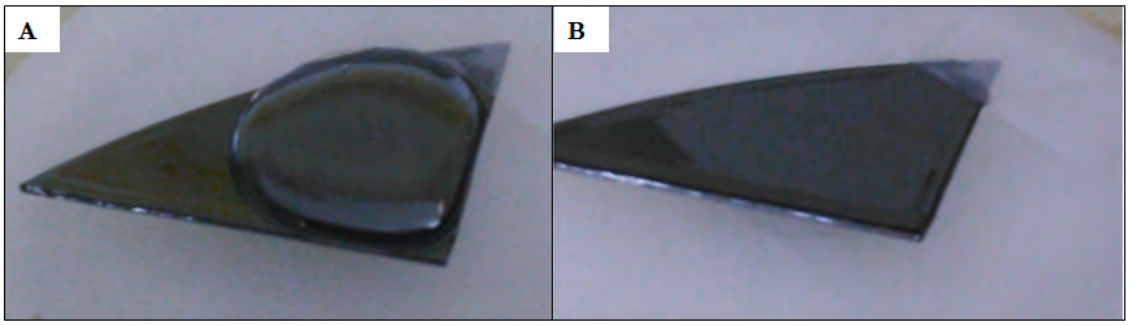

Figure 6.4: Deposition of a thin film by spin coating on Si substrate. (A) A drop of the material to be deposited on the Si substrate before spinning (B) Thin film formed after spinning. Notice the edge effects on the rim of the substrate

In the development of the skin-on-a-chip device, several SU-8 masters featuring a micropillar array were fabricated by spin coating and contact lithography following the method presented below.

After cleaning the Si chips, SU-8 2100 (Microchem) was deposited on the substrate by spin coating (Laurell. WS-400E-6NPP-LITE) with an initial speed of 1000 rpm for 30 seconds to allow spreading over the surface followed by second spinning step at 6000 rpm for 1 minute which yielded a thickness of $\sim 30\,\mu m$. The chips with the SU-8 deposits were soft-baked (prebaked) on a hot plate at 70°C for 5 minutes to eliminate excess solvent and minimize adhesion with the mask. The previously fabricated AuPd mask was then brought into contact with the SU-8 and held between two glass slides while low pressure was applied. The photoresist was exposed with a MA-6 aligner (Süss MicroTec) to UV light at $10\,mW/cm^2$ through the mask for 80 seconds.

After exposure, the chips were subjected to a post-bake (post-exposure bake) on a hot plate at 70°C for 3 minutes to complete the cross-linking reaction initiated by the exposure and the definition of the structures. The masters were finally immersed in a developer solution (PGMEA) for 10 minutes to dissolve non-exposed photoresist, rinsed in isopropanol and dried with filtered air. A summary of the key photolithography steps followed to fabricate the SU-8 masters is presented in Figure 6.5

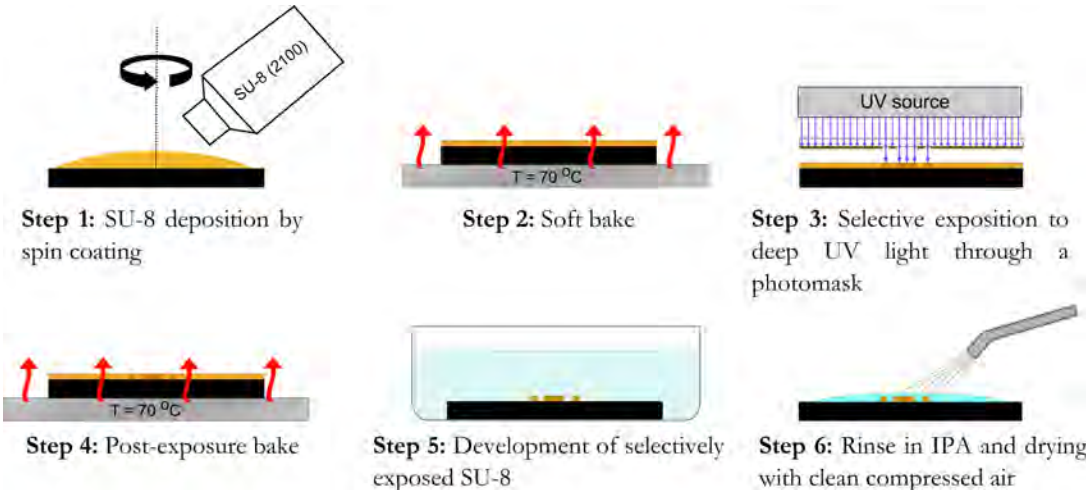

Figure 6.5: Summary of the main photolithography steps from the deposition of the photoresist to the final master

6.2 Replication of the microfluidic master

Once the master has been fabricated, replication by PDMS casting is straightforward, inexpensive and does not require advanced equipment or expertise. Thank to the softness of PDMS, demolding rarely damages the master, leaving it intact for reuse. Replica molding requires three main steps: casting the liquid PDMS prepolymer on the master, thermal curing of PDMS and peel-off. In this project, the microfluidic masters acquired from microLIQUID S.L. were replicated to create the upper and lower layers of the skin-on-a-chip device.

The PDMS kit (Sylgard 184, Dow Corning) was poured into a disposable cup in a 10:1 weight ratio of monomer to curing agent to prepare $\sim 100\,\mathrm{g}$ of PDMS prepolymer. The components were vigorously mixed with a glass stirring bar until the mixture appeared white due to the bubbles formed during mixing (Fig. 6.6a). The prepolymer mixture was then introduced in a vacuum chamber and degassed until all bubbles disappeared (Fig. 6.6c).

After degassing, the prepolymer was slowly poured on the masters –which were previously introduced in a large culture plate– to avoid the formation of additional bubbles. Any bubbles formed during this

process were manually removed with a thin syringe needle (Terumo). The masters for the upper and lower layer were covered to a thickness of ∼6 and ∼ 4 mm respectively and then introduced in an oven at 80 °C for 1 hour to cure the PDMS.

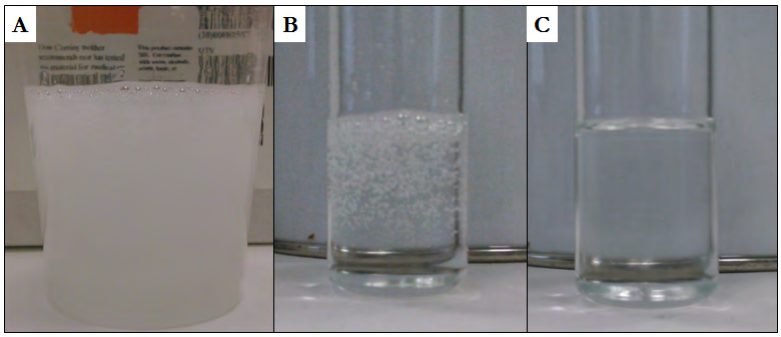

Figure 6.6: PDMS mixing and degassing (A) Appearance of the prepolymer immediately after mixing (B) After it has been partially degassed (C) Once degassing is complete

After curing the PDMS, the masters were extracted from the oven and allowed to cool down to room temperature. A scalpel was used to trace the periphery of the chips without scratching the SU-8 master and the PDMS was carefully peeled off with the help of a small spatula. The PDMS replica was then cut into individual chips with the scalpel, and the input and output ports were perforated using a 1.2 mm diameter blunt mixing needle (no bevel) as punch.

Thorough inspection of the PDMS chips showed that the lateral walls that separate the central chamber from the pneumatic channels were often missing or damaged, and those that remained intact displayed low mechanical stability and were unable to prevent fluid leakage into the pneumatic channels. This is likely caused by the high aspect ratio (1:10) of these walls and the corresponding slit in the SU-8 master.

6.3 Microimprinting for membrane fabrication

Nano- or microimprinting[14] constitute a group of microfabrication methods commonly used to engrave features on the surface of an imprint resist (typically a thermoplastic or elastomer) based on the deformation of the resist by a mold. While the main purpose of microimprinting techniques is the fabrication of elastomer stamps[15] for microcontact printing, they can be adapted to produce through-holes on a thin film of resist.

High accuracy, micrometer-scale pores can be produced in a PDMS membrane using a SU-8 master and microimprinting techniques. In this project, a10 µm thick PDMS membrane with pores imprinted according to the specifications described in Section 4 was developed.

Thin film thickness was characterized with optical techniques based on spectral reflectance (Filmetrics F20-UV). A Cauchy model $\left(n = \frac{A}{\lambda} + \frac{B}{\lambda^2} + \frac{C}{\lambda^4}\right)$ for the index of refraction of PDMS was developed adjusting the coefficients A, B, C to data extracted from [102] with a linear fit (Fig. 6.7a). This optical characterization was subsequently used to parametrize PDMS spin coating on Si (Fig. 6.7b), relating spinning rate to membrane thickness. For this purpose, PDMS was deposited on Si chips by spin coating at different speeds, and the resulting thickness was measured. Additionally, this technique was used to characterize the thickness of a silicone oil film deposited on Si under different conditions (6000 rpm, 3000 rpm and immersion in ethanol followed spin coating at 3000 rpm) and the PDMS membranes deposited over these layers (Fig. 6.8)

To fabricate the porous PDMS membrane, a PDMS (Dow Corning Corporation) support was produced with a flat surface according to the method presented in Section 6.2 but curing the PDMS at 75°C for 1 hour on a hotplate. A layer of silicone oil (3-IN-ONE) was deposited in the form of a spray and subjected to spin coating at 3000 rpm. This method produced a very uneven coverage (Fig. 6.8a) that recovered the form of droplets within 5 minutes. A second layer of PDMS was deposited by spin coating

[14] There is still discussion regarding the nomenclature and classification of different techniques, including hot embossing

[15] Nanoimprinting lithography has been used in the microelectronic industry and in micro/nano fluidics for scales in the order of nanometers

at an initial speed of 3000 rpm for 30sec followed by 6000 rpm for 1 minute, which yielded an uncured PDMS membrane of $\sim 10\,\mu m$ thickness (Fig. 6.8b).

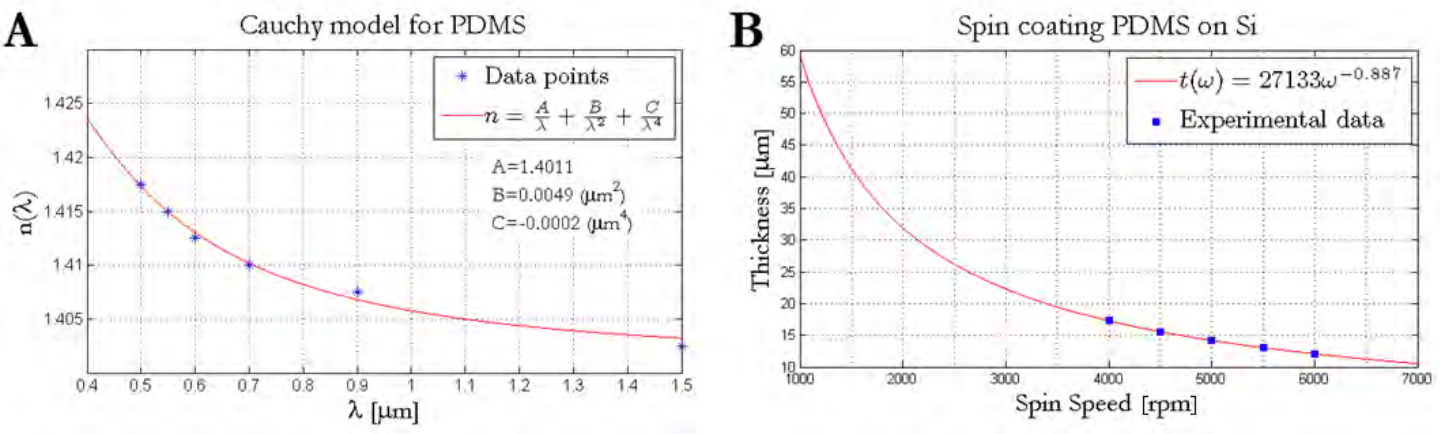

Figure 6.7: Optical characterization of PDMS spin coating thickness (A) Cauchy model of PDMS index of refraction used to characterize thin film thickness by optical methods (B) Relationship between spinning rate and membrane thickness for PDMS on Si

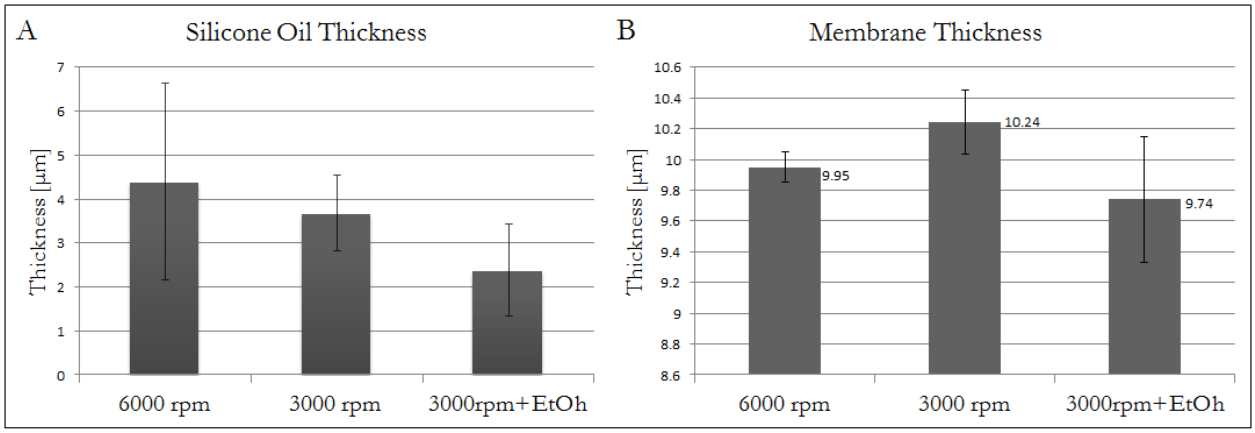

Figure 6.8: Thickness of silicone oil and PDMS deposits used during microimprinting (mean ± standard deviation. (A) Thickness of the silicone oil layer deposited at 6000 rpm and 3000 rpm with and without previous ethanol treatment.The high variability in the data suggest low uniformity (B) Thickness of a PDMS membrane deposited on the previous silicone oil at 6000 rpm.

The SU-8 micropillar array was manually aligned with the support and brought into contact with the uncured PDMS. The construct was placed on a hotplate at 80°C for 1 hour to cure the membrane. Mild pressure was applied during curing to allow feature imprinting without causing PDMS outflow. The master was then peeled-off to obtain a membrane with through-holes with a diameter of 10 µm and a pitch of 40 µm. A summary of the microimprinting protocol is presented in Figure 6.9

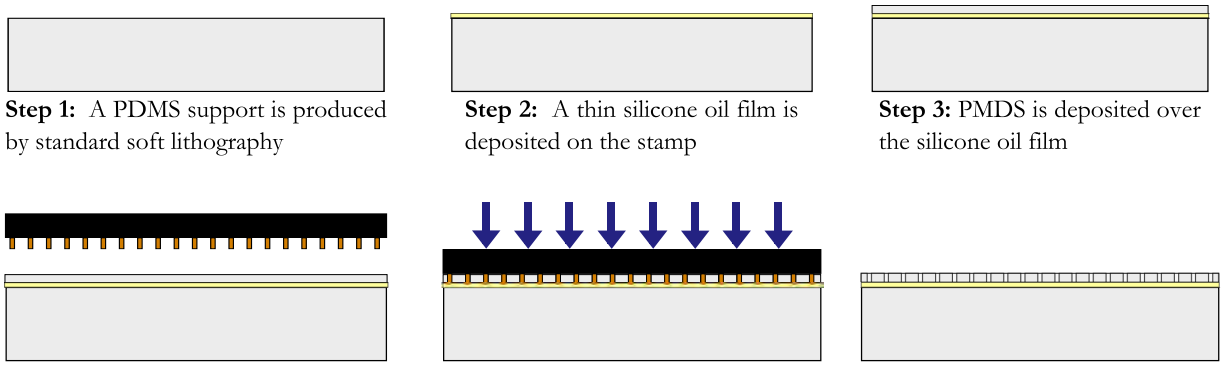

Figure 6.9: Summary of the microimprinting procedure to obtain a PDMS membrane with through-holes from a previously fabricated master

This process resulted in significant adhesion between the membrane and the master due to the poor anti-adherent properties of the silicone oil. Even after spin coating, the oil layer was highly heterogeneous and presented low coverage of the surface, as evidence by the large variability in the data (Fig. 6.8a). As a result, the membrane was ruptured during master detachment and traces of PDMS remained on the master, preventing further use (Fig. 6.10). The use of an anti-adhesion treatment on the surface of the stand and the master could significantly improve the results, maintaining membrane integrity after master lift-off. For instance, surface treatment with Trichloro (1H,1H,2H,2H-perfluorooctyl) silane or PFOCTS is widely used to facilitate demolding in microfluidic technologies [78, 103]

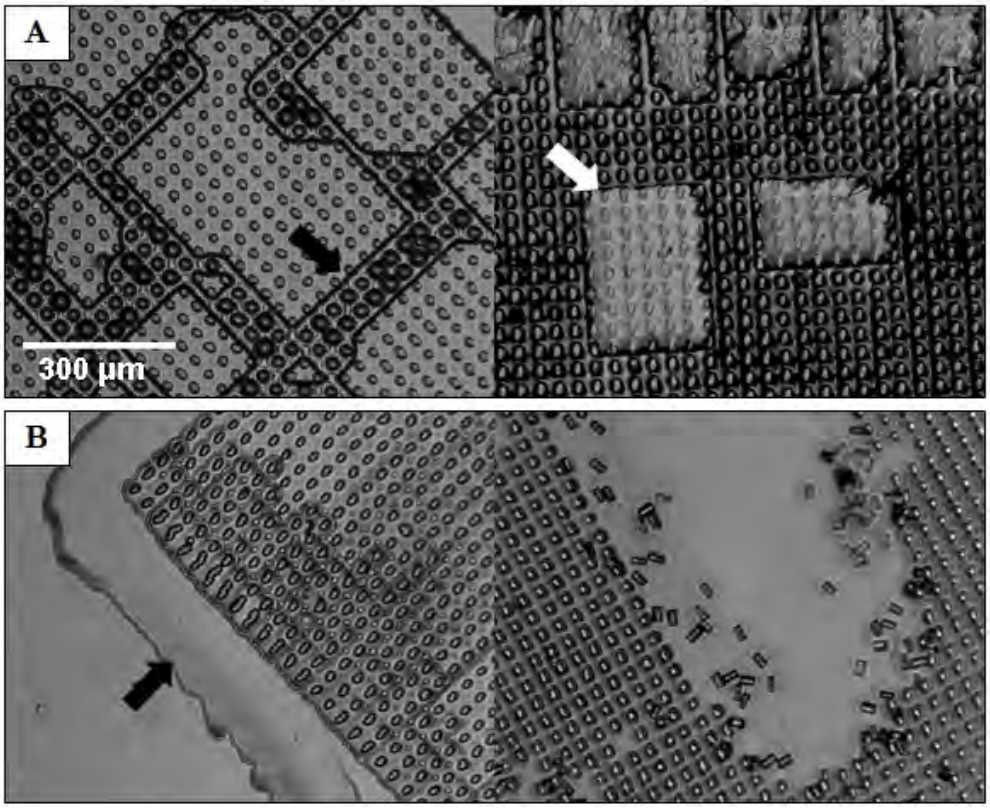

Figure 6.10: Results of the microimprinting process after master lift-off. (A) PDMS membrane with through holes. (B) State of the SU-8 master after detachment. Notice the ruptures of the membrane (black arrows) and the imprint of the micropillar array on the underlying PDMS stand (white arrow)

6.4 Integrated porous membrane

Membranes provide control of mass transport, separation and, immobilization and interfacing. Although membrane science and technology has developed as an independent field, it has become increasingly interesting for the microfluidic field in the last decades [104]. Microfluidic membrane devices have been used for various applications such as filtration, culture support, gas-liquid contact and dialysis, emulsification, BioMEMS sensors or selective adsorption.

Membranes are exceedingly important in organ-on-a-chip applications, as they provide a means for tissue-tissue interfacing. They mediate contact and interaction between cells seeded on either side of

the membrane and regulate the transport of solutes between compartments. Developing biocompatible membranes that can recapitulate the permeability and transport characteristics of specific tissues will prove essential to the fabrication of certain organs on chips, particularly those in which mass transport, separation and filtration of body fluids are fundamental functions. Selecting a membrane with the appropriate properties is therefore key to the device operation and success.

There are several methods to incorporate membranes into microfluidic chips, including bonding of commercial membranes; in-situ fabrication; incorporation of built-in membranes during chip fabrication; and integration of microfabricated membranes. Some of these techniques are remarkably complicated and require complex equipment and advanced expertise; and thus unsuited for organ-on-a-chip application, in which simplicity of fabrication and operation is fundamental for its wide-spreading. Post-fabrication assembly of the membrane is simpler and allows a wider range of readily available membranes to be incorporated.

The skin-on-a-chip device is a dynamic system subjected to a constant fluid flow –and the corresponding shear stress– and cycles of mechanical stretch and recoil; and therefore the membrane cannot be simply clamped or sandwiched between the two PDMS layers. Complete integration of the membrane within the chip and bonding to the remaining components is essential to prevent fluid leakage, to maintain cell types separated and to withstand the physical forces during operation without detachment.

This section explores the mechanical, chemical, biological and transport properties of two different membranes: a microfabricated PDMS porous membrane and a commercial polycarbonate (PC) membrane. Finally, it presents a detailed comparison between the two membranes and basic guidelines for membrane selection.

6.4.1 Polydimethylsiloxane membrane

PDMS have been widely used as membrane material due to its high gas permeability and its elasticity, especially in gas-related applications. PDMS allows transport of gaseous species, can be inexpensively fabricated in very thin films (down to 7 µm [105]), and it can be easily integrated in microfluidic devices. In cell culture applications, it provides a solid but flexible support and it is permeable to CO_2 and O_2.

The main disadvantages of PDMS as membrane material are its low mechanical strength –very thin films rupture easily–, handling difficulties –PDMS membranes tend to fold– and the high hydrophobicity of its surface. The hydrophobicity is a particular cause of concern in cell culture applications, as it impairs cell attachment to the surface of the material (Fig. 6.11). Different methods can be used to promote cell attachment to the surface [106], such as rendering it hydrophilic with plasma treatment [107] or functionalizing the surface with ECM or adhesive proteins [108].

In the present work, the effect of a collagen surface treatment on cell attachment to PDMS was studied. A PDMS thin film was functionalized with collagen by physisorption and a subconfluent number of cells were seeded on treated and untreated PDMS to investigate the differences in cell adhesion.

PDMS membranes without pores were fabricated by spin coating as previously described in Section 6.3. The small membranes were carefully peeled off of the Si substrate after curing and placed on a cell culture plate, leaving a significant portion of the plate surface uncovered to serve as control. The surface was then treated with 1 ml of a 20 µg/ml solution of collagen (Sigma Aldrich) in PBS (Sigma Aldrich) for 2 hours under UV light; after which the collagen solution was removed and the surface, rinsed in PBS and allowed to dry for another hour under UV light. The treated samples were stored at 4 °C until further use. Untreated PDMS samples were prepared the same way without the collagen treatment.

To study cell attachment, $5 \cdot 10^5$ human fibroblast were seeded on either treated or untreated PDMS and cultured for 48 hours with Dulbecco's modified eagle's medium (DMEM High W/Glutamax, Gibco) with 10% FBS (Fisher Scientific) and 2.5% Antibiotic/Antimicotic (Atb/Atm, Fisher Scientific) in an incubator at 37 °C and 5% CO_2. Photographs (Olympus SC30) were taken after 1 hour and 4 hours to characterize early adhesion to the surface. After 48 hours, the cultures were rinsed twice in PBS to remove loosely attached cells and photographs were taken again. Multiple membranes fabricated independently were tested to consider sample variability.

Results of the cell adhesion study (Fig. 6.11) indicate that the surface properties of untreated (bare) PDMS prevent cell adhesion. Even after 48 hours, the number of cells attached to the PDMS membranes remained minimal, and they acquired abnormal morphologies. The presence of PDMS membranes,

however, did not hinder normal cell attachment and proliferation on the uncovered surface of the culture plate, which demonstrate its biocompatibility.

On the other hand, PDMS membranes treated with collagen exhibited high cell adhesion and cell density after 48 hours (Fig. 6.11), which illustrates the effectiveness of collagen physisorption as a PDMS biofunctionalization technique. The cell culture reached confluency on both the plate and the PDMS membranes; and surface modification effectively allowed cell adhesion even after 48 hours, as evidenced by the fact that cell attachment to the functionalized membranes persisted after PBS rinsing.

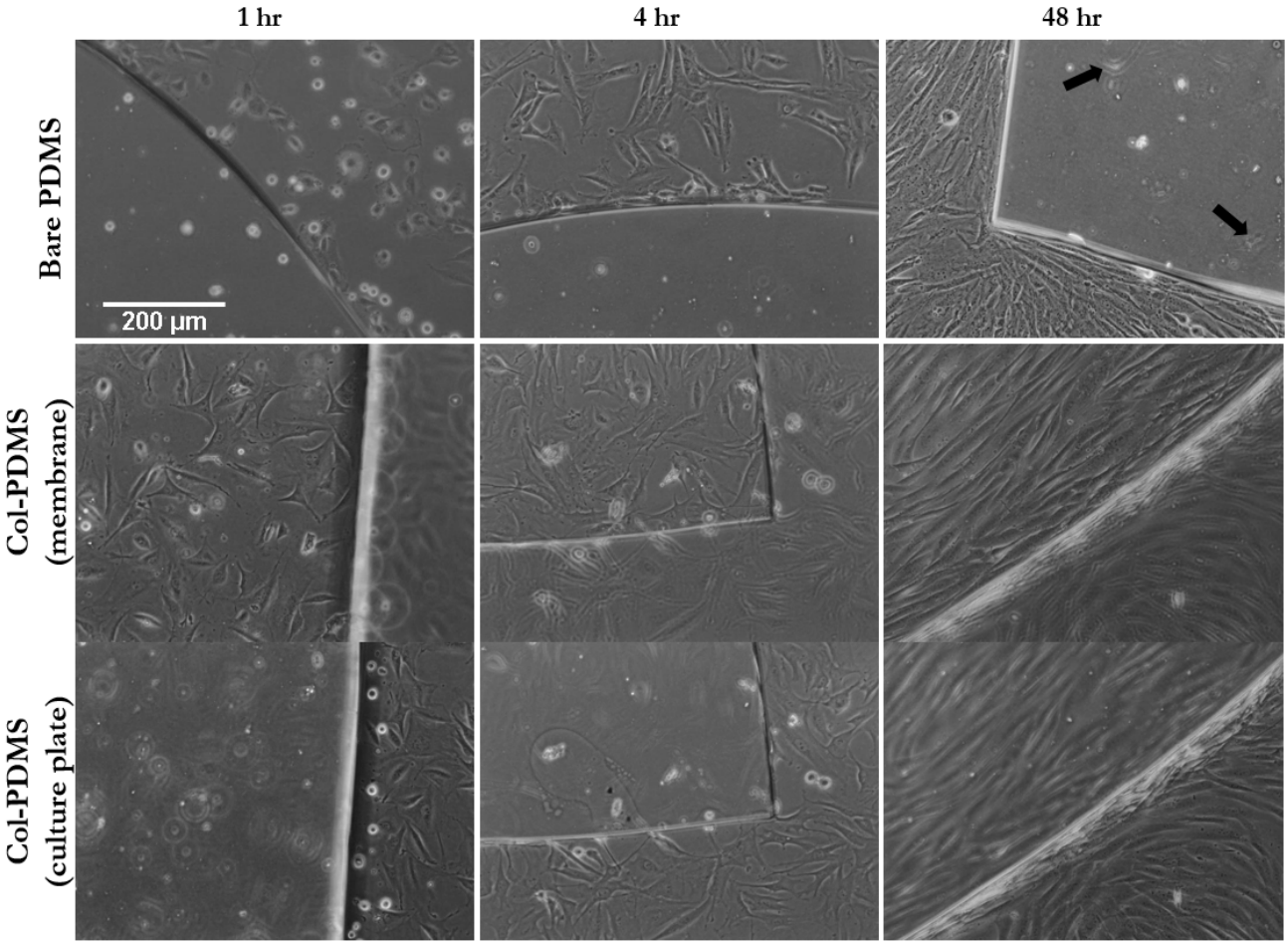

Figure 6.11: Cell adhesion to bare (top) and collagen-treated (middle and bottom) PDMS membranes at 1 hour, 4 hours and 48 hours. For functionalized membranes, images focus on the membrane (middle) and the culture plate (bottom). High hydrophobicity of bare PDMS impairs cell attachment, and only few cells with abnormal morphology can be seen (black arrows).

Although PDMS has high gas permeability, the skin-on-a-chip application requires the use of a porous membrane which allows fluid transport across. Pores can be incorporated in a PDMS membrane during fabrication in the form of through-holes, as described in Section 6.3. The advantage of using microfabrication technologies is the control over pore size and distribution. PDMS membrane pore size, geometry, arrangement and density can be selected according to the transport requirements of different organ on chip applications.

6.4.2 Polycarbonate membrane

Polycarbonate (PC) membranes are widely used in life sciences due to their versatility, simplicity and availability. In fact, nuclear track-etched PC membranes have been commercially available since the 70s [109] and they have been used for a variety of applications, including filtration, purification, analysis, sample preparation, cell culture or chemotaxis among others. PC membrane versatility has led to their use in hybrid microfluidic devices for cell culture and characterization [110] and lab-on-a-chip applications [111].

Porous PC filters are produced using nuclear track-etching technology, in which a thin film of PC is bombarded with heavy ions from an accelerator or a nuclear reactor. As they pass through the material, they cause radiolysis, leaving sensitized tracks that are susceptible to chemical etching to produce the pores. Nuclear track-etching allows precise and independent control of pore size and density, with narrow pore size distribution and low pore shape variability.

Some membrane filters are treated with wetting agent to increase the wettability, facilitating water transport across the pores. Grafting or adsorption of polyvinylpyrrolidone (PVP) is commonly used in commercial membranes to increase their hydrophilicity. PVP is considered biocompatible and is used in many medical applications.

Commercial PC membranes are easy to handle and manipulate, and they are available in a range of diameters and pore sizes. They provides higher mechanical stability and support for cell culture, making them excellent candidates for the skin-on-a-chip device. In the present work, isopore track-etched PC membranes with 5 μm pore size, 7-22 μm thickness and 25 mm diameter acquired from Millipore were studied for their application in organ-on-a-chip devices.

To study cell adhesion to PC and the effectiveness of collagen physisorption, PC filters were placed on a cell culture plate and treated with a 20 µg/ml collagen solution as previously described. Then, following the protocol presented in the previously section, $5 \cdot 10^5$ human fibroblasts were seeded on collagen-treated and bare PC membranes. Likewise, the same number of cells was seeded on a conventional cell culture plate to be used as adhesion and proliferation control. Photographs were taken at 24 and 48 hours to characterize cell adhesion and proliferation on PC with respected to the control. Additionally, at 48 hours the membranes were carefully extracted with tweezers from the culture plates and placed in a new one to ensure that cells were seeded on the membrane. The experiments were performed in triplicate.

The results obtained for the experiment (Fig. 6.12) indicate that polycarbonate membranes do not substantially impair cell adhesion and proliferation. Cells seeded on both bare or treated PC were capable of adhering to the surface, and no notable differences between treated and untreated membranes were observed. This suggests that the collagen treatment does not provide a significant improvement in cell adhesion over bare PC.

Cell adhesion and proliferation have been reported to decrease with increasing pore size [112] because the pores on the surface represent an obstacle for adhesion. Although in the present case cells seeded on polycarbonate membrane did not exhibit noteworthy differences in the degree of adhesion and confluency with respect to the control, this phenomenon could become a cause of concern in organ-on-a-chip applications that require higher permeability and thus larger pore size.

Polycarbonate membranes are therefore easier to acquire, given that they are commercially available, and simpler to use; as evidenced by the fact that no surface treatment is required for cell adhesion

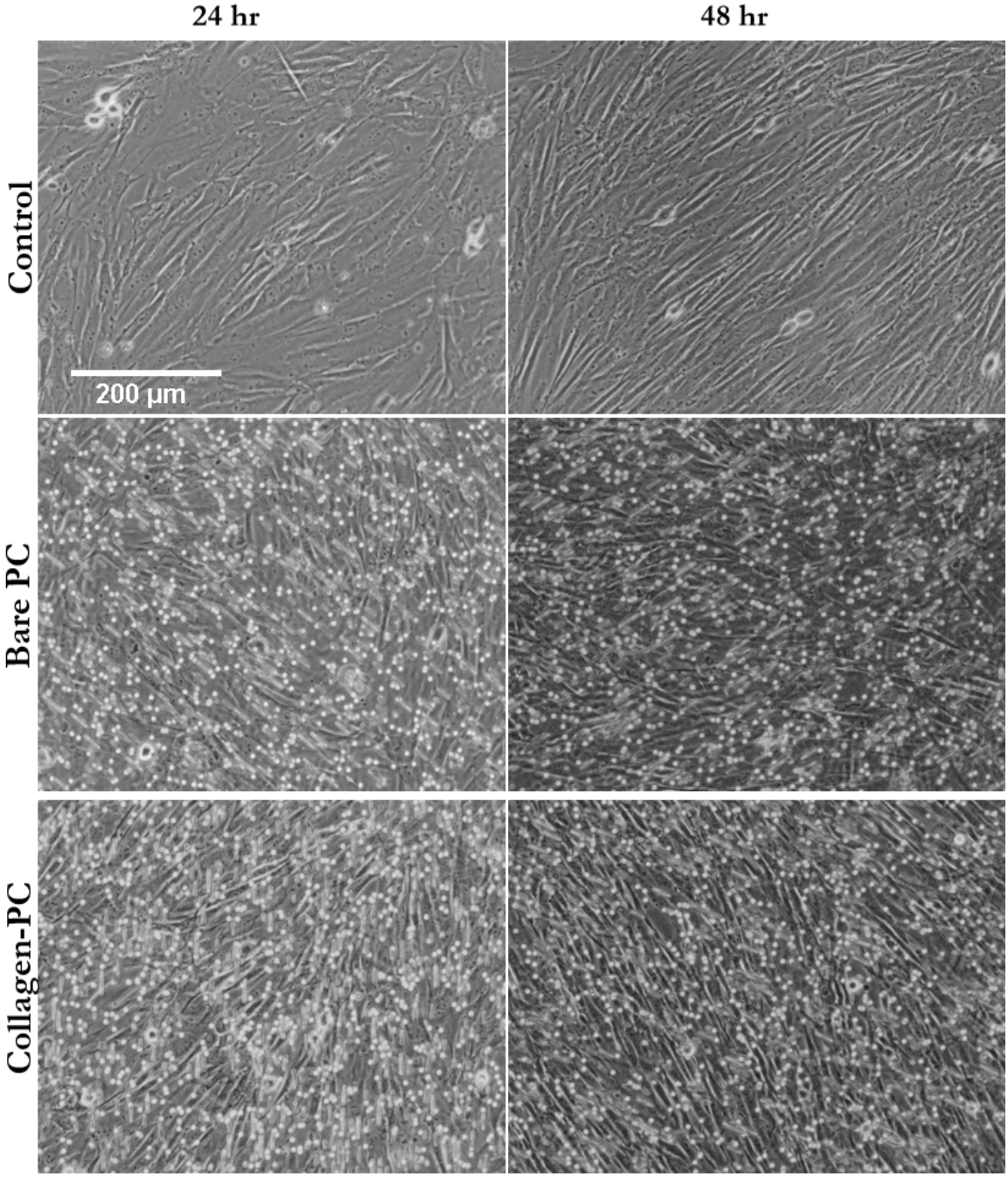

Figure 6.12: Results of the cell adhesion study on polycarbonate. Both bare and treated PC filters exhibit high cell adhesion and no significant differences with the control.

6.4.3 Membrane selection

This section provides a detailed comparison between the two membranes explores in this project: a microfabricated PDMS membrane and a commercial PC filter. Given the importance of biological, mechanical, and chemical properties as well as its availability for organ-on-a-chip application, the comparison presented herein focuses on these aspects of the two membranes.

From a biological point of view, the hydrophobicity of PDMS severely hinders cell attachment to the membrane without surface treatment. A simple strategy to mask the chemical nature of the elastomer is the physical absorption of proteins to the surface. Physisorption of ECM components (collagen) or adhesive proteins (fibronectin) significantly improves cell attachment to the PDMS membrane even after 48 hours. However, the long-term stability of this protein surface coating can be compromised due to thermal elution and the Vroman effect.

On the other hand the PC membranes with a PVP wetting agent display high cell attachment to the surface even prior to any surface treatment; which reduces the complexity and fabrication time of the device. Moreover the high pore density of these membranes seems to have no major effect over cell attachment and growth, at least at small pore sizes. However, the presence of pores on the membrane interferes with cell observation by conventional microscopy, impairing optical characterization of the device operation.

Mechanically, the PDMS membrane displays a hyperelastic behavior, thus making it the ideal candidate for applications that require reversible membrane deformation upon mechanical loading. Polycarbonate membranes, due to its mechanical stiffness, is not well suited for devices that require high membrane deformability.

PC is an organic polymer with multiple organofunctional groups that are susceptible to chemical reactions with biomolecules present in the culture, which could cause membrane degradation and liberate toxic byproducts. Even though this reactivity is overall a disadvantage, it can also be exploited to biofunctionalized the membrane. On the other hand, PDMS is chemically inert and highly

biocompatible due to its inorganic backbone; although it can be activated and derivatized by oxygen plasma treatment.

Production of PDMS membranes is inexpensive, but the fabrication of the previous microimprinting master requires expensive equipment and certain expertise. In exchange, the pore size, distribution and geometry can be fully controlled and tailored to the specific application. Polycarbonate membranes are readily available from various distributor for a moderate prize and they can readily be used without specific expertise. As a tradeoff, PC membranes are less customizable than PDMS membranes, and only certain pore sizes and densities are available.

The comparison between the two types of membranes studied in the present work is summarized in table 1

Table 1: Summary of the comparison between membranes

Characteristic	**Microfabricated PDMS**	**PC + PVP wetting agent**
Biocompatiblity	The polymer is biologically inert	PC is bioinert and PVP is widely used in medical applications
Cell visualization	Fully transparent, easy to see through	Transparent, but pores impair the visualization
Cell attachment	Requires surface modification via physisorption	High attachment even without treatment
Cell growth	Unaffected if surface-treated	Mostly unaffected (lower alignment in confluent cultures)
Integration on the device	Simple: plasma treatment	Complex: requires additional chemical modifications
Pore size	Defined by the SU-8 master	Defined by the manufacturer's fabrication process
Pore size distribution	Almost monodisperse	Very narrow
Pore size limitations	Lower bound, depends on equipment	Upper bound (max 12μm)
Pore geometry	Defined by the SU-8 master	Circular
Pore edge resolution	Dependent on equipment quality	Very good
Thickness	Determined by spin coating	Variable (7-22 μm)
Availability	Requires microfabrication capabilities	Commercially available
Elasticity	Hyperelastic ($\sim$ MPa)	Relatively stiff ($\sim$ GPa)
Modification	Difficult to manipulate due to softness	Can be easily perforated and cut
Handling	Tends to fold and stick to other surfaces	Easy to handle, non adherent
Price	Inexpensive	Moderate (˜1.5 € per membrane), depends on distributor

For this skin-on-a-chip device, a commercial polycarbonate membrane was selected due to its availability, cell adhesion properties and simplicity of use. In this application the membrane is not directly stretched, therefore an elastic PDMS membrane is not a requirement; and a PC membrane ensures long term tissue stability without surface treatment.

6.5 Integration and bonding of the device

Integration of the different components is a central part of the device fabrication. The use of biological materials limits the range of bonding materials that can be used, since many adhesive are cytotoxic. Moreover, biological materials tend to be highly susceptible to plasma bonding techniques commonly used in microfluidics, hence the device must be fully assembled before seeding.

PDMS-PDMS bonding by oxygen plasma treatment is well established in the field of microfluidics, although other techniques have been explored [113]. Bonding of certain thermoplastics using different techniques has also been studied [114,115], specially PMMA due to its interest in microfluidics. Bonding of hybrid chips –devices with components fabricated in several different materials– is more challenging due to differences in properties and surface chemistry between the materials.

In order to achieve thermoplastic-PDMS bonding, different methods have been developed based on the used of silane coupling agents [116,117]. Silanization is one of the most common polymer surface treatment techniques in microfabrication. It is based on the formation of a self-assembled monolayer (SAM) or a thin cross-linked network of a silane coupling agent which contains a Si atom, three hydrolyzable groups, an alkane linker and a terminal organofunctional group. The polymer surface is usually activated by oxygen plasma treatment prior to the silanization, facilitating the reaction with the silane agent.

APTES or 3-Aminopropyltriethoxysilane is one of the most popular silane agents. It contains three ethoxy hydrolyzable and cross-linkable groups and a terminal primary amine that can react with most functional groups in organic chemistry (Fig. 6.14a). APTES has been shown to react with polycarbonate without oxygen plasma treatment, and a new mechanism of interaction has been postulated to explain this effect [118].

Therefore, two main mechanisms have been proposed for the silanization of PC with APTES (Fig. 6.13). The silanol groups formed after hydrolysis can react with hydroxyl groups on the surface of PC after plasma activation, while remaining silanol groups undergo a condensation reaction to cross-link adjacent APTES molecules (Fig. 6.13a). This mechanism is common for all silanization treatments.

On the other hand, the second mechanism is based on the susceptibility of the carbonate groups to selective chain scission by the primary amine, resulting in the direct covalent bond of APTES to the polymer chain without the need of oxygen treatment (Fig. 6.13b). In this case, one of the silanol groups resulting from hydrolysis behaves as terminal group, while the other two are involved in cross-linking.

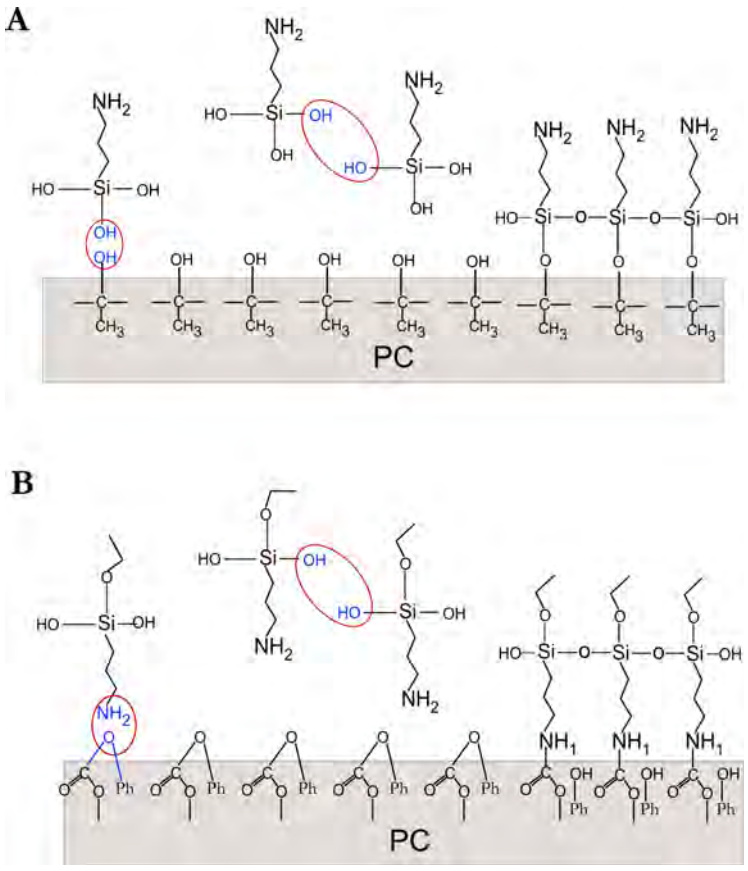

Figure 6.13: Two proposed methods for polycarbonate silanization with 3'-aminopropyltrietoxisilane (APTES). (A) Characteristic silanization mechanism in which hydrolyzable groups react with the plasma activated surface. (B) Alternative chain scission mechanism based on aminolysis of the carbonate group.

These mechanisms can be explained from the molecular structure of polycarbonate (Fig. 6.14b). The presence of methyl groups, which can be easily oxidized by plasma treatment, provides binding points for the hydrolyzable groups in accordance with the first mechanism. Moreover, the carbonate ester group (–OCOO–) is a target for aminolysis caused by the terminal amine of APTES. This reaction

mechanism results in the cleavage of the polymer chain, with one end terminated at a phenol group and the other covalently linked to the APTES molecule by a carbamate or urethane bond (–NHCOO–).

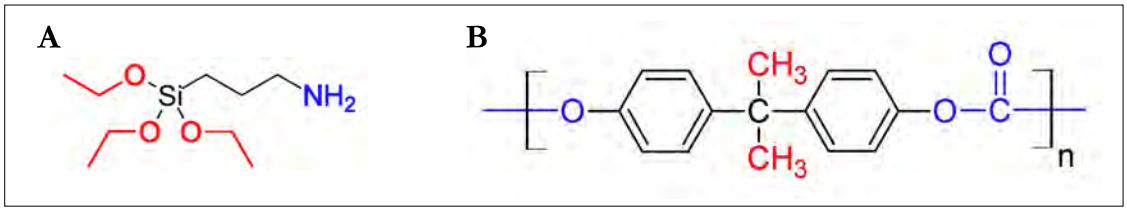

Figure 6.14: Structure of key molecules in PC surface treatment. (A) 3-Aminopropyltriethoxysilane. Red color represents hydolyzable groups, blue color represent the terminal group. (B) Polycarbonate polymer backbone. Red groups are susceptible to plasma oxidation, blue groups are susceptible to aminolysis.

Based on a previously reported thermoplastic-PDMS bonding method [119] and well-established silanization techniques [120], a novel PC-PDMS bonding strategy was developed to integrate the different components of the skin-on-a-chip device.

The polycarbonate membranes (Millipore) were rinsed in isopropanol (IPA), held in a stand and treated with room air plasma (Expanded Plasma Cleaner, Harrick Plasma) at 30 W and ˜310 mTorr for 90 seconds. A 1.5% (v/v) aqueous solution of 3'-aminopropyltrietoxisilane (APTES) (99%, Sigma Aldrich) was prepared 30 minutes beforehand to allow hydrolysis, and the pH was adjusted to 5 using acetic acid. After the plasma treatment, the membranes were quickly immersed in the silanization solution for 20 minutes. The membranes were then extracted and placed in an over at 110 °C for 30 minutes to cross-link the silane layer.

After the silanization, the membranes were rinsed in DI water and placed on the stand again. The PDMS chips were cleaned with adhesive tape to remove the dust particles in order to ensure good contact between the surfaces. Then the PDMS components and the functionalized membranes were simultaneously treated with room air plasma at 30W for 90 seconds, after which they were manually aligned and brought into contact. Mild pressure was applied for 5 minutes to facilitate the bonding without disturbing the PDMS features. A summary of the bonding protocol and the events at the molecular level is presented in Figure 6.15.

To complete the chip assembly, the corners were chamfered at $\sim 45^{o}$ to prevent debonding due to adhesion problems at the corners and the chips were stored at room temperature until further use.

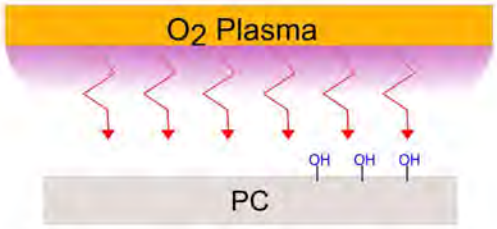

Step 1: Activated of the PC surface by oxygen plasma treatment

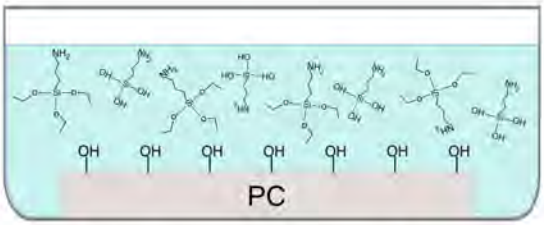

Step 2: Silanization of activated PC surface with APTES from aqueous solution

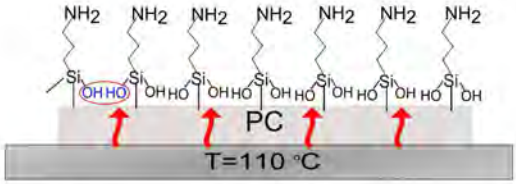

Step 3: Thermal curing of the silane layer to promote crosslinking

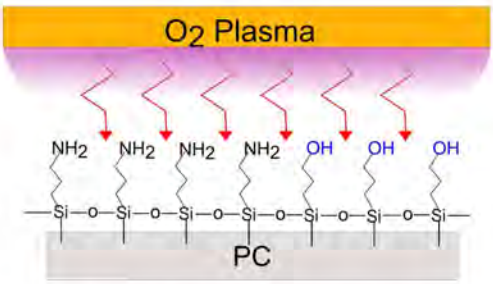

Step 4: Activation of the terminal groups on silanized PC surface by oxygen plasma teratment

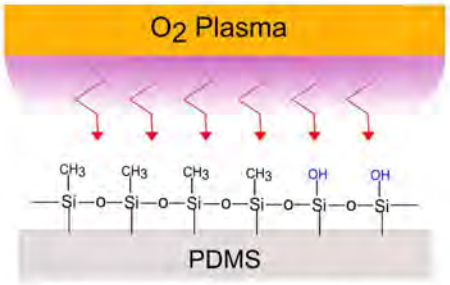

Step 5: Activation of the PDMS surface by oxygen plasma treatment

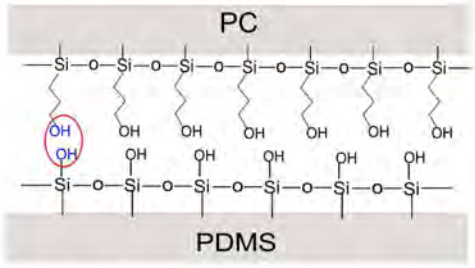

Step 6: The activated PDMS and the silanized PC surfaces are brought into contact

Figure 6.15: Summary of the PC-PDMS bonding protocol. Blue functional groups represent reacting groups

7 Skin-on-a-chip seeding and operation

Once the device has been fully assembled and prepared for application, it must be sterilized and connected to a microfluidic circuit. The nature and properties of the different surfaces of the device fundamentally influences the sterilization and filling process (Fig. 7.1). The membrane silanization is irreversible, which combined with the PVP wetting treatment, makes the membrane hydrophilic. On the other hand, the plasma activation of the PDMS surface is transient and it recovers its hydrophobicity after a few minutes.

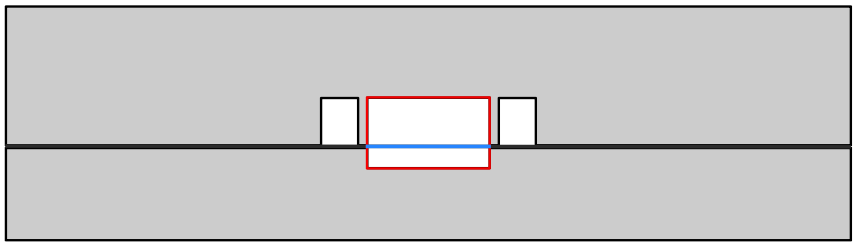

Figure 7.1: Surface properties of the device after treatment and assembly. The hydrophilic membrane (blue) allows cell adhesion and fluid transport. The hydrophobicity of PDMS walls (red) prevents cell adhesion on the sides of the chamber.

Microfluidic tubing, accessories and pumps are commercially available from a number of manufacturers and can be readily connected to create a circuit. Perfusion pumps use a high-precision mechanical system to drive the piston of a syringe at a very slow pace, generating extremely small flow rates (down to picoliter/minute). Specialized microfluidics pumps are designed to provide short settling times and to counteract the flow pulsatility due to the motor steps, providing very steady flow rates that are required for microfluidic cell culture applications. These perfusion pumps, however, are bulky and extremely expensive, limiting the access to microfluidic research.

The final step in the fabrication of the skin-on-a-chip is the *in situ* construction of a bioengineered skin equivalent inside the device. Skin tissue engineering is a well established field, and skin equivalents can be fabricated in a number of materials and with common techniques that can be adapted to the requirements of microfluidic systems.

7.1 Wet and dry sterilization

Microfabrication of the skin-on-a-chip device is carried out under non-sterile conditions, and therefore the device must be sterilized prior to cell seeding. Two main groups of strategies can be used to sterilize microfluidic devices, referred to as wet and dry methods in the present work. Wet methods make us of some disinfectant in liquid form such as ethanol or isopropanol that can be easily flowed through the channels. Dry methods do not used wet chemicals. Instead, they rely on gases, radiation or heat to sterilize the surface.

Wet methods are widely used in microfluidics because they serve two purposes: first, they disinfect the channels, eliminating ay microorganism that may interfere with the tissue culture; and second, they can be used to simultaneously prime the channels.

As previously explained in Section 6, the hydrophobicity of PDMS can severely hinder channel filling with aqueous fluids. The plasma treatment commonly used to assembly the device can render the PDMS surface hydrophilic, but this effect is only temporary. For this reason, some authors recommend pre-filling (priming) the channels with some liquid immediately after assembly with oxygen plasma to extend the change in surface chemistry, to minimize bubble nucleation and to facilitate subsequent filling with the fluid used in the device operation.

Dry methods allow for parallel or mass sterilization and can be controlled to a larger extent than wet methods. Moreover, they do not leave chemical residue in the channels nor do they adsorb to channel walls. On the other hand, radiative and thermal treatments can alter the chemistry of the materials, having a harmful effect on the device.

UV treatment has been reported to cause some transient changes in the chemistry of PDMS, but mechanical properties, wettability, surface microtexture and element concentration remain mostly unaltered [121, 122]. Moreover, gamma radiation is proposed by the PC manufacturer (Millipore) as sterilization methods.

The skin-on-a-chip device represents a peculiar case for two reasons: (a) priming of the channels

immediately after plasma treatment is not possible, and (b) wetting the channels in the wrong order can cause difficulties during cell seeding.

The first problem is caused by the complex bonding protocol that requires some surfaces contact time under mild pressure before the device can be used. By the time the chip is ready to be filled, the PDMS channel walls have reverted to their hydrophobic state, preventing channel priming. One of the main advantages of wet methods plays no role in this instance for this reason. The second problem arises when the lower channel is wetted in the first place. The ethanol that remains on the walls of the lower channel and the high wettability of the PVP coated membrane favour the leakage of fluid from the hydrophobic upper channel to the lower one, hindering upper channel seeding.

For these reasons, dry methods are better suited for the skin-on-a-chip device. In the present work, the chips were sterilized with UV light (Telstar) for 20 minutes immediately before use.

7.2 Microfluidic circuit and operation

To operate the skin-on-a-chip, a simple microfluidic circuit was developed. A syringe pump was built by re-purposing a low-cost, 3D-printed injection system developed for a previous project. The original prototype featured a linear actuator system composed of a NEMA 17 stepper motor, a M4x0.75 threaded rod, two smooth rods and linear bearings. The original motor was replaced by a low-power NEMA-17 Bipolar Stepper motor with 200 steps/rev (12V 350 mA, Adafruit); which was controlled by an Arduino Uno (ATmega328P). A simple circuit (Fig. 7.2a) was designed to connect the stepper motor to the microcontroller; and a switch with a pull-down resistor was added to turn the pumping action on and off.

The perfusion pump was used to drive a 5 ml syringe (Terumo) which was connected to the microfluidic circuit (Fig. 7.2b). The microfluidic circuit was constructed with 1/16" OD x 0.02" ID and 1/16" OD x 0.03" ID PFA tubing (IDEX); and the connection was accomplished with a 1/4-28 Flangeless Male Nut, a 1/4-28 Flangeless Ferrule for 1/16" OD tubing, and a 1/4-28 Female-to-Female Luer Adapter (IDEX). The inlet of the device was connected to a PFA tube of $\sim 10\,\text{cm}$ length and the outlet to a short, bent PFA tube of $\sim 1.8\,\text{cm}$ length to dispose of the waste.

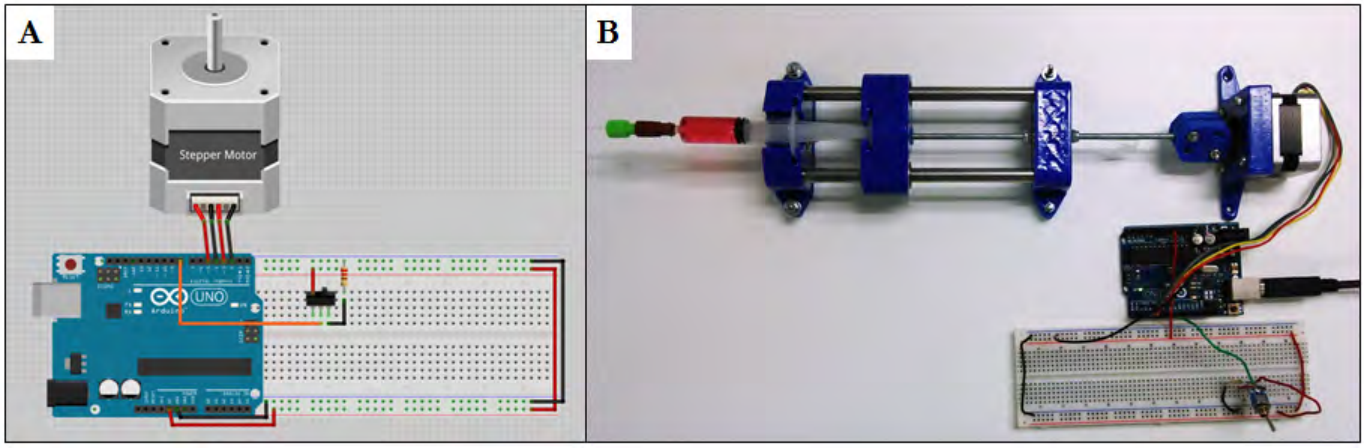

Figure 7.2: Microfluidic circuit and pump. (A) Electronic circuit to control the pump stepper motor. (B) Syringe pump and fluid connection during operation

The pump was programmed with a short Arduino Sketch based on the AccelStepper library (Fig.7.3). The code essentially defines a constant speed and checks the status of the switch. If the switch is ON, then the motor is driven at the chosen speed (4 steps/sec in this case).

PUMP

```
#include <AccelStepper.h> // Load the library
AccelStepper stepper; // Defaults to AccelStepper::FULL4WIRE (4 pins) on 2, 3, 4, 5
int switchPin=8; //Connect the switch to pin 8 on the Arduino board

void setup()
{
  pinMode(switchPin,INPUT);
   stepper.setMaxSpeed(1000);
   stepper.setSpeed(4);  //Speed in steps/sec of the motor
}

void loop()
{
  while(digitalRead(switchPin)==LOW){} //Check the status of the switch
  stepper.runSpeed(); //Run the motor at the selected speed
}
```

Figure 7.3: Arduino program for the pump

The flow rate developed by the pump depends on the selected speed, the dimensions of the mechanical

components and the syringe used. The flow rate generated by the pump can be estimated as:

$$Q = \frac{v \cdot p \cdot A}{s} \tag{53}$$

where v is the speed set by the microcontroller in steps/sec, s is the number of steps per revolution, p is the pitch of the lead screw and A is the cross-section of the syringe. In this case, the program runs the motor at 4 steps/sec; the motor has 200 steps/rev; the pitch of the lead screw is 0.75 mm; and the cross section of the syringe is given by its diameter, $D \simeq 1.27\,\text{cm} \rightarrow A \simeq 127\,\text{mm}^2$. These conditions give an estimated flow rate of $1.9 \cdot 10^{-9}\,\text{m}^3/\text{s}$. Thus, this pump is unable to provide the flow rate ($\sim 1\,\text{ml/hr} = 2.8 \cdot 10^{-10}\,\text{m}^3/\text{s}$) that has been considered in the design.

Based on the dimensions of the channel, the properties of the fluid and the flow rate, the Reynolds number and entrance length and hydrodynamic resistance of the channel can be estimated[16] as:

$$Re = \frac{2\rho Q}{\mu(h+w)} \tag{54}$$

$$Le = 0.06 Re \frac{2hw}{(h+w)} \tag{55}$$

$$R = \frac{12\mu L}{wh^3}\left(\frac{1}{1-0.63h/w}\right) \tag{56}$$

for a channel with a high aspect ratio[17] $w > h$

The microfluidic system of the skin-on-a-chip device is designed to operate at a flow rate of approximately 1 ml/hr, that is $Q = 2.8 \cdot 10^{-10}$ m^3/s. With such a flow rate, the Reynolds number and entrance length are: $Re \simeq 0.1$ and $Le \simeq 2$ µm. Therefore, under these flow conditions, the Reynolds number is sufficiently low to neglect inertial forces and the entrance length represents only 0.015% of the total channel length.

[16] These expressions are based on the unidirectional flow along a rectangular channel and thus they do not take into account the transverse velocity due to the porous wall

[17] The expression for the hydrodynamic resistance is: $R = \frac{12\mu L}{wh^3}\left(1 - \frac{192h}{\pi^5 w}\sum_{n=1,3,5}\frac{1}{n^5}\tanh\left(\frac{n\pi w}{2h}\right)\right)^{-1}$ but it can be simplified when $w > h$ since the term for n=3 is already negligible

The pressure at different points of the microfluidic circuit can be estimates from an electrical analogy based on the hydraulic resistances (Fig. (7.4)). The resistance of the channel is approximately given by equation (56). Moreover, the outlet can be modeled as series of a channel of rectangular cross section 200 x 800 μm and 2.5 mm length, a circular channel of 1.2 mm in diameter and ∼6 mm in length and a thin tube of 0.762 mm in diameter and ∼ 1.8 cmin length. The resistance of the rectangular part can be estimated from eq. (54), whereas the resistance of the cylindrical sections with radii r can be computed as:

$$R = \frac{8\mu L}{\pi r^4} \tag{57}$$

Taking into account the relationship between pressure, flow rate and hydraulic resistance $\Delta P = Q \cdot R$, the pressure drops across the channel and the outlet can be readily know:

$$\begin{aligned} Rc &\simeq 3.3 \cdot 10^{10}\ \text{Pa} \cdot \text{m}^{-3} \cdot \text{s} \quad \rightarrow \quad \Delta P_c = 10\ \text{Pa} \\ Ro &\simeq 8.9 \cdot 10^{9}\ \text{Pa} \cdot m^{-3} \cdot \text{s} \quad \rightarrow \quad \Delta P_{out} = 2.5\ \text{Pa} \end{aligned} \tag{58}$$

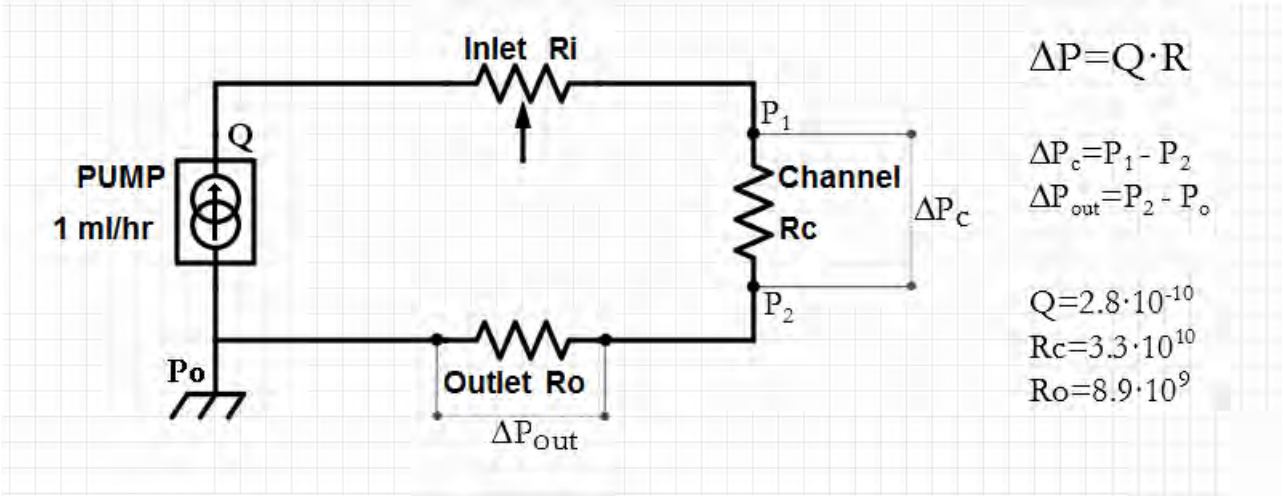

Figure 7.4: Schematics of the microfluidic circuit analog. *Rc*, *Ri* ad *Ro* represent the hydraulic resistances of the channel, the inlet and outlet respectively. The pump is modeled as a current source with constant flow rate Q and the ground pressure is P_o

If the outlet is left open to the atmosphere, the *ground* pressure is equal to the atmospheric pressure. By working with manometric pressures, the *manometric ground* pressure can be set to $P_o = 0$. Under

this configuration of the microfluidic circuit, the pressures at the inlet and outlet of the channel are $P_1 = 12.5$ Pa and $P_2 = 2.5$ Pa respectively.

The custom built syringe pump was unable to deliver such a small flow rate with high precision and steadiness. In fact, it was only able to deliver flow rates in the order of $10^{-9}\,\mathrm{m}^3/\mathrm{s}$ with high pulsatility. Therefore a more sophisticated perfusion pump is required to properly operate the skin-on-a-chip device.

7.3 Cell seeding and *in situ* formation of a skin equivalent

The upper chamber of the skin-on-a-chip device is designed to host a bioengineered skin equivalent perfused by the lower microvascular channel. To examine the effectiveness of the upper chamber as cell culture system two different assays were carried out. In a first instance, a cell seeding experiment was conducted with two different cell types, representative of skin cells: Human Primary Fibroblasts and HaCaT cells (an immortalized keratinocyte cell line). In a second instance, a gelation study was performed by introducing a fibrin matrix into the chamber.

To study the capacity of the device to host a simple cell culture, freshly thawed Human Fibroblasts and HaCaT cells were resuspended in cell culture medium (DMEM+10%FBS, 2.5% Atb/Atm) and seeded into the chamber at a concentration of $\sim 2 \cdot 10^6$ cells/ml and $\sim 6 \cdot 10^6$ cells/ml, respectively. An approximate volume of 10 µl was enough to fill the chamber, resulting in ~ 20000 and ~ 60000 cells being seeded, respectively. Cells were allowed to adhere to the PC membrane for 1 hour inside an incubator at 37 ºC and 5% CO_2. After this time, the lower channel was filled with culture medium and cultured for 24 hours inside the incubator. After 24 hours, the upper chamber was rinsed with fresh medium to discard dead cells and the lower channel was refilled. Phase contrast photographs (Olympus, SC30) were taken at 24 hours to characterize cell adhesion. Experiments were conducted in triplicate for each cell type.

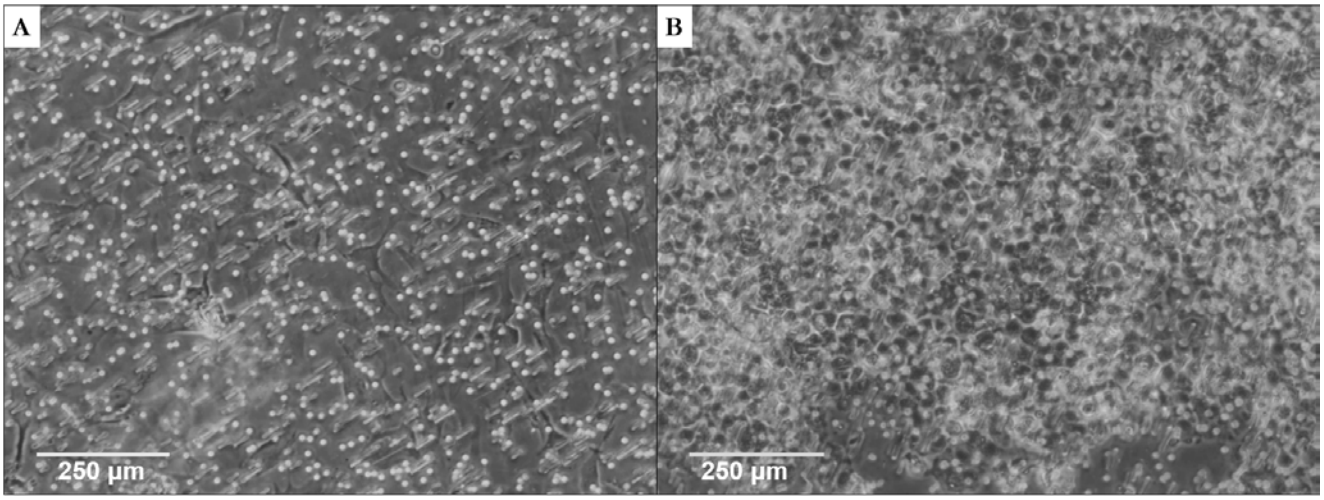

Figure 7.5: Results of cell culture in the chamber 24 hours after seeding. (A) Fibroblasts. (B) HaCaT cells.

The results of the cell seeding experiment (Fig. 7.5) indicate that the chamber can successfully host a simple cell culture. On the other hand, due to the limited volume of medium that the lower channel can hold, the cell culture could not be maintained for periods longer than 24 hours without refilling, given that at 24 hours a significant portion of the cells seeded on the chamber appeared dead or apoptotic. However, the cell culture could be maintained for 72 hours by refilling both the upper and lower channels with fresh medium every 24 hours. This problem suggests that a more sophisticated pump is required for long-term maintenance of the cell culture.

The dermal equivalent in the SoaC device is composed of a fibrin matrix with embedded fibroblasts; however, the formation of each of these fibrin matrices has been show to be strongly dependent on the materials and the conditions in which they are built . For this reason, an experiment was conducted to test whether the chamber allowed for a fibrin matrix to be formed inside.

Fibrinogen powder from human plasma (Sigma-Aldrich) was dissolved in a 0.9% (w/v) aqueous solution of NaCl (saline) to a concentration of 20 mg/ml and thrombin from human plasma (Sigma-Aldrich) was dissolved in 1 ml of $CaCl_2$ 25 mM. To prepare the hydrogel, 59 µl of the thrombin solution and 59 µl of Amchafibrin (Fides Ecopharma) were added to 707 µl of DMEM (10% FBS, 2.5% Atb/Atm). Dissolved fibrinogen (177 µl) was added in the last place to a final volume of 1 ml and briefly mixed.

The hydrogel preparation was quickly introduced in the upper chamber and allowed to polymerize inside an incubator at 37 °C and 5% CO_2 for 5 minutes. Approximately 10 µl were introduced in the chamber, while the remaining volume was allowed to polymerize inside the incubator for the same amount of time and taken as a gelation control (examined with the flip-flop method). After the dermal matrix was formed, the lower channel was filled with culture medium (DMEM + 10% FBS, 2.5% Atb/Atm) to maintain the turgency of the hydrogel. After 10 minutes, the device was open and directly inspected (Fig. 7.6). The experiment was conducted in duplicate.

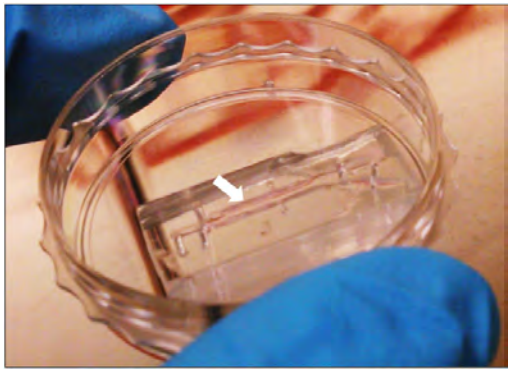

Figure 7.6: Formation of a fibrin matrix in the chamber. The hydrogel (arrow) can be seen by opening the device

Within 5 minutes of incubation, the fibrin matrix was formed inside the device, as evidenced by the fact that the upper chamber was clogged, preventing any fluid from being introduced into said chamber. Direct inspection of the inside of the device also revealed the presence of a fibrin hydrogel within the chamber (Fig. 7.6). Therefore, the chamber does not seem to interfere with the formation of the fibrin matrix.

Jointly, these two experiments demonstrate that the SoaC device is well suited to host a bioengineered skin equivalent. The formation of this equivalent inside the chip is, however, a complex process that requires several steps. Therefore a new protocol was developed for this purpose. It exploits the laminar flow regime that is characteristic of microfluidics. By simultaneously introducing two fluids through the double port system, a parallel flow of two fluids without mixing between streams can be established inside the upper chamber. This phenomenon can be utilized to allow for the *in situ* formation of a dermal matrix while leaving enough space for an epidermis and an air-liquid interface

within the chamber. Once the dermal matrix is formed, seeding the keratinocytes is straightforward, and suprabasal differentiation can be readily accomplished upon exposure to air (See Figure 7.8).

The efficacy of this new method to generate a skin organotypic culture inside the skin-on-a-chip device was examined as follows.

The fibrin hydrogel was prepared as previously described. Additionally, human fibroblasts were added to the DMEM, achieving a final concentration of $\sim 5 \cdot 10^5$ cells/ml in the hydrogel. This hydrogel preparation and PBS –used here as sacrificial material– were simultaneously introduced with two pipettes at a slow rate into the upper chamber through the outer and inner ports respectively. The fibrin hydrogel was allowed to react inside an incubator at 37 °C and 5% CO_2 for 5 minutes; after which the PBS was replaced by fresh medium (DMEM + 10% FBS + 2.5% atb/atm) and the lower channel was equally filled (with DMEM + 10% FBS + 2.5% atb/atm). Photographs were taken at this point (Olympus, SC30) and the device was left in the incubator for one hour.

HaCaT cells were then seeded in the upper chamber over the dermal matrix at a concentration of $\sim 10^6$ cells/ml. The space left after removing the sacrificial material could accommodate approximately a volume of 5 µl, resulting in $\sim 5 \cdot 10^3$ cells being seeded. The culture was incubated for one hour at 37 °C and 5% CO_2, allowing the HaCaT cells to settle on the surface and the fibroblasts to extend. After the incubation period, the device was again inspected.

Results obtained after the *in situ* formation of the fibrin matrix and the removal of the sacrificial material indicate the presence of fibroblasts in the upper chamber (Fig. 7.7a and 7.7b, white arrows), which demonstrates the adequacy of the parallel flow seeding method. Moreover, the sacrificial fluid left enough space to allow for HaCaT seeding (Fig. 7.7c and 7.7d), although the chambers were partially clogged at some points. These cells seemed to concentrate on the center of the channel (Fig. S5), which could be caused by the topography of the surface, the hydrophobicity of the lateral walls, hydrodynamic forces or short-range intermolecular interactions.

After the incubation period, HaCaT cells began to adhere to the surface (Fig. 7.7e) and around 30 minutes later some colonies started to form (Fig. 7.7f). Fibroblasts were also observed to extend cellular processes inside the matrix (Fig. 7.7g) within two hours of seeding.

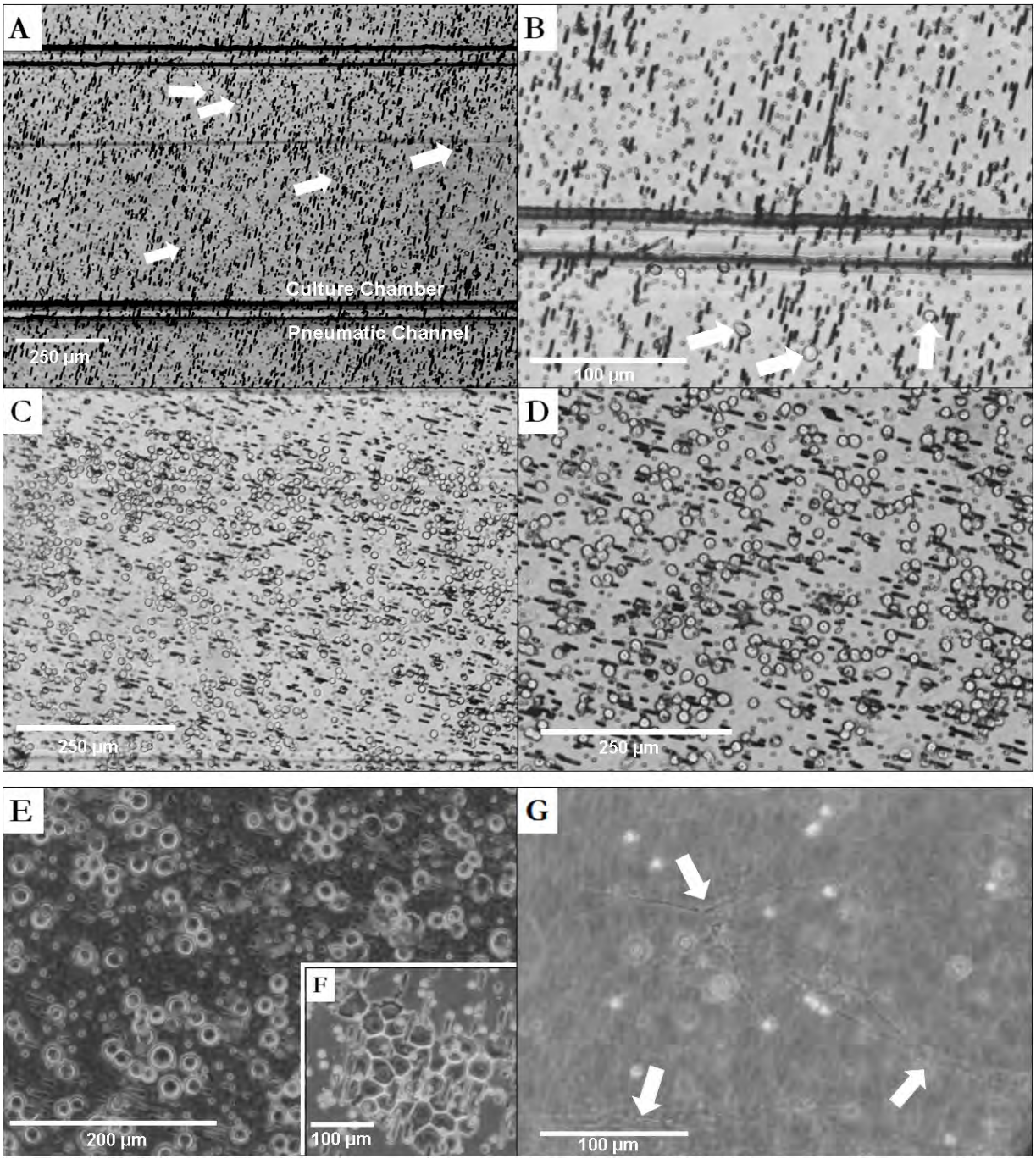

Figure 7.7: *In-situ* formation of a bioengineered skin equivalent inside the chamber. Fibroblasts (white arrows) embedded in the fibrin matrix remain in the chamber after removal of the sacrificial material (A, B) allowing HaCaT cells to be seeded over the dermal matrix (C, D). HaCaT cells begin to adhere to the to the surface 1 hour after seeding (E) and form some colonies 30 minutes later (F). Fibroblasts extend processes inside the matrix 2 hours after seeding (G).

Even though the manual seeding produces uneven results not well suited for applications, the results provided in the present work serve as a proof of concept. The use of high-precision perfusion pumps would allow to standardize the procedure. A summary of the novel seeding method developed for the skin-on-a-chip device is presented in Figure 7.8.

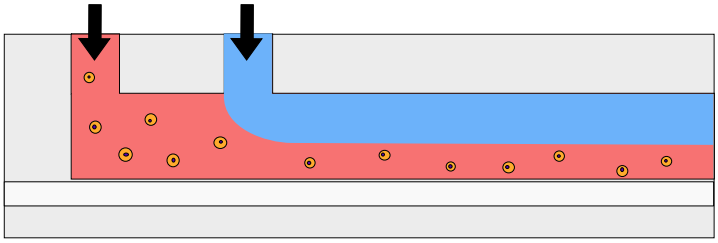

Step 1: The hydrogel solution and a sacrificial material are introduced through the double port to create a parallel flow

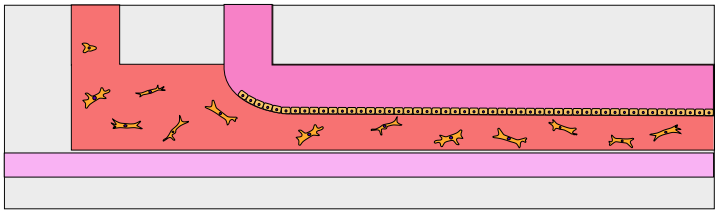

Step 4: After an hour, keratinocytes begin to settle into monolayer on the surface and fibroblasts expand within the hydrogel

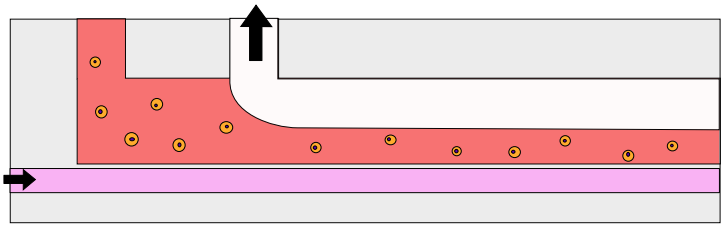

Step 2: The sacrificial material is removed once the dermal equivalent is formed (~5 minutes) and the lower channel is filled with medium

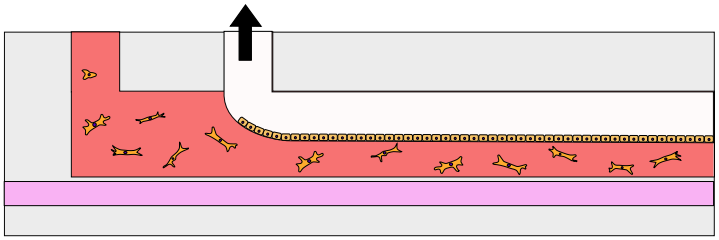

Step 5: Culture medium is removed from the upper chamber to generate an air-liquid interface that promotes suprabasal differentiation

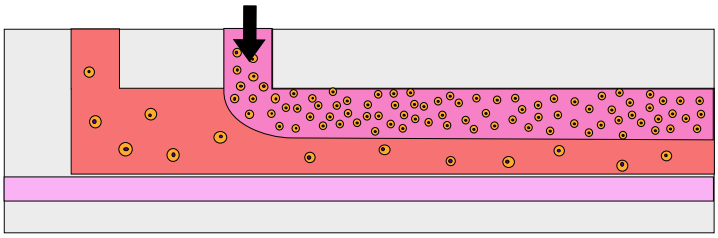

Step 3: Keratinocytes (HaCaT) are seeded on the space left by the sacrificial material

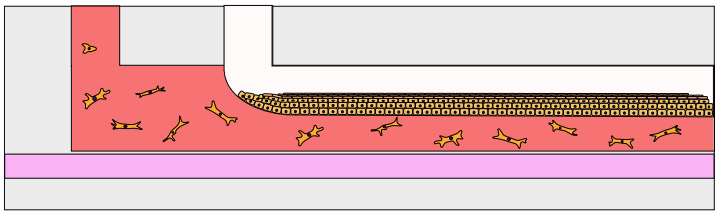

Step 6: Within 3-4 weeks, the epidermis is fully developed and a skin equivalent is formed

Figure 7.8: New protocol for *in-situ* formation for a skin equivalent inside the skin-on-a-chip device

8 Conclusion and future work

The present work describes the design, modeling, fabrication and examination of a skin-on-a-chip device. A biologically inspired skin biomimetic device was designed, featuring a microvascular channel, a 3D culture chamber and two lateral pneumatic channels for mechanical stimulation; and modeled according to principles of physiology and transport phenomena.

A complete fabrication protocol for skin-on-a-chip device was developed, exploring different alternative methods, and used to manufacture these microfluidic cell culture systems in accordance with the design. The devices were fabricated in three layers using a variety of microfabrication techniques, including photolithography, replica molding and microimprinting.

Two different membranes –a microfabricated PDMS membrane and a commercially available PC filter– were examined and characterized on the basis of cell adhesion, surface properties and surface functionalization as candidates to establish a porous interface between the microvascular channel and the culture chamber. Moreover, a novel bonding method, based on plasma treatment and silanization of the polycarbonate surface with APTES, was developed to integrate the selected PC membrane and the PDMS layers. Finally, cell seeding in the culture chamber as well as in-situ formation of a bioengineered skin equivalent with a newly developed method was demonstrated. Albeit not fully conclusive, these results offer a solid proof of concept of a skin on a chip device that can host a continuously perfused skin equivalent.

The mathematical model developed in Section 5 offers a simplified but insightful quantitative description of the device operation. In accordance with this model, the skin-on-a-chip device recapitulates certain physiological phenomena that are observed *in vivo* such as capillary transport dynamics, interstitial flow and cutaneous uptake of atmospheric oxygen. Furthermore, skin equivalents have been reported to recapitulate other physiological phenomena such as suprabasal differentiation, keratinization, lipid secretion and vitamin D synthesis [79, 123]. The next logical step is to move from transformed cell lines (HaCaT) to primary human cells that can better reproduce human biology. Although the mathematical model needs validation, using for instance imaging techniques such as PIV; and the skin equivalent

culture requires additional analysis; the present work serves as starting point for the development of an biomimetic microdevice that can recapitulate human skin for organ and disease modeling and drug screening.

Two main aspects of the skin-on-a-chip device have not been addressed in the present work, namely the endothelialization of the microvascular channel and the refinement of the pneumatic channels for operation. The formation of an endothelium in the vascular side of the membrane is fundamental to reproduce the transport properties of capillaries and to simulate inflammatory diseases. The endothelial barrier is also key in the development of an oncotic pressure that is responsible for the filtration-reabsorption profile. Cell adhesion on the polycarbonate membrane was shown to be normal in Section 6.4 and therefore endothelialization of the channel should be straightforward. Moreover, the surface treatment with APTES allows for further chemical modification of the PC surface to favor endothelial adhesion.

On the other hand, the pneumatic channels were not operational due to their poor mechanical stability. In fact, the failure of the walls is caused by their high aspect ratio, and therefore a decrease in the aspect ratio of the walls (i.e. increasing their thickness) could yield better results. However, the increase in thickness is limited by the deformability of the walls, given that they must collapse when a small vacuum is generated in these channels. Therefore, other alternative mechanisms should be explored such as piezoelectric materials, memory shape alloys or artificial muscles.

Although these tissue-on-a-chip technologies are still in their infancy, they have an outstanding potential. Current models are still relatively simple, and yet they display a variety of responses that cannot be observed in conventional cultures. More advanced and comprehensive models, based on primary human cells, are likely to arise in the near future, featuring more complex tissue architectures and interactions. In that regard, an advanced skin-on-a-chip model could incorporate hair, skin glands and other skin appendages.

The use of microfluidic technologies allows integration with other microfluidic systems and actuators such as gradient generators, micromixers, micropumps and microvalves [124] to provide remarkable functionalities that go far beyond the limitations of traditional cell culture systems. Moreover, the high

multiplexing capabilities of microfluidics allow multiple devices to be operated in parallel, reducing the cost of operation.

The next generation of organs on chips could incorporate on-chip sensors and actuators. A multitude of micro-scale sensors have been developed for biomedical devices, including pH, temperature and force sensors, optical sensors, electrodes for electrochemical measurements or biosensors for the concentration of particular biomolecules. In addition, actuators can be used to maintain the culture and environment conditions within desired ranges. Sensors and actuators can be integrated on the chip and controlled with custom-designed electronic circuits that can be included as part of the device. These hybrid devices will provide real time control and monitorization of the organ-on-a-chip response to a drug, allowing for automated drug screening results.

The future of microfluidic organs on chips lies in the development of body-on-a-chip devices presenting a diversity of interconnected organs that can recapitulate the individual organ physiology, the complex interactions among organs, their interplay, and the collective behavior that arises from it. These devices would also allow for more comprehensive and self-sustainable systems; replacing pumps with hearts-on-chips; pneumatic systems with artificial muscles; and computer control with integrated electronics and brains-on-chips.

In the future, these systems will have the capacity to closely replicate the extraordinary complexity of biological microenvironments and to reproduce the systemic response of the human body to a drug. Organs-on-chips have the potential to replace animals with innovative and cost-effective models of human biology that will aid in the development of new drugs with reduced expenses and development times and increased efficiency and success rate.

References

[1] M. Hay, D. W. Thomas, J. L. Craighead, C. Economides, and J. Rosenthal, "Clinical development success rates for investigational drugs," *Nat Biotech*, vol. 32, pp. 40–51, Jan. 2014.

[2] J. A. DiMasi, R. W. Hansen, and H. G. Grabowski, "The price of innovation: new estimates of drug development costs," *Journal of health economics*, vol. 22, no. 2, pp. 151–185, 2003.

[3] C. P. Adams and V. V. Brantner, "Estimating the cost of new drug development: Is it really 802 million," *Health Affairs*, vol. 25, pp. 420–428, Mar. 2006.

[4] S. M. Paul, D. S. Mytelka, C. T. Dunwiddie, C. C. Persinger, B. H. Munos, S. R. Lindborg, and A. L. Schacht, "How to improve r&d productivity: the pharmaceutical industry's grand challenge," *Nat Rev Drug Discov*, vol. 9, pp. 203–214, Mar. 2010.

[5] M. Esch, T. King, and M. Shuler, "The role of body-on-a-chip devices in drug and toxicity studies," *Annual Review of Biomedical Engineering*, vol. 13, no. 1, pp. 55–72, 2011. PMID: 21513459.

[6] R. M. Abrantes-Metz, C. Adams, and A. D. Metz, "Pharmaceutical development phases: a duration analysis," *FTC, Bureau of Economics Working Paper*, no. 274, 2004.

[7] S. Keyhani, M. Diener-West, and N. Powe, "Are development times for pharmaceuticals increasing or decreasing?," *Health Affairs*, vol. 25, pp. 461–468, Mar. 2006.

[8] J. A. DiMasi and L. Faden, "Factors associated with multiple fda review cycles and approval phase times," *Drug Information Journal*, vol. 43, no. 2, pp. 201–225, 2009.

[9] J. W. Scannell, A. Blanckley, H. Boldon, and B. Warrington, "Diagnosing the decline in pharmaceutical r&d efficiency," *Nat Rev Drug Discov*, vol. 11, pp. 191–200, Mar. 2012.

[10] F. Pammolli, L. Magazzini, and M. Riccaboni, "The productivity crisis in pharmaceutical r&d," *Nature Reviews. Drug Discovery*, vol. 10, pp. 428–438, June 2011.

[11] I. Kola and J. Landis, "Can the pharmaceutical industry reduce attrition rates?," *Nature reviews Drug discovery*, vol. 3, no. 8, pp. 711–716, 2004.

[12] J. Buzek and B. Ask, "Regulation (ec) no 1223/2009 of the european parliament and of the council of 30 november 2009 on cosmetic products," *Official Journal of the European Union L*, vol. 342, 2009.

[13] E. Commission., "Directive 2010/63/eu of the european parliament and of the council of 22 september 2010 on the protection of animals used for scientific purposes (text with eea relevance)," *Official Journal L 276*, vol. 53, pp. 33–79, 2010.

[14] M. Caron, P. Emans, M. Coolsen, L. Voss, D. Surtel, A. Cremers, L. Van Rhijn, and T. Welting, "Redifferentiation of dedifferentiated human articular chondrocytes: comparison of 2d and 3d cultures," *Osteoarthritis and Cartilage*, vol. 20, no. 10, pp. 1170–1178, 2012.

[15] D. Loessner, K. S. Stok, M. P. Lutolf, D. W. Hutmacher, J. A. Clements, and S. C. Rizzi, "Bioengineered 3d platform to explore cell-ecm interactions and drug resistance of epithelial ovarian cancer cells," *Biomaterials*, vol. 31, no. 32, pp. 8494–8506, 2010.

[16] R. L. Ehrmann and G. O. Gey, "The growth of cells on a transparent gel of reconstituted rat-tail collagen," *Journal of the National Cancer Institute*, vol. 16, no. 6, pp. 1375–1403, 1956.

[17] B. M. Baker and C. S. Chen, "Deconstructing the third dimension - how 3d culture microenvironments alter cellular cues," *Journal of cell science*, vol. 125, no. 13, pp. 3015–3024, 2012.

[18] D. Huh, G. A. Hamilton, and D. E. Ingber, "From 3d cell culture to organs-on-chips," *Trends in Cell Biology*, vol. 21, pp. 745–754, Dec. 2011.

[19] L. Martínez-Santamaría, S. Guerrero-Aspizua, and M. Del Río, "Skin bioengineering: Preclinical and clinical applications," *Actas Dermo-Sifiliográficas (English Edition)*, vol. 103, pp. 5–11, Jan. 2012.

[20] M. Garcia, M. J. Escamez, M. Carretero, I. Mirones, L. Martinez-Santamaria, M. Navarro, J. L. Jorcano, A. Meana, M. Del Rio, and F. Larcher, "Modeling normal and pathological processes through skin tissue engineering," *Molecular carcinogenesis*, vol. 46, no. 8, pp. 741–745, 2007.

[21] S. Guerrero-Aspizua, M. García, R. Murillas, L. Retamosa, N. Illera, B. Duarte, A. Holguín, S. Puig, M. I. Hernández, and A. Meana, "Development of a bioengineered skin-humanized mouse model for psoriasis: dissecting epidermal-lymphocyte interacting pathways," *The American journal of pathology*, vol. 177, no. 6, pp. 3112–3124, 2010.

[22] P. Avci, M. Sadasivam, A. Gupta, W. C. De Melo, Y.-Y. Huang, R. Yin, R. Chandran, R. Kumar, A. Otufowora, T. Nyame, and M. R. Hamblin, "Animal models of skin disease for drug discovery," *Expert Opinion on Drug Discovery*, vol. 8, no. 3, pp. 331–355, 2013. PMID: 23293893.

[23] G. M. Whitesides, "The origins and the future of microfluidics," *Nature*, vol. 442, no. 7101, pp. 368–373, 2006.

[24] A. Folch, *Introduction to BioMEMS*. CRC Press, 2012.

[25] T. M. Squires and S. R. Quake, "Microfluidics: Fluid physics at the nanoliter scale," *Reviews of modern physics*, vol. 77, no. 3, p. 977, 2005.

[26] N. L. Jeon, S. K. Dertinger, D. T. Chiu, I. S. Choi, A. D. Stroock, and G. M. Whitesides, "Generation of solution and surface gradients using microfluidic systems," *Langmuir*, vol. 16, no. 22, pp. 8311–8316, 2000.

[27] G. M. Walker, J. Sai, A. Richmond, M. Stremler, C. Y. Chung, and J. P. Wikswo, "Effects of flow and diffusion on chemotaxis studies in a microfabricated gradient generator," *Lab on a Chip*, vol. 5, no. 6, pp. 611–618, 2005.

[28] S. K. Dertinger, D. T. Chiu, N. L. Jeon, and G. M. Whitesides, "Generation of gradients having complex shapes using microfluidic networks," *Analytical Chemistry*, vol. 73, no. 6, pp. 1240–1246, 2001.

[29] H. Kaji, G. Camci-Unal, R. Langer, and A. Khademhosseini, "Engineering systems for the generation of patterned co-cultures for controlling cell-cell interactions," *Biochimica et Biophysica Acta (BBA)-General Subjects*, vol. 1810, no. 3, pp. 239–250, 2011.

[30] A. Khademhosseini, L. Ferreira, J. Blumling, J. Yeh, J. M. Karp, J. Fukuda, and R. Langer, "Co-culture of human embryonic stem cells with murine embryonic fibroblasts on microwell-patterned substrates," *Biomaterials*, vol. 27, no. 36, pp. 5968–5977, 2006.

[31] K. Gupta, D.-H. Kim, D. Ellison, C. Smith, A. Kundu, J. Tuan, K.-Y. Suh, and A. Levchenko, "Lab-on-a-chip devices as an emerging platform for stem cell biology," *Lab on a Chip*, vol. 10, no. 16, pp. 2019–2031, 2010.

[32] D. van Noort, S. M. Ong, C. Zhang, S. Zhang, T. Arooz, and H. Yu, "Stem cells in microfluidics," *Biotechnology progress*, vol. 25, no. 1, pp. 52–60, 2009.

[33] D. Wlodkowic and J. M. Cooper, "Tumors on chips: oncology meets microfluidics," *Current opinion in chemical biology*, vol. 14, no. 5, pp. 556–567, 2010.

[34] S. Chung, R. Sudo, V. Vickerman, I. K. Zervantonakis, and R. D. Kamm, "Microfluidic platforms for studies of angiogenesis, cell migration, and cell-cell interactions," *Annals of biomedical engineering*, vol. 38, no. 3, pp. 1164–1177, 2010.

[35] M.-H. Wu, S.-B. Huang, and G.-B. Lee, "Microfluidic cell culture systems for drug research," *Lab on a Chip*, vol. 10, no. 8, pp. 939–956, 2010.

[36] P. S. Dittrich and A. Manz, "Lab-on-a-chip: microfluidics in drug discovery," *Nature Reviews Drug Discovery*, vol. 5, no. 3, pp. 210–218, 2006.

[37] S. N. Bhatia and D. E. Ingber, "Microfluidic organs-on-chips," *Nat Biotech*, vol. 32, pp. 760–772, Aug. 2014.

[38] C. Moraes, G. Mehta, S. C. Lesher-Perez, and S. Takayama, "Organs-on-a-chip: a focus on compartmentalized microdevices," *Annals of biomedical engineering*, vol. 40, no. 6, pp. 1211–1227, 2012.

[39] K. Ohashi, T. Yokoyama, M. Yamato, H. Kuge, H. Kanehiro, M. Tsutsumi, T. Amanuma, H. Iwata, J. Yang, and T. Okano, "Engineering functional two-and three-dimensional liver systems in vivo using hepatic tissue sheets," *Nature medicine*, vol. 13, no. 7, pp. 880–885, 2007.

[40] C. Y. Li, K. R. Stevens, R. E. Schwartz, B. S. Alejandro, J. H. Huang, and S. N. Bhatia, "Micropatterned cell-cell interactions enable functional encapsulation of primary hepatocytes in hydrogel microtissues," *Tissue Engineering Part A*, vol. 20, no. 15-16, pp. 2200–2212, 2014.

[41] A. Sivaraman, J. Leach, S. Townsend, T. Iida, B. Hogan, D. B. Stolz, R. Fry, L. Samson, S. Tannenbaum, and L. Griffith, "A microscale in vitro physiological model of the liver: predictive screens for drug metabolism and enzyme induction," *Current drug metabolism*, vol. 6, no. 6, pp. 569–591, 2005.

[42] P. J. Lee, P. J. Hung, and L. P. Lee, "An artificial liver sinusoid with a microfluidic endothelial-like barrier for primary hepatocyte culture," *Biotechnology and bioengineering*, vol. 97, no. 5, pp. 1340–1346, 2007.

[43] K.-J. Jang, A. P. Mehr, G. A. Hamilton, L. A. McPartlin, S. Chung, K.-Y. Suh, and D. E. Ingber, "Human kidney proximal tubule-on-a-chip for drug transport and nephrotoxicity assessment," *Integrative Biology*, vol. 5, no. 9, pp. 1119–1129, 2013.

[44] G. J. Mahler, M. B. Esch, R. P. Glahn, and M. L. Shuler, "Characterization of a gastrointestinal tract microscale cell culture analog used to predict drug toxicity," *Biotechnology and bioengineering*, vol. 104, no. 1, pp. 193–205, 2009.

[45] H. J. Kim and D. E. Ingber, "Gut-on-a-chip microenvironment induces human intestinal cells to undergo villus differentiation," *Integrative Biology*, vol. 5, no. 9, pp. 1130–1140, 2013.

[46] H. J. Kim, D. Huh, G. Hamilton, and D. E. Ingber, "Human gut-on-a-chip inhabited by microbial flora that experiences intestinal peristalsis-like motions and flow," *Lab on a Chip*, vol. 12, no. 12, pp. 2165–2174, 2012.

[47] S.-H. Park, W. Y. Sim, B.-H. Min, S. S. Yang, A. Khademhosseini, and D. L. Kaplan, "Chip-based comparison of the osteogenesis of human bone marrow-and adipose tissue-derived mesenchymal stem cells under mechanical stimulation," 2012.

[48] D. R. Myers, Y. Sakurai, R. Tran, B. Ahn, E. T. Hardy, R. Mannino, A. Kita, M. Tsai, and W. A. Lam, "Endothelialized microfluidics for studying microvascular interactions in hematologic diseases," *Journal of visualized experiments: JoVE*, no. 64, pp. –, 2012.

[49] D. Huh, B. D. Matthews, A. Mammoto, M. Montoya-Zavala, H. Y. Hsin, and D. E. Ingber, "Reconstituting organ-level lung functions on a chip," *Science*, vol. 328, no. 5986, pp. 1662–1668, 2010.

[50] A. Grosberg, A. P. Nesmith, J. A. Goss, M. D. Brigham, M. L. McCain, and K. K. Parker, "Muscle on a chip: in vitro contractility assays for smooth and striated muscle," *Journal of pharmacological and toxicological methods*, vol. 65, no. 3, pp. 126–135, 2012.

[51] G. A. Giridharan, M.-D. Nguyen, R. Estrada, V. Parichehreh, T. Hamid, M. A. Ismahil, S. D. Prabhu, and P. Sethu, "Microfluidic cardiac cell culture model (microcccm)," *Analytical chemistry*, vol. 82, no. 18, pp. 7581–7587, 2010.

[52] Y.-s. Torisawa, C. S. Spina, T. Mammoto, A. Mammoto, J. C. Weaver, T. Tat, J. J. Collins, and D. E. Ingber, "Bone marrow-on-a-chip replicates hematopoietic niche physiology in vitro," *Nature methods*, vol. 11, no. 6, pp. 663–669, 2014.

[53] R. Gómez-Sjöberg, A. A. Leyrat, D. M. Pirone, C. S. Chen, and S. R. Quake, "Versatile, fully automated, microfluidic cell culture system," *Analytical chemistry*, vol. 79, no. 22, pp. 8557–8563, 2007.

[54] F. Deiss, A. Mazzeo, E. Hong, D. E. Ingber, R. Derda, and G. M. Whitesides, "Platform for high-throughput testing of the effect of soluble compounds on 3d cell cultures," *Analytical chemistry*, vol. 85, no. 17, pp. 8085–8094, 2013.

[55] P. M. van Midwoud, M. T. Merema, E. Verpoorte, and G. M. Groothuis, "A microfluidic approach for in vitro assessment of interorgan interactions in drug metabolism using intestinal and liver slices," *Lab on a Chip*, vol. 10, no. 20, pp. 2778–2786, 2010.

[56] S. M. Hattersley, C. E. Dyer, J. Greenman, and S. J. Haswell, "Development of a microfluidic device for the maintenance and interrogation of viable tissue biopsies," *Lab on a Chip*, vol. 8, no. 11, pp. 1842–1846, 2008.

[57] J. H. Sung and M. L. Shuler, "A micro cell culture analog (ucca) with 3-d hydrogel culture of multiple cell lines to assess metabolism-dependent cytotoxicity of anti-cancer drugs," *Lab on a Chip*, vol. 9, no. 10, pp. 1385–1394, 2009.

[58] N. Futai, W. Gu, J. W. Song, and S. Takayama, "Handheld recirculation system and customized media for microfluidic cell culture," *Lab on a Chip*, vol. 6, no. 1, pp. 149–154, 2006.

[59] D. Huh, D. C. Leslie, B. D. Matthews, J. P. Fraser, S. Jurek, G. A. Hamilton, K. S. Thorneloe, M. A. McAlexander, and D. E. Ingber, "A human disease model of drug toxicity-induced pulmonary edema in a lung-on-a-chip microdevice," *Science translational medicine*, vol. 4, no. 159, pp. 159ra147–159ra147, 2012.

[60] D. Huh, B. D. Matthews, A. Mammoto, M. Montoya-Zavala, H. Y. Hsin, and D. E. Ingber, "Reconstituting organ-level lung functions on a chip," *Science*, vol. 328, no. 5986, pp. 1662–1668, 2010.

[61] W. J. Polacheck, R. Li, S. G. Uzel, and R. D. Kamm, "Microfluidic platforms for mechanobiology," *Lab on a Chip*, vol. 13, no. 12, pp. 2252–2267, 2013.

[62] A. W. Orr, B. P. Helmke, B. R. Blackman, and M. A. Schwartz, "Mechanisms of mechanotransduction," *Developmental Cell*, vol. 10, pp. 11–20, Jan. 2006.

[63] D. E. Ingber, "Cellular mechanotransduction: putting all the pieces together again," *The FASEB journal*, vol. 20, no. 7, pp. 811–827, 2006.

[64] Y. Imura, K. Sato, and E. Yoshimura, "Micro total bioassay system for ingested substances: assessment of intestinal absorption, hepatic metabolism, and bioactivity," *Analytical chemistry*, vol. 82, no. 24, pp. 9983–9988, 2010.

[65] H. Kimura, T. Yamamoto, H. Sakai, Y. Sakai, and T. Fujii, "An integrated microfluidic system for long-term perfusion culture and on-line monitoring of intestinal tissue models," *Lab Chip*, vol. 8, no. 5, pp. 741–746, 2008.

[66] R. Baudoin, A. Legendre, S. Jacques, J. Cotton, F. Bois, and E. Leclerc, "Evaluation of a liver microfluidic biochip to predict in vivo clearances of seven drugs in rats," *Journal of pharmaceutical sciences*, vol. 103, no. 2, pp. 706–718, 2014.

[67] P. Chao, T. Maguire, E. Novik, K.-C. Cheng, and M. Yarmush, "Evaluation of a microfluidic based cell culture platform with primary human hepatocytes for the prediction of hepatic clearance in human," *Biochemical pharmacology*, vol. 78, no. 6, pp. 625–632, 2009.

[68] Y.-C. Toh, T. C. Lim, D. Tai, G. Xiao, D. van Noort, and H. Yu, "A microfluidic 3d hepatocyte chip for drug toxicity testing," *Lab on a Chip*, vol. 9, no. 14, pp. 2026–2035, 2009.

[69] M. Crosera, M. Bovenzi, G. Maina, G. Adami, C. Zanette, C. Florio, and F. F. Larese, "Nanoparticle dermal absorption and toxicity: a review of the literature," *International archives of occupational and environmental health*, vol. 82, no. 9, pp. 1043–1055, 2009.

[70] G. J. Tortora and B. H. Derrickson, *Principles of anatomy and physiology*. Wiley, 2011.

[71] L. C. Junqueira and J. Carneiro, *Basic histology: text and atlas*. London: McGraw Hill, 2005, 2005.

[72] F. H. Silver, L. M. Siperko, and G. P. Seehra, "Mechanobiology of force transduction in dermal tissue," *Skin Research and Technology*, vol. 9, no. 1, pp. 3–23, 2003.

[73] J. D. Sibonga, H. J. Evans, H. Sung, E. Spector, T. Lang, V. Oganov, A. Bakulin, L. Shackelford, and A. LeBlanc, "Recovery of spaceflight-induced bone loss: bone mineral density after long-duration missions as fitted with an exponential function," *Bone*, vol. 41, no. 6, pp. 973–978, 2007.

[74] N. Wang, J. P. Butler, and D. E. Ingber, "Mechanotransduction across the cell surface and through the cytoskeleton," *Science*, vol. 260, no. 5111, pp. 1124–1127, 1993.

[75] N. Wang, J. D. Tytell, and D. E. Ingber, "Mechanotransduction at a distance: mechanically coupling the extracellular matrix with the nucleus," *Nature reviews Molecular cell biology*, vol. 10, no. 1, pp. 75–82, 2009.

[76] D. E. Ingber, "Tensegrity: the architectural basis of cellular mechanotransduction," *Annual review of physiology*, vol. 59, no. 1, pp. 575–599, 1997.

[77] M. S. Chin, R. Ogawa, L. Lancerotto, G. Pietramaggiori, K. T. Schomacker, J. C. Mathews, S. S. Scherer, P. Van Duyn, M. J. Prsa, and M. P. Ottensmeyer, "In vivo acceleration of skin growth using a servo-controlled stretching device," *Tissue Engineering Part C: Methods*, vol. 16, no. 3, pp. 397–405, 2009.

[78] D. Huh, H. J. Kim, J. P. Fraser, D. E. Shea, M. Khan, A. Bahinski, G. A. Hamilton, and D. E. Ingber, "Microfabrication of human organs-on-chips," *Nat. Protocols*, vol. 8, pp. 2135–2157, Nov. 2013.

[79] V. M. Schoop, N. Mirancea, and N. E. Fusenig, "Epidermal organization and differentiation of hacat keratinocytes in organotypic coculture with human dermal fibroblasts," *Journal of Investigative Dermatology*, vol. 112, no. 3, pp. 343–353, 1999.

[80] M. A. Unger, H.-P. Chou, T. Thorsen, A. Scherer, and S. R. Quake, "Monolithic microfabricated valves and pumps by multilayer soft lithography," *Science*, vol. 288, no. 5463, pp. 113–116, 2000.

[81] K.-L. Tung, Y.-L. Chang, and C.-J. Chuang, "Effect of pore morphology on fluid flow through track-etched polycarbonate membrane," *Tamkang Journal of Science and Engineering*, vol. 4, no. 2, pp. 127–132, 2001.

[82] G. A. Truskey, F. Yuan, and D. F. Katz, *Transport phenomena in biological systems*. Pearson/Prentice Hall Upper Saddle River NJ:, 2004.

[83] A. Thomas, J. Tan, and Y. Liu, "Characterization of nanoparticle delivery in microcirculation using a microfluidic device," *Microvascular Research*, vol. 94, no. 0, pp. 17 – 27, 2014.

[84] J. Tan, S. Shah, A. Thomas, H. D. Ou-Yang, and Y. Liu, "The influence of size, shape and vessel geometry on nanoparticle distribution," *Microfluidics and nanofluidics*, vol. 14, pp. 77–87, July 2012.

[85] J. C. del Álamo, G. N. Norwich, Y.-s. J. Li, J. C. Lasheras, and S. Chien, "Anisotropic rheology and directional mechanotransduction in vascular endothelial cells," *Proceedings of the National Academy of Sciences*, vol. 105, pp. 15411–15416, Oct. 2008.

[86] J. N. Topper and M. A. Gimbrone Jr, "Blood flow and vascular gene expression: fluid shear stress as a modulator of endothelial phenotype," *Molecular Medicine Today*, vol. 5, pp. 40–46, Jan. 1999.

[87] P. F. Davies, A. Robotewskyj, and M. L. Griem, "Quantitative studies of endothelial cell adhesion. directional remodeling of focal adhesion sites in response to flow forces.," *Journal of Clinical Investigation*, vol. 93, pp. 2031–2038, May 1994.

[88] J. M. Rutkowski and M. A. Swartz, "A driving force for change: interstitial flow as a morphoregulator," *Trends in Cell Biology*, vol. 17, pp. 44–50, Jan. 2007.

[89] W. J. Polacheck, J. L. Charest, and R. D. Kamm, "Interstitial flow influences direction of tumor cell migration through competing mechanisms," *Proceedings of the National Academy of Sciences*, vol. 108, pp. 11115–11120, July 2011.

[90] C. Pozrikidis and D. Farrow, "A model of fluid flow in solid tumors," *Annals of Biomedical Engineering*, vol. 31, no. 2, pp. 181–194, 2003.

[91] J. R. Levick, "Flow through interstitium and other fibrous matrices," *Quarterly Journal of Experimental Physiology*, vol. 72, no. 4, pp. 409–437, 1987.

[92] K. N. Richmond, R. D. Shonat, R. M. Lynch, and P. C. Johnson, "Critical po2 of skeletal muscle in vivo," *American Journal of Physiology-Heart and Circulatory Physiology*, vol. 277, no. 5, pp. H1831–H1840, 1999.

[93] D. Goldman, "Theoretical models of microvascular oxygen transport to tissue," *Microcirculation*, vol. 15, no. 8, pp. 795–811, 2008.

[94] M. Sücker, A. Struk, P. Altmeyer, M. Herde, H. Baumgärtl, and D. W. Lübbers, "The cutaneous uptake of atmospheric oxygen contributes significantly to the oxygen supply of human dermis and epidermis," *The Journal of physiology*, vol. 538, no. 3, pp. 985–994, 2002.

[95] S. Mitragotri, Y. G. Anissimov, A. L. Bunge, H. F. Frasch, R. H. Guy, J. Hadgraft, G. B. Kasting, M. E. Lane, and M. S. Roberts, "Mathematical models of skin permeability: An overview," *International journal of pharmaceutics*, vol. 418, no. 1, pp. 115–129, 2011.

[96] J. C. McDonald and G. M. Whitesides, "Poly(dimethylsiloxane) as a material for fabricating microfluidic devices," *Acc. Chem. Res.*, vol. 35, pp. 491–499, Apr. 2002.

[97] F. Schneider, J. Draheim, R. Kamberger, and U. Wallrabe, "Process and material properties of polydimethylsiloxane (pdms) for optical mems," *Sensors and Actuators A: Physical*, vol. 151, pp. 95–99, Apr. 2009.

[98] G. Shao, "Polymer based microfabrication and its applications in optical mems and biomems," 2011.

[99] J. R. Anderson, D. T. Chiu, H. Wu, O. J. Schueller, and G. M. Whitesides, "Fabrication of microfluidic systems in poly (dimethylsiloxane)," *Electrophoresis*, vol. 21, pp. 27–40, 2000.

[100] Y. Xia and G. M. Whitesides, "Soft lithography," *Angewandte Chemie International Edition*, vol. 37, no. 5, pp. 550–575, 1998.

[101] W. Kern, "Handbook of semiconductor wafer cleaning technology," *New Jersey: Noyes Publication*, pp. 111–196, 1993.

[102] Z. Cai, W. Qiu, G. Shao, and W. Wang, "A new fabrication method for all-pdms waveguides," *Sensors and Actuators A: Physical*, vol. 204, pp. 44–47, 2013.

[103] M. Zhang, J. Wu, L. Wang, K. Xiao, and W. Wen, "A simple method for fabricating multi-layer pdms structures for 3d microfluidic chips," *Lab Chip*, vol. 10, pp. 1199–1203, 2010.

[104] J. de Jong, R. G. H. Lammertink, and M. Wessling, "Membranes and microfluidics: a review," *Lab Chip*, vol. 6, no. 9, pp. 1125–1139, 2006.

[105] K. Toda, S.-I. Ohira, and M. Ikeda, "Micro-gas analysis system microgas comprising a microchannel scrubber and a micro-fluorescence detector for measurement of hydrogen sulfide," *Analytica chimica acta*, vol. 511, no. 1, pp. 3–10, 2004.

[106] H. Makamba, J. H. Kim, K. Lim, N. Park, and J. H. Hahn, "Surface modification of poly (dimethylsiloxane) microchannels," *Electrophoresis*, vol. 24, no. 21, pp. 3607–3619, 2003.

[107] D. Fuard, T. Tzvetkova-Chevolleau, S. Decossas, P. Tracqui, and P. Schiavone, "Optimization of poly-di-methyl-siloxane (PDMS) substrates for studying cellular adhesion and motility," *Microelectron. Eng.*, vol. 85, pp. 1289–1293, May 2008.

[108] K. Y. Chumbimuni-Torres, R. E. Coronado, A. M. Mfuh, C. Castro-Guerrero, M. F. Silva, G. R. Negrete, R. Bizios, and C. D. Garcia, "Adsorption of proteins to thin-films of pdms and its effect on the adhesion of human endothelial cells," *RSC Advances*, vol. 1, no. 4, pp. 706–714, 2011.

[109] P. Apel, "Track etching technique in membrane technology," *Radiation Measurements*, vol. 34, pp. 559–566, June 2001.

[110] S. Hediger, A. Sayah, J. Horisberger, and M. Gijs, "Modular microsystem for epithelial cell culture and electrical characterisation," *Biosensors and Bioelectronics*, vol. 16, no. 9, pp. 689–694, 2001.

[111] S. Thorslund, O. Klett, F. Nikolajeff, K. Markides, and J. Bergquist, "A hybrid poly (dimethylsiloxane) microsystem for on-chip whole blood filtration optimized for steroid screening," *Biomedical microdevices*, vol. 8, no. 1, pp. 73–79, 2006.

[112] J. H. Lee, S. J. Lee, G. Khang, and H. B. Lee, "Interaction of fibroblasts on polycarbonate membrane surfaces with different micropore sizes and hydrophilicity," *Journal of Biomaterials Science, Polymer Edition*, vol. 10, no. 3, pp. 283–294, 1999.

[113] M. A. Eddings, M. A. Johnson, and B. K. Gale, "Determining the optimal PDMS-PDMS bonding technique for microfluidic devices," *Journal of Micromechanics and Microengineering*, vol. 18, no. 6, p. 067001, 2008.

[114] C.-W. Tsao and D. L. DeVoe, "Bonding of thermoplastic polymer microfluidics," *Microfluidics and Nanofluidics*, vol. 6, no. 1, pp. 1–16, 2009.

[115] C. Tsao, L. Hromada, J. Liu, P. Kumar, and D. DeVoe, "Low temperature bonding of pmma and coc microfluidic substrates using uv/ozone surface treatment," *Lab on a Chip*, vol. 7, no. 4, pp. 499–505, 2007.

[116] K. S. Lee and R. J. Ram, "Plastic-pdms bonding for high pressure hydrolytically stable active microfluidics," *Lab on a Chip*, vol. 9, no. 11, pp. 1618–1624, 2009.

[117] K. Kim, S. W. Park, and S. S. Yang, "The optimization of pdms-pmma bonding process using silane primer," *BioChip Journal*, vol. 4, no. 2, pp. 148–154, 2010.

[118] C. Li and G. L. Wilkes, "The mechanism for 3-aminopropyltriethoxysilane to strengthen the interface of polycarbonate substrates with hybrid organic-inorganic sol-gel coatings," *Journal of Inorganic and Organometallic Polymers*, vol. 7, no. 4, pp. 203–216, 1997.

[119] V. Sunkara, D.-K. Park, H. Hwang, R. Chantiwas, S. A. Soper, and Y.-K. Cho, "Simple room temperature bonding of thermoplastics and poly (dimethylsiloxane)," *Lab on a Chip*, vol. 11, no. 5, pp. 962–965, 2011.

[120] G. T. Hermanson, *Bioconjugate techniques*. Academic press, 2013.

[121] A. Mata, A. Fleischman, and S. Roy, "Characterization of polydimethylsiloxane (pdms) properties for biomedical micro/nanosystems," *Biomedical Microdevices*, vol. 7, no. 4, pp. 281–293, 2005.

[122] K. Efimenko, W. E. Wallace, and J. Genzer, "Surface modification of sylgard-184 poly (dimethyl siloxane) networks by ultraviolet and ultraviolet/ozone treatment," *Journal of colloid and interface science*, vol. 254, no. 2, pp. 306–315, 2002.

[123] B. Lehmann, "Hacat cell line as a model system for vitamin d3 metabolism in human skin," *Journal of investigative dermatology*, vol. 108, no. 1, pp. 78–82, 1997.

[124] A. K. Au, H. Lai, B. R. Utela, and A. Folch, "Microvalves and micropumps for biomems," *Micromachines*, vol. 2, no. 2, pp. 179–220, 2011.

[125] S. Denniss and J. Rush, "Polyvinylpyrrolidone can be used to cost-effectively increase the viscosity of culture media," *The FASEB Journal*, vol. 29, no. 1 Supplement, pp. 1029–19, 2015.

[126] P. Wanichapichart, T. Chittrakarn, W. Sujaritturakarn, and H. G. Coster, "Production of nuclear-track etched membranes," *Science Asia*, vol. 26, pp. 175–179, 2000.

[127] T. Bakmand, D. Kwasny, M. Dimaki, and W. E. Svendsen, "Fabrication and characterisation of membrane-based gold electrodes," *Electroanalysis*, vol. 27, no. 1, pp. 217–224, 2015.

[128] C. L. Chiu, V. Hecht, H. Duong, B. Wu, and B. Tawil, "Permeability of three-dimensional fibrin constructs corresponds to fibrinogen and thrombin concentrations," *BioResearch open access*, vol. 1, no. 1, pp. 34–40, 2012.

[129] R. Sander, "Compilation of henry's law constants for inorganic and organic species of potential importance in environmental chemistry," 1999.

[130] M. Radisic, W. Deen, R. Langer, and G. Vunjak-Novakovic, "Mathematical model of oxygen distribution in engineered cardiac tissue with parallel channel array perfused with culture medium containing oxygen carriers," *American Journal of Physiology-Heart and Circulatory Physiology*, vol. 288, no. 3, pp. H1278–H1289, 2005.

[131] K.-P. Wilhelm, P. Elsner, E. Berardesca, and H. I. Maibach, *Bioengineering of the skin: skin imaging & analysis*. CRC Press, 2006.

Annex I: Supplementary figures

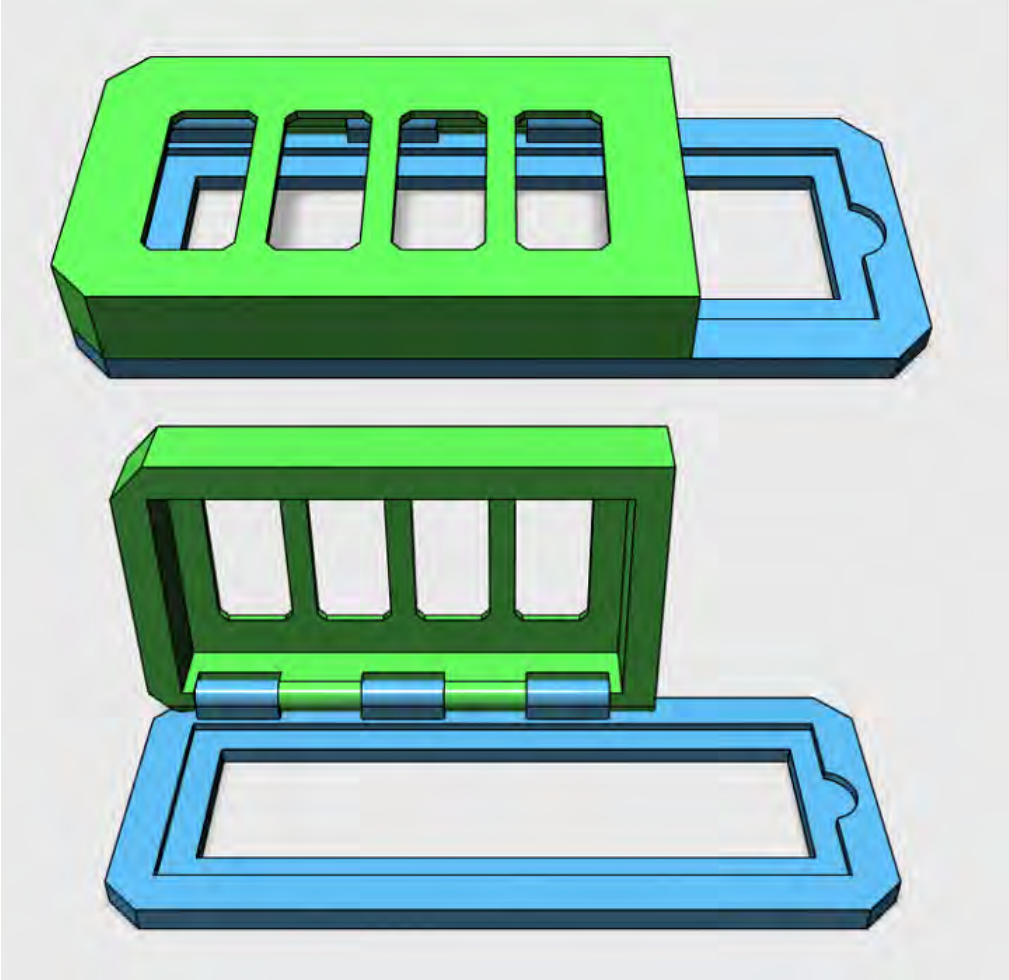

Figure S1: Multi-chip holder design for parallel operation. Up to four skin-on-a-chip devices can be assembled on a microscopy glass slide with a simple plasma treatment. The frosted part of the slide is left outside for labeling. The holder features four independent observation windows and a locking system, and it could incorporate microfluidic connections and ports to internally connect each holder to a single inlet.

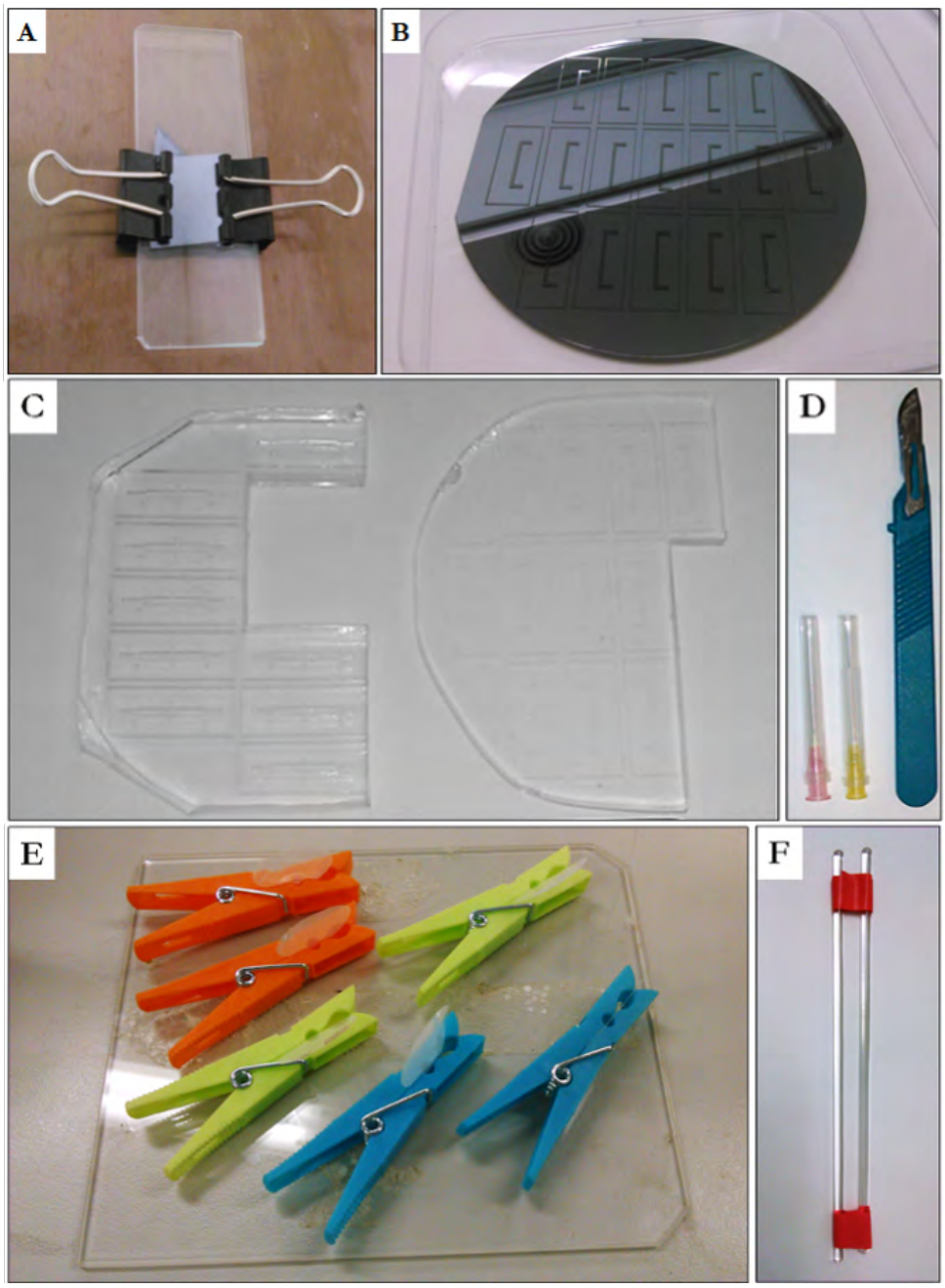

Figure S2: SU-8 master, PDMS replicas and tools used in microfabrication. (A) Contact lithography and microimprinting. (B) Su-8 master for the lower layer. (C) PDMS replicas of the master (D) Tools used to prepare single chips (E) Stands for plasma treatment of PC filters (F) Support for PC filters during silane curing

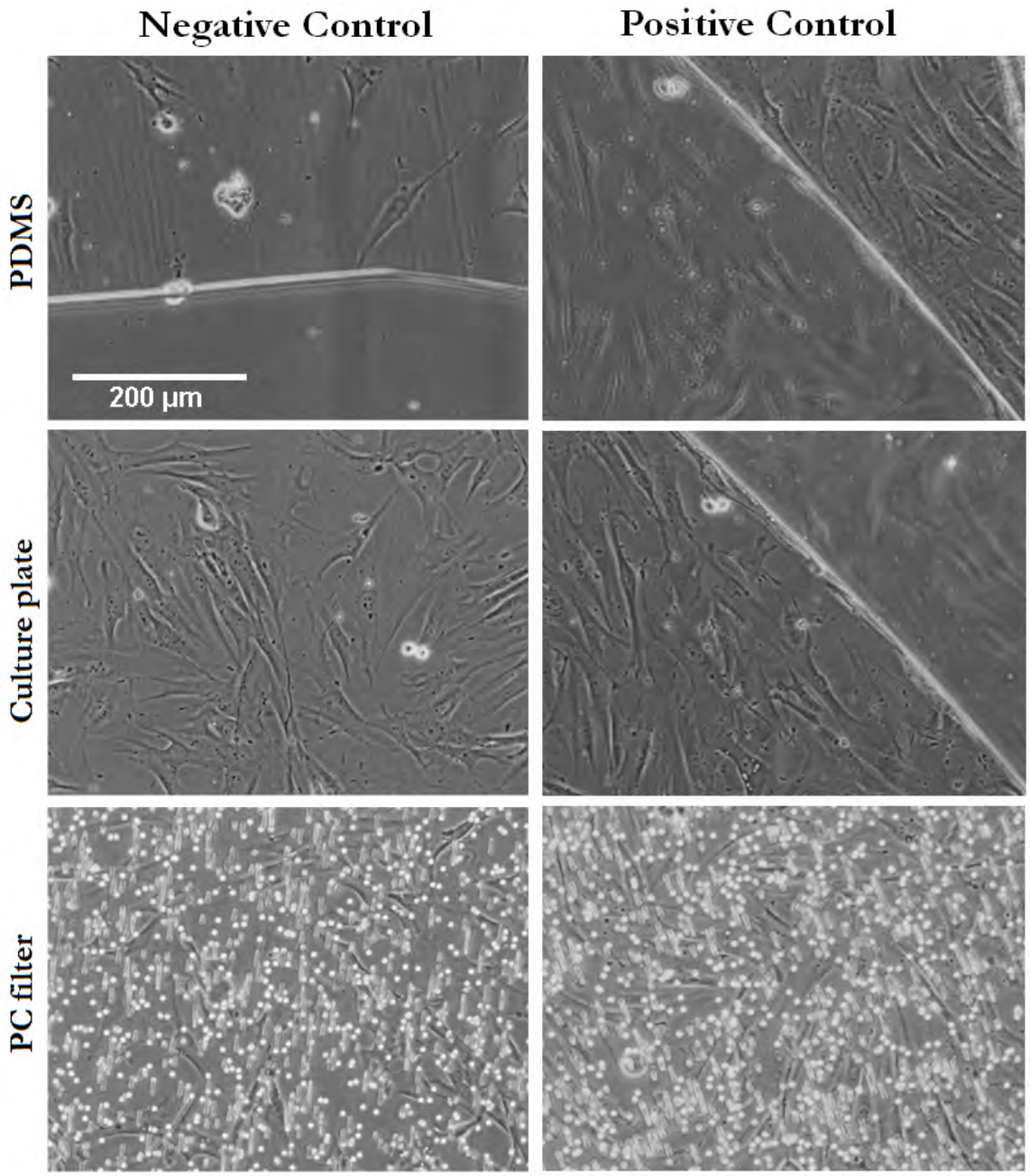

Figure S3: Control for the collagen functionalization of PC. PC and PDMS membranes were simultaneously functionalized in the same plate to perform an adhesion assay, comparing cell adhesion to untreated (Negative control, left) and collagen-treated (Positive control, right) membranes. PC and PDMS membranes were functionalized; and cells were incubated for 24 hours; as previously described. Untreated PDMS membranes and both PC membranes were placed on a different surface after incubation to facilitate the visualization. Collagen functionalization proves to be effective in PDMS, hence the lack of differences between treated and untreated PC is not caused by a error in the functionalization process.

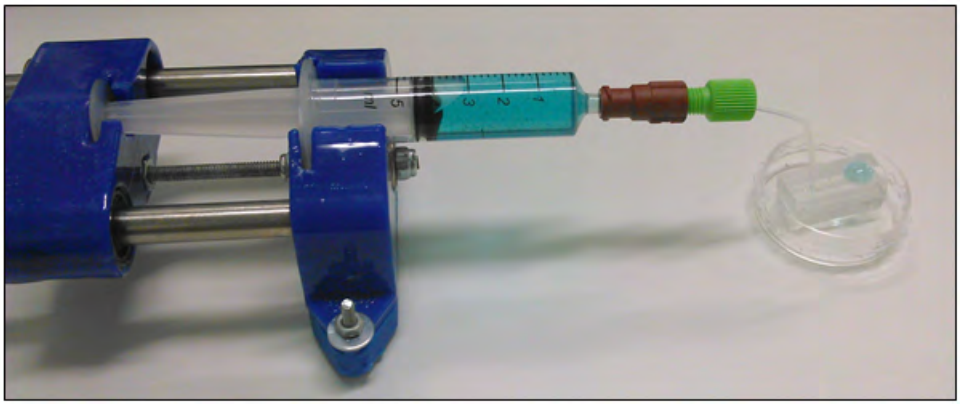

Figure S4: Operation of the chip using the custom built syringe pump. Detail of the pump and microfluidic circuit with colored water and no waste tubing

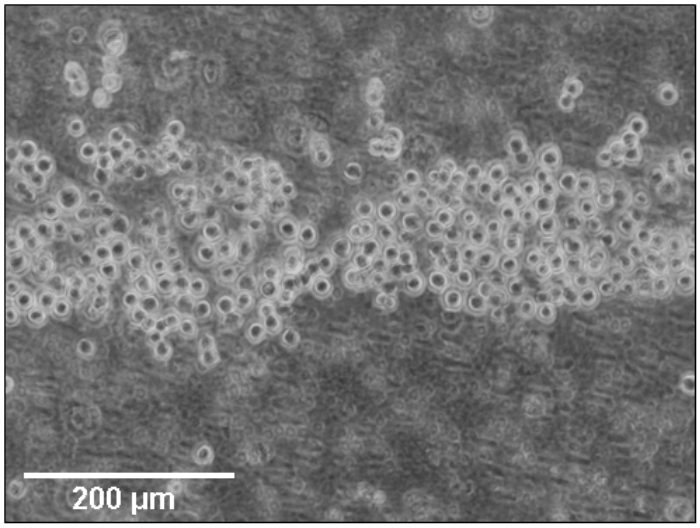

Figure S5: HaCaT cell seeded in the chamber after the *in-situ* gelation of the fibrin matrix seem to self-assemble, focusing on the center of the channel after the incubation period (1 hour)

Annex II: Derivation of equations and selection of parameters

This annex provides a more detailed derivation of selected equations for future traceability of the mathematical model as well as a table with the values selected for the model coefficients and their origin.

Pressure field in the channel

In Section (5.1) an equation for the pressure was developed:

$$\frac{\partial^2 P(x)}{\partial x^2} - kP(x) \quad = -k\Pi \tag{59}$$

This equation can be solved by assuming an homogeneous and a particular solution $P_h + P_p$. The roots of the characteristic polynomial of the homogeneous equation are $\lambda = +\sqrt{k}$, $\lambda = -\sqrt{k}$, and the root for the particular equation is $\lambda = 0$. Thus, the root factorization of the polynomial is given by $\lambda\left(\lambda - \sqrt{k}\right)\left(\lambda + \sqrt{k}\right)$, and thus the general solution is:

$$P(x) = \underbrace{C_1 \cdot e^{\sqrt{k}x} + C_2 \cdot e^{-\sqrt{k}x}}_{=P_h} + \underbrace{C_3}_{=P_p} \tag{60}$$

The particular solution, i.e. $P_p = C_3$, must satisfy the differential equation. Given that $\frac{\partial^2 P(x)}{\partial x^2} = 0$, substitution into the ODE above yields:

$$-kC_3 = -k\Pi \rightarrow C_3 = \Pi \tag{61}$$

The coefficients $C_1,\ C_2$ are determined by setting $P(x = 0) = P_1,\ P(x = L) = P_2$

Wall Shear Stress

The shear acting on the endothelium has been show to be a key factor in the regulation of endothelial call behavior. The viscous shear stress is caused by viscous forces of the fluid acting on the walls. The

stress vector is defined by:

$$\vec{\tau} = \begin{pmatrix} \tau_{xx} & \tau_{xy} & \tau_{xz} \\ \tau_{yx} & \tau_{yy} & \tau_{yz} \\ \tau_{zx} & \tau_{zy} & \tau_{zz} \end{pmatrix} \cdot \vec{n} \tag{62}$$

where τ_{ij} is the ij-th component of the stress tensor and $\vec{n}$ is the vector normal to the surface pointing towards the fluid. This stress tensor is symmetric ad thus the elements below the diagonal are henceforth omitted. For a newtonian, incompressible fluid with viscosity μ, the stress vector acting on the upper wall is:

$$\vec{\tau} = \mu \begin{pmatrix} 2\frac{\partial v_X}{\partial x} & \left(\frac{\partial v_x}{\partial y} + \frac{\partial v_y}{\partial x}\right) & \left(\frac{\partial v_x}{\partial z}\right) \\ - & 2\frac{\partial v_y}{\partial y} & \left(\frac{\partial v_y}{\partial z}\right) \\ - & - & 0 \end{pmatrix} \cdot \begin{pmatrix} 0 \\ -1 \\ 0 \end{pmatrix} = -\mu \begin{pmatrix} \left(\frac{\partial v_X}{\partial y} + \frac{\partial v_y}{\partial x}\right) \\ 2\frac{\partial v_y}{\partial y} \\ \left(\frac{\partial v_X}{\partial z}\right) \end{pmatrix} \Bigg|_{y=\frac{h}{2}} \tag{63}$$

In this particular case, only the component acting perpendicular to the wall along the direction of the flow, i.e. the x-component of the stress vector. Moreover, as previously explained, the x-derivatives can be neglected. Therefore, the wall shear stress acting on the endothelium is given by:

$$\tau_w = -\mu \frac{\partial v_x}{\partial y}\bigg|_{y=\frac{h}{2}} \tag{64}$$

The expression for $v_x(x, y, z)$ given by equation (14) can be readily differentiated, yielding

$$\tau_w(x, z) = Pl(x) \cdot h \left[\frac{1}{2} - 4 \cdot \sum_{n=0}^{\infty} \frac{\cosh\left((2n+1)\frac{\pi z}{h}\right)}{(2n+1)^2 \pi^2 \cosh\left((2n+1)\frac{\pi w}{2h}\right)}\right] \tag{65}$$

The wall shear stress therefore varies with the pressure gradient along the microchannel as well as with the position across the channel's width. As a result, endothelial cells near the border will be subjected to different levels of shear stress than those at the center. An average wall shear stress can be obtained by averaging the expression above:

$$\langle \tau_w \rangle_z = Pl(x) \cdot \frac{h}{2} \left[1 - 16\frac{h}{w} \cdot \sum_{n=0}^{\infty} \frac{\tanh\left((2n+1)\frac{\pi w}{2h}\right)}{(2n+1)^3 \pi^3}\right] \tag{66}$$

Interstitial pressure field

Equation (33) describes the interstitial pressure field inside the dermis:

$$P = C_o(y-H) + \sum_{n=1}^{\infty} C_n \left(e^{-\frac{n\pi}{L}y} - e^{\frac{n\pi}{L}(y-2H)}\right) \cos\left(\frac{n\pi x}{L}\right) \tag{67}$$

The coefficients C_o and C_n are determined by the boundary condition $\frac{\partial P}{\partial y}(x,0) = -\frac{\mu}{\phi} v_{int}(x)$. Consider $\frac{\partial P}{\partial y}(x,y)$ at $y=0$

$$\left.\frac{\partial P}{\partial y}(x,y)\right|_{y=0} = C_o + \sum_{n=1}^{\infty} -C_n \cdot \frac{n\pi}{L}\left(1 + e^{-2H\frac{n\pi}{L}}\right) \cos\left(\frac{n\pi x}{L}\right) \tag{68}$$

This expression has the form of a cosine-base Fourier series:

$$f(x) = \frac{A_o}{2} + \sum_{n=1}^{\infty} A_n \cos\left(\frac{n\pi x}{L}\right) \tag{69}$$

with $A_o = 2C_o$ and $A_n = -C_n \cdot \frac{n\pi}{L}\left(1 + e^{-2H\frac{n\pi}{L}}\right)$ and $f(x) = -\frac{\mu}{\phi} v_{int}(x)$. The coefficients can be readily obtained by applying the Fourier series analysis equation:

$$\begin{aligned} A_o = &\quad \tfrac{2}{L}\textstyle\int_0^L f(x)\ dx \\ A_n = &\quad \tfrac{2}{L}\textstyle\int_0^L f(x)\cdot\cos\left(\frac{n\pi x}{L}\right)\ dx \end{aligned} \tag{70}$$

$$\begin{aligned} C_o = &\quad -\tfrac{\mu}{\phi L}\textstyle\int_0^L \delta\left(c_1\cdot e^{\sqrt{k}x} + c_2\cdot e^{-\sqrt{k}x}\right)\ dx \\ C_n = &\quad \tfrac{2\mu}{n\pi\phi\left(1+e^{-2H\frac{n\pi}{L}}\right)}\textstyle\int_0^L \delta\left(c_1\cdot e^{\sqrt{k}x} + c_2\cdot e^{-\sqrt{k}x}\right)\cdot\cos\left(\frac{n\pi x}{L}\right)\ dx \end{aligned} \tag{71}$$

$$\begin{aligned} C_o = &\quad -\tfrac{\mu\delta}{L\phi}\tfrac{1}{\sqrt{k}}\left[C_1\cdot e^{\sqrt{k}x} - C_2\cdot e^{-\sqrt{k}x}\right]_0^L \\ C_n = &\quad \tfrac{2\mu\delta}{n\pi\phi\left(1+e^{-2H\frac{n\pi}{L}}\right)}\left[C_1\cdot\tfrac{e^{\sqrt{k}x}\left(\sqrt{k}\cos\left(\frac{n\pi x}{L}\right)+\frac{n\pi x}{L}\sin\left(\frac{n\pi x}{L}\right)\right)}{\left(\frac{n\pi x}{L}\right)^2+k} - C_2\cdot\tfrac{e^{-\sqrt{k}x}\left(\sqrt{k}\cos\left(\frac{n\pi x}{L}\right)-\frac{n\pi x}{L}\sin\left(\frac{n\pi x}{L}\right)\right)}{\left(\frac{n\pi x}{L}\right)^2+k}\right]_0^L \end{aligned} \tag{72}$$

This method to determine the coefficients is common to all series expressions of PDE solutions such as those for the velocity profile in the channel $v_x(x, y, z)$ given by equation (14), the transverse velocity $v_y(x, y, z)$ given by equation (28) or the second form of the interstitial pressure $P_2(x, y)$ given by equation (37)

Parameter values

Table S1: Parameter values selected for the mathematical model

Parameter	**Selected value**	**Source**
Medium viscosity μ (Without FBS)	$1.14 \cdot 10^{-3}$ Pa $\cdot$ s	Obtained from literature: [125]
Medium density ρ	$0.99 \cdot 10^{3}$ kg $\cdot$ m^{-3}	Taken to be approximately that of water
Membrane conductivity per unit thickness δ	10^{-8} m $\cdot$ s^{-1} $\cdot$ Pa^{-1}	Estimated from literature: [81, 126, 127]
Fibrin specific permeability ϕ	$6.68 \cdot 10^{-12}$ m^2	Estimated from literature: [128]
Henry constant for Oxygen k_H	1.3 mol $\cdot$ m^{-3} $\cdot$ atm^{-1}	Obtained from literature: [129]
Oxygen concentration at the interface C_a	0.273 mol $\cdot$ m^{-3}	Calculated
Oxygen concentration in the channel C_o	0.222 mol $\cdot$ m^{-3}	Obtained from literature: [130]
Oxygen Michaelis constant K_M	$0.67 - 2.7$ μM	Obtained from literature [82]
Diffusion coefficient – Dermis D_1	$1 \cdot 10^{-9}$ m^2 $\cdot$ s^{-1}	Obtained from literature: [131]
Diffusion coefficient – Epidermis D_2	$3 \cdot 10^{-9}$ m^2 $\cdot$ s^{-1}	Obtained from literature: [131]
Oxygen consumption – Dermis R_1	$1.47 \cdot 10^{-4}$ mol $\cdot$ m^{-3} $\cdot$ s^{-1}	Estimated from literature: [94, 130]
Oxygen consumption – Epidermis R_2	$1.99 \cdot 10^{-4}$ mol $\cdot$ m^{-3} $\cdot$ s^{-1}	Estimated from literature: [94, 130]
Flow rate Q	$2.8 \cdot 10^{-10}$ m^3 $\cdot$ s^{-1}	Determined by the pump
Resistance of the microvascular channel R_C	$3.3 \cdot 10^{10}$ Pa $\cdot$ m^{-3} $\cdot$ s	Calculated
Resistance of the outlet R_o	$8.9 \cdot 10^{9}$ Pa $\cdot$ m^{-3} $\cdot$ s	Calculated
Inlet pressure P_1	12.5 Pa	Calculated
Outlet pressure P_2	2.5 Pa	Calculated
Oncotic Pressure Π	7.5 Pa	Can be determined by dextran concentration*
Microvascular channel length L	$1.3 \cdot 10^{-2}$ m	Determined by design
Microvascular channel width w	$8 \cdot 10^{-4}$ m	Determined by design
Microvascular channel height h	$2 \cdot 10^{-4}$ m	Determined by design
Dermis thickness H_1	$3 \cdot 10^{-4}$ m	Determined by design
Epidermis thickness H_2	10^{-4} m	Determined by design

*Dextran are commonly used in medicine as plasma expanders. Their extremely large molecular weight makes the endothelium extremely impermeable to them. They can be added to the medium to tune the oncotic pressure to the requirements

Annex III: Advanced pump prototype

In the present work, the pump is driven by a low-power stepper motor (Stepper motor - NEMA-17 size - 200 steps/rev, 12V 350mA). The stepper motor is set to operate at very low speeds (~ 4 steps/sec) and large torques are not required to pump the fluid at these low speeds. For this reason, the stepper motor can be driven at a lower voltage. At 5 V, and taking the winding resistance to be 35 Ω(according to specifications), the motor requires ~ 143 mA of current to operate. The Arduino Uno board is capable of supplying the 5 V voltage and up to 200 mA of current; enough to drive the motor.

This circuit, however, is too simplistic and severely limited in terms of power for the motor. A more advanced circuit can be built unit a driver as show in Figure S6

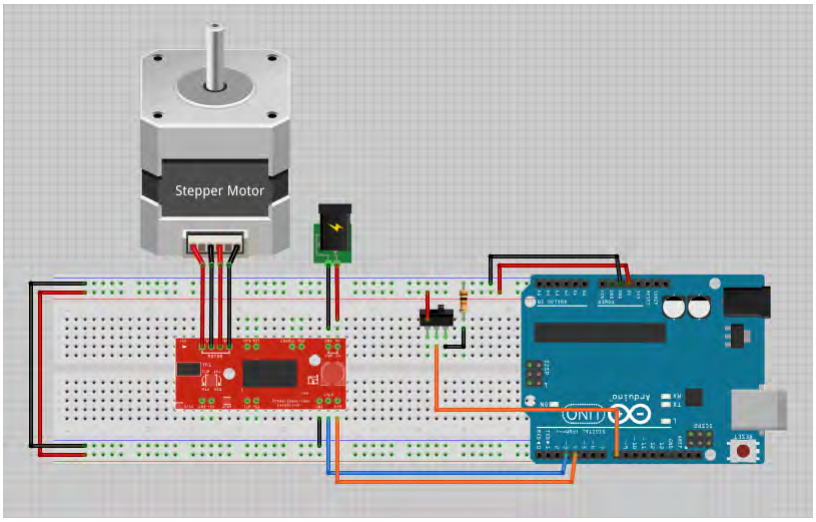

Figure S6: Electronic circuit for the pump with a driver

The motor driver can be used to provide the rated voltage to the motor. Moreover, it allows for *microstepping,* increasing the effective number of steps and therefore reducing the minimum flow rate by the same factor. A pump driven by this circuit could provide smaller, smoother and more precise flow rates.

A second prototype was built according to these specifications with an Easy Driver (Sparkfun) and

selecting pins 3 and 4 on the Adruino Uno board as *step* and *direction* pins respectively. The *setSpeed* was increased to 10 steps/sec and the microstepping was set to 1/8. This effectively increased the number of steps by a factor of 8 and provided a flow rate of approximately $\sim 5 \cdot 10^{-10}\,\mathrm{m}^3/\mathrm{s}$ (versus a theoretical flow rate of $\sim 6 \cdot 10^{-10}\,\mathrm{m}^3/\mathrm{s}$). The second prototype is still a work in progress and therefore was not used in the present work as perfusion pump.

Annex IV: Planning, budget and estimated production cost

Project Planning

The skin-on-a-chip project comprises 7 main phases spanning over the course of one year: Preliminary Work, Microfabrication I, Membrane Selection, Final Design, Microfabrication II, Cell Culture Testing and Dissertation Writing. The planning and details of each phase are presented in Figures S7 and S8. Key milestones in the project include the start of the collaboration with the microfabrication group at the CTB, the fabrication of the test and definitive masters, the selection of the membrane, the order and delivery of the microfluidic masters and the PC filters, the completion of the fabrication protocol and the proof of concept of the device operation.

Project Budget

The budget of this project has been divided in two main categories: materials, reagents and tools that were purchased specifically for the project (Table S2); and laboratory reagents, materials and personnel workhours that were consumed in the project (Table S3). Most of the purchased materials were acquired because they were previously unavailable, but they were not fully consumed in the present work. Cost of materials have been classified into different groups in accordance with their purpose.

Table S2: Budget of materials purchased for the project

Microfabrication

Product Description	Reference	Units	Price per unit (€)	Cost (€)
Acetate mask and masters (2 units)	Microfluidic Masters (microLIQUID)	2	200.00	400.00
Silicone elastomer kit (PDMS)	Sylgard 184 (Dow Corning)	1 (1.1 kg)	126.70	126.70
X10 Glass stirring rod D 6mm L 25 mm	11703783 (Fisher Scientific)	1 (10 units)	61.40	61.40
Disposable Cup 150 ml	030901B (DD BioLab)	1 (100 units)	42.74	42.74
Filter membranes, Isopore track-etched polycarbonate	P9699-100EA (Sigma Aldrich)	1 (100 units)	145.40	145.40
(3-Aminopropyl)triethoxysilane 99%	440140-500ML (Sigma Aldrich)	1 (500 ml)	275.80	275.80
			Subtotal	1052.04

Microfluidic Circuit

Product Description	Reference	Units	Price per unit (€)	Cost (€)
Tubing, PFA Teflon, .020"ID x 1/16"OD x 20'	UP-1512 (IDEX)	1	77.47	77.47
Tubing, PFA Teflon, .030"ID x 1/16"OD x 20'	UP-1514 (IDEX)	1	77.47	77.47
1/4-28 FEMALE TO FEMALE LUER PEEK	UP-P-658 (IDEX)	1	22.20	22.20
NATURAL 1/16" FLANGELESS FERRULE, TEFZEL, 10/PK	UP-P-200NX (IDEX)	1 (10 units)	21.94	21.94
GREEN - 1/16" FLANGELESS MALE NUT, DELRIN, 1/4-28	UP-P-205 (IDEX)	25	2.24	56.00
			Subtotal	255.08

Perfusion Pump

Product Description	Reference	Units	Price per unit (€)	Cost (€)
Ardunio Uno board	A000066(Arduino)	1	29.14	29.14
NEMA 17 Stepper Motor 200 steps/rev 12 V, 350 mA 20 Ncm	324 (Adafruit)	1	17.90	17.90
Easy Driver	ROB-12779 (Sparkfun)	1	15.60	15.60
IC replacement	A3967SLBTR-T (RS)	1	3.52	3.52
Linear Bearings LM8UU	(Repparts 3D)	1 (12 units)	10.00	10.00
Threaded rod M4 x 075	-	1	1.45	1.45
Smooth rod	-	1	3.00	3.00
Bolts and nuts (M4)	-	1	3.50	3.50
ABS coil	-	1 (1 kg)	22.00	22.00
			Subtotal	106.11
			Total Cost (€)	**1413.23**

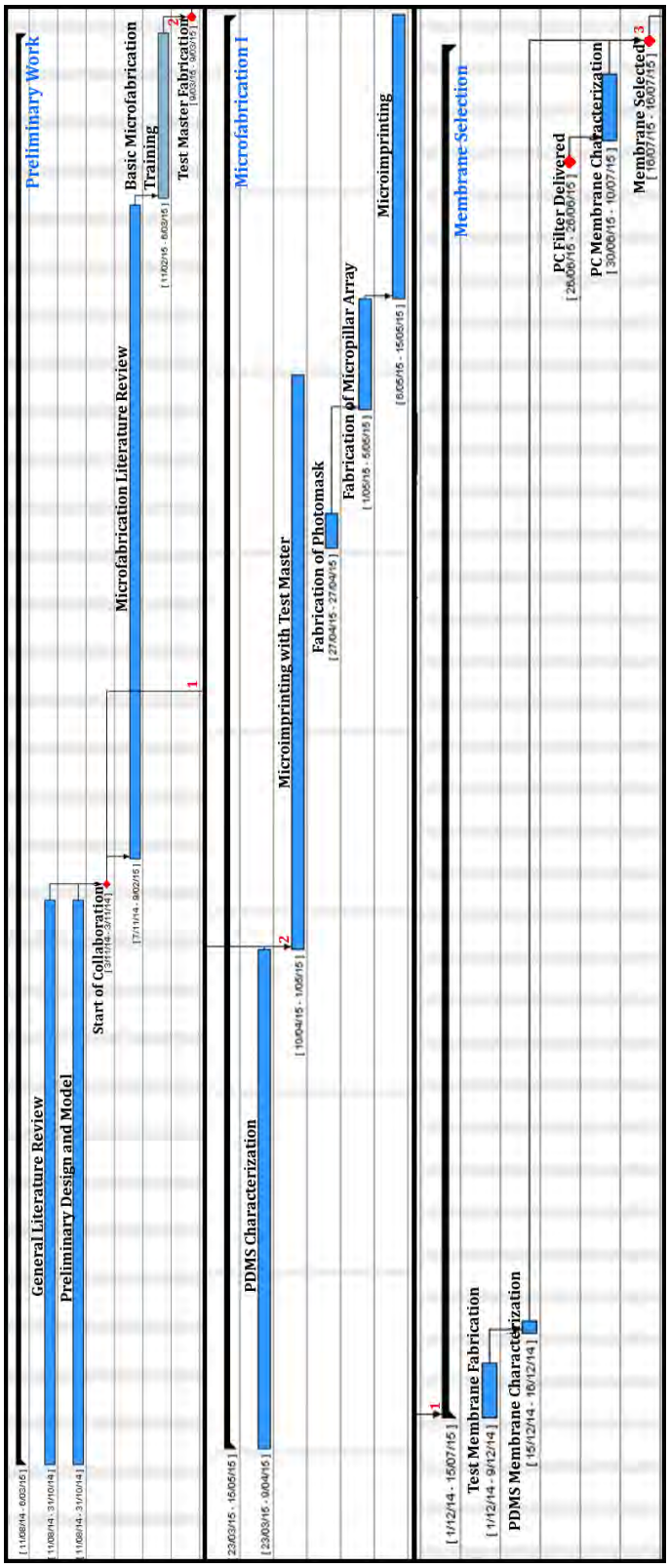

Figure S7: First section of the project planning including the first three phases: Preliminary work, Microfabrication I and Membrane selection. The key milestones of this section are the start of the collaboration with a microfabrication group (1), that is needed to start the the membrane characterization and the microfabrication work; and the fabrication of a test master (2) to begin the development of the microfabrication process; as well as the delivery of the PC filters. This section ends with the selection of a membrane (3) that allows to continue towards the second section

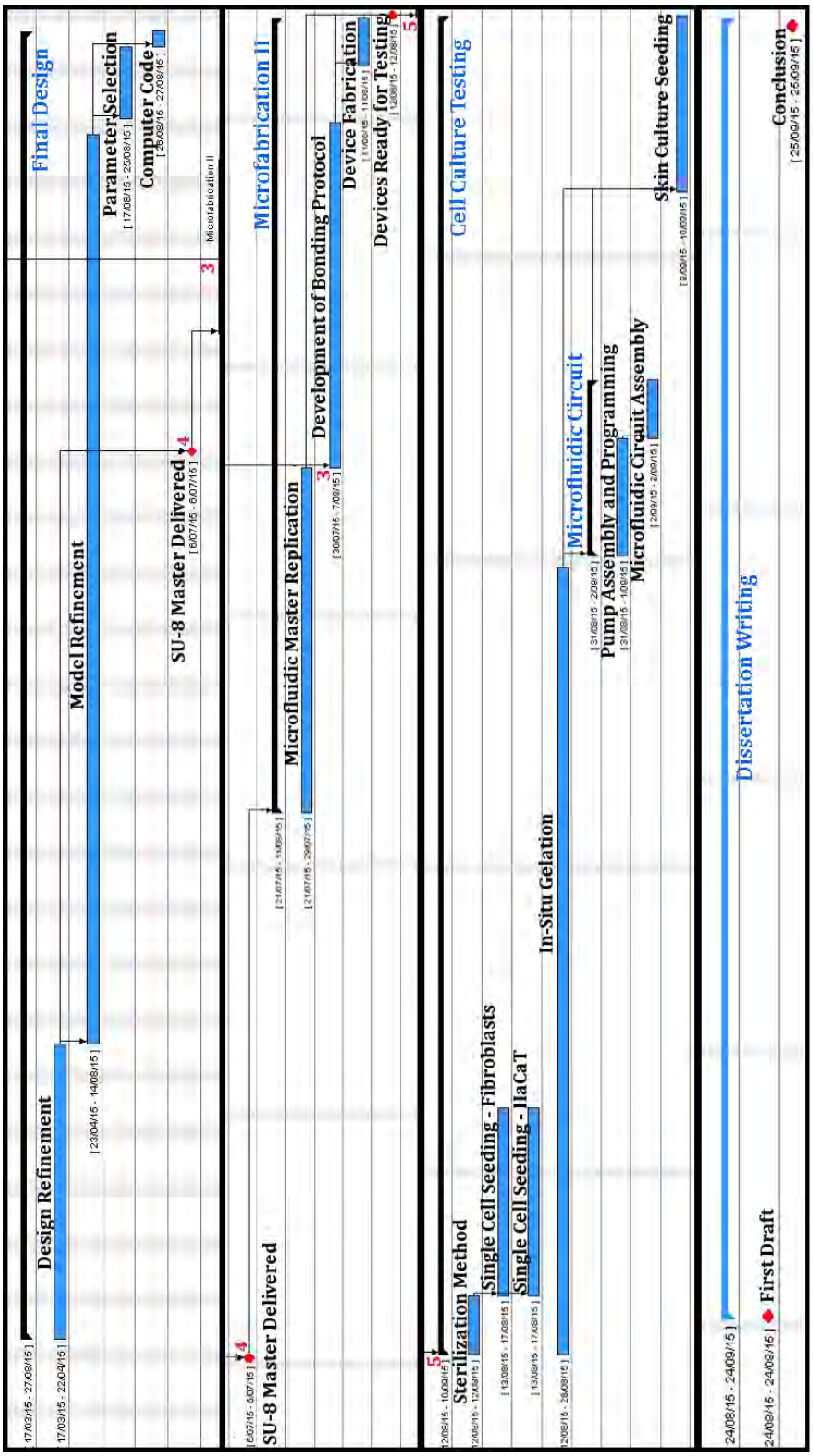

Figure S8: Second section of the project planning including the last four phases: Final Design, Microfabrication II, Cell Culture Testing and Dissertation Writing. Key milestones are the selection of a membrane (previous section) that is needed to start developing the bonding protocol (3); the delivery of the microfluidic SU-8 masters based on the final design (4) that is required for the second microfabrication phase; and the completion of the device fabrication (5) to begin the cell culture tests.

Table S3: Budget of laboratory materials and personnel workhours consumed

Consumables

Product Description	Reference	Price per item (€)	Amount Consumed	Cost (€)
10793344 - X12 FILTRATION UNIT 250ML 0,1µM	10793344	104.02	2 Units	17.34
X500 Culture Dish, PS, 100x20mm, Tissue Culture Treated, Sterile, 20/bag	10075371	389.14	15 Units	11.67
X500 Culture Dish, PS, 35x10mm, Tissue Culture Treated, Sterile, 20/bag	10556661	267.26	50 Uits	26.73
X16 245mm Square BioAssay Dish without Handles, not TC-Treated Culture, Sterile.	10737041	200.89	10 Units	125.56
X1000 Serological Pipet, PS, 1ml, Individually Paper/ Plastic Wrapped, Sterile.	10074450	270.30	50 Units	13.52
X10000 PIPETTE TIP 1000µL	-	49.61	800 Units	3.97
X1000 PIPETTE TIP 10µL	-	12.13	160 Units	1.94
X100 GUANTES NITRILO CONFORT T6,5	10226293	14.54	2 Boxes	29.08
X50 Falcon Tubes 15ML	CTGP-E15-050	7.05	100 Units	14.10
X50 Falcon Tubes 50ML	CTSP-E50-050	8.12	25 Units	4.06
X500 MICROTUBE NATUREL 1,5ML	11926955	14.16	10 Units	0.28
			Subtotal	248.24

Reagents

Product Description	Reference	Price per item (€)	Amount Consumed	Cost (€)
DMEM High W/GlutaMax - I 500ML	11574516	20.33	500 ml	20.33
FBS Qualite Recherche US 500ML	10309433	99.80	50 ml	9.98
Antibiotic/Antimicotic Sol 100ML	11536481	35.43	12.5 ml	4.43
Trypsin 0.05% 1X +0,2%EDTA 500ML	11581861	16.07	50 ml	1.61
Thrombin from human plasma	T8885-10VL	277.50	1 ml	277.50
Fibrinogen from human plasma. 50-70% protein (≥80% of protein is clottable) 1G	F3879-1G	311.90	0.1 g	31.19
Amchafibrin	CN-700506	3.14	1 ml	0.52
Collagen from calf skin. Type I (0.1% sol. in 0.1 M acetic acid) 20ML	C8919-20ML	173.50	2 ml	17.35
Silicon Wafer diam. 6 in x t 0.5 mm	-	∼15.00	1	15.00
SU-8 2100 Photo Resist 500ML	-	∼600.00	20	24.00
2-Propanol ACS reagent, ≥99.5% 500ML	190764-500ML	20.30	200 ml	8.12
			Subtotal	410.03
			Total Fungible Cost (€)	**658.27**

Personnel

Approximate cost per hour: 58 €/hr	**Weeks of work:** 3 weeks	**Workhours:** 6 hrs/day	**Cost of personnel (€)**	5220.00
			Total Laboratory Cost (€)	**5878.27**

Production time and cost

This section presents an estimate of the fabrication cost (Table S4) and time (Table S5) for a batch of skin-on-a-chip devices. The microfluidic masters purchased from microLIQUID S.L. contains 17 copies of the SoaC design in a single Si wafer; and the yield of the replication process is approximately 90%. Therefore an average number of 15 functional devices are produced per batch.

The cost per device could be substantially reduced by increasing batch size, given that the cost per batch does not substantially change with batch size. In the present case, however, the use of individual PC filters affects the batch cost; and hence a different membrane would be required for mass product. Moreover, the productivity is significantly limited by the batch fabrication time. The long fabrication time is caused by the use of several methods that are inherently serial. Although not well suited for mass production, the fabrication method presented in this project yield low-cost devices for research purposes.

Table S4: Estimated batch fabrication cost

Fabrication

Product Description	Reference	Cost (€) per unit, volume or mass	Units, Volume or Mass per batch	Cost (€) per batch
PC filter	P9699-100EA	145.40	15 Units	1.45
APTES	440140-500ML	275.80	0.90 ml	0.55
PDMS	Sylgard 184	126.70	70 g	0.12
Isopropanol	190764-500ML	20.30	15 ml	0.04
Additional Materials	-	2.00	-	-
			Batch fabrication cost (€)	32.98 €
			Fabrication cost per device (€)	2.20 €

Skin Seeding

Product Description	Reference	Cost (€) per unit, volume (ml) or mass (mg)	Units, Volume or Mass per batch	Cost (€) per batch
Fibrinogen	F3879	311.90	3.25 mg	0.31
Thrombin	T8885-1VL	277.50	59 µm	277.50
Amchafibrin	CN-700506	3.14	59 µm	0.10
DMEM	11965-092	22.90	707µm	0.05
			Batch seeding cost (€)	17.42
			Seeding cost per device (€)	1.16
			Total Batch Cost (€)	**50.40**
			Total Cost per Device (€)	**3.36**

Table S5: Estimated batch fabrication and seeding time

Replication of the Microfluidic Master

Process	Time (Minutes)
1. PDMS Mixing and Degassing	30
2. Pouring Over the Master	10
3. PDMS Curing	60
4. Peeling-off of the PDMS Replica	10
5. Chip Cutting, Punching and Preparation	30
Subtotal	140 (2 hrs 20 min)

Device Assembly and Preparation

Process	Time (Minutes)
1. Membrane Cleaning and Plasma Treatment	20
2. Preparation of the Silane Solution	20
3. Silanization and Curing	90
4. PC-PDMS Plasma Treatment	20
5. Device Bonding	10
6. Corner Chamfering	5
7. UV Sterilization	20
Subtotal	185 (3 hrs 5 min)

Cell seeding

Process	Time (Minutes)
1. Preparation of the hydrogel	30
2. Fibrin matrix formation	20
3. Epidermal cell seeding	30
Subtotal	80 (1 hrs 20 min)

Total Batch Time	**185 (6 hrs 45 min)**